Correspondent: J. Lach
Experimental Facilities
National Accelerator Lab
Batavia, Illinois 60510

FTS/Commercial: 312-231-6600   Ext. 453

ELASTIC SCATTERING OF THE HYPERONS

M. Atac, C. Dolnick, P. Gollon, J. Lach,

J. MacLachlan, A. Roberts, R. Stefanski, D. Theriot

National Accelerator Laboratory

H. Kraybill, J. Marx, P. Nemethy, J. Sandweiss, W. Willis

Yale University

December 1, 1970

ELASTIC SCATTERING OF THE HYPERONS

We propose to measure the elastic scattering of the hyperons Σ^-, Ξ^-, Ω^- and Λ^0 over a region of momentum transfer up to about 1 GeV/c. As part of this program we will measure the production cross sections of the negative and positive hyperons and carry out a search for new particles with life-time $\gtrsim 10^{-11}$ seconds. This experimental program is based on the use of novel detectors of high spatial resolution which we have developed.

M. Atac, C. Dolnick, P. Gollon, J. Lach, J. MacLachlan

A. Roberts, R. Stefanski, and D. Theriot

National Accelerator Laboratory

H. Kraybill, J. Marx, P. Nemethy, J. Sandweiss, W. Willis

Yale University

December 1, 1970[*]

Correspondent: J. Lach

[*]This and proposal 69 were originally submitted together as one proposal on June 15, 1970.

I. INTRODUCTION

We propose to measure the small angle scattering of most of the hyperons. For some time we have been developing detectors of high spatial resolution - almost an order of magnitude greater than that obtained in normal wire spark chambers - necessary to do experiments with beams of high energy hyperons. These technical developments coincide well with our interest in the physics of small angle scattering: the change in shape or "shrinkage" as energy is increased and the measurement of the forward scattering amplitudes and comparison with SU3.

As part of this program we will measure the production cross section in the forward direction of the charged hyperons, Σ^-, Ξ^-, and Ω^-. The positive hyperons, Σ^+, $\overline{\Sigma}^+$, $\overline{\Xi}^+$, and $\overline{\Omega}^+$ will be produced along with a substantial proton flux, but we feel that those produced with substantial cross sections - as most likely the Σ^+ - can be detected and their production cross section measured. Two methods of detection are proposed to be implemented for the charged hyperons. One is a high resolution gas Cerenkov counter placed immediately after the magnetic channel and the other relies on observing the hyperon decay products. We will be sensitive to hyperon decays which lead to a final state neutron such as

$$\Sigma^- \rightarrow n\pi^-$$

and to those which lead to a final state Λ^o such as

$$\Omega^- \rightarrow K^- \Lambda^o$$
$$ \Big\downarrow \pi^- p$$

In addition, we are particularly interested in the search for new short lived particles, which might well escape discovery elsewhere. Also, the decay properties of such rare particles as the Ω^- will be studied very effectively.

While most of the effort will be devoted to charged particles, we hope to use the neutron-poor Λ beam created by Σ^- charge exchange in Be to study Λ-p scattering. This requires no additional equipment and is probably superior to experiments relying on direct neutral beams.

II. A. ENERGY DEPENDENCE OF SMALL ANGLE SCATTERING

In the last ten years this has been one of the topics in particle physics most discussed by theorists. Here we risk oversimplifying the issues to bring out what seems to be the most crucial question to be settled by going to high energy. This is whether the scattering of small momentum transfers approaches an energy-dependent form as the energy increases, or continues to exhibit a steady shrinkage.

The different theories developed to explain elastic scattering divide rather clearly on this point. Theories of the Regge-pole type with a Pomeranchuk trajectory roughly parallel to other known trajectories predict a shrinking of the diffraction peak for all scattering processes, that is, a continuous increase of slope of the $d\sigma/dt$ as a function of energy. On the other hand, theories with a fixed Pomeranchuk singularity, that is a trajectory showing a very small slope increase with momentum transfer, as well as a wide class of theories related to the optical model such as that of Chou and Yang[1] or Durand and Lipes[2], predict an asymptotic approach to an elastic scattering differential cross section which is independent of energy, particularly at small $\left| t \right|$.

What we now know is that at AGS energies, some peaks shrink (p-p), some grow ($\overline{p}$-p), and some remain constant (π-p). Figure 1 illustrates this situation. The fashion among Regge theorists recently has been for a flat Pomeranchuk trajectory. The observed variations with energy are then ascribed to secondary trajectories, while effects at large $\left| t \right|$ are obscured by cuts. Thus the question can only be resolved by experiments at higher energy and at very small $\left| t \right|$. Great interest has been aroused by the only higher energy result available, the p-p scattering from Serpukhov. There

[1] T. T. Chou and C. N. Yang, Phys. Rev. 170, 1591 (1968).

[2] L. Durand and R. Lipes, Phys. Rev. Letters 20, 637 (1968).

it seems that the p-p elastic peak does not stop shrinking, but rather indicates a Pomeranchuk trajectory with a large slope, Fig. 2. If these results are really correct, perhaps we will find that at sufficiently high energies the π-p and $\bar{p}$-p peaks will begin to shrink too. If so, the old-fashioned Regge model may turn out to be right after all!

To answer these questions, we should determine the trajectory function, $\alpha(t)$, to an accuracy of 0.05-0.10 in bins of 0.1 in $-t^2$. This requires 10,000-20,000 events at each energy, if the determination is made on the basis of measurements at 75 GeV/c and 150 GeV/c. We would probably wish to take 4-6 different energies. For the rarer hyperons, where the rates are limited by flux, we would make do with smaller statistics, appropriate to the fluxes found in the experiment.

II. B. THE HYPERCHARGE DEPENDENCE OF FORWARD SCATTERING

Our program of studying the elastic scattering of charge particles is particularly relevant to studies of the hypercharge dependence of the strong interactions, within a given family of particles. The possibilities are most striking in baryon-baryon scattering, where we will observe states with four different values of the strangeness:

$$p\text{-}p \qquad\qquad\qquad\qquad S = 0$$
$$\Sigma^-\text{-}p, \ \Lambda\text{-}p, \ (\Sigma^+\text{-}p) \qquad S = -1$$
$$\Xi^-\text{-}p, \ \Xi^0\text{-}p \qquad\qquad\quad S = -2$$
$$\Omega^-\text{-}p \qquad\qquad\qquad\quad S = -3$$

In terms of the quark model, we have reactions containing from zero to three strange quarks. These reactions are an ideal testing ground for this model, since the simplest interpretation of present data is that the strange quark has a somewhat different interaction from the non-strange pair.

The least speculative predictions of interactions in the quark model are those dependent on the assumption of additivity of quark amplitudes for forward scattering, since the momentum transfers are then very small. The tests of this model in meson-baryon scattering are well known, and we would look forward to testing these at high energies, where secondary effects are presumably smaller. In baryon-baryon scattering, there are a host of sum rules which may be predicted. A sample of these is given below.[1,2] These are divided into groups, with succeeding groups making the stronger assumptions of spin independence, SU(3) invariance, and high energy limits on quark scattering. Particle labels denote values of the corresponding forward scattering cross sections:

$$\Sigma^+p - \Sigma^-p = pp - np + \Xi^0p - \Xi^-p$$

$$\sqrt{3}\ (\Lambda p - \Sigma^0 p) = pp - np - 1/2\ [\Sigma^+p - \Sigma^-p]$$

[1] D. A. Akyeampong, Nuovo Cimento 48A, 519 (1967).

[2] Dare, Nuovo Cimento 52A, 1015 (1967).

$$\overline{\Lambda p} = 1/2 \ [\Sigma^+ p + \Sigma^- p]$$

$$pp + \Lambda p = np + \Sigma^+ p$$

$$\Sigma^- p = \Xi^o p$$

$$\Sigma^+ p = np$$

$$np = 1/2 \ [\Lambda p + pp]$$

$$\Lambda p + \Xi^- p - 2 \ \Sigma^- p \ = 3/4 \ [np - \Sigma^+ p]$$

$$3 \ [2 \ \Lambda p - \Sigma^- p] = 4 \ np - \Sigma^+ p$$

$$np = pp, \ \Lambda p = \Sigma^- p = \Sigma^+ p$$

$$\Xi^- p = \Xi^o p$$

$$\Lambda p = 1/2 \ [np + \Xi^o p]$$

Aside from the quark model, one can test the predictions of SU3 for the baryon-baryon scattering amplitudes. This is again a favorable place for a test because of small momentum transfers. One needs at least three hyperon cross sections, in addition to the nucleon cross sections, to carry out a test. This should be possible in our experiment, since we should obtain the $\Sigma^- p$, $\Xi^- p$, and Λp cross sections.

III. A. HIGH RESOLUTION DETECTORS

This experiment relies on the use of novel detectors with high spatial resolution. Since these are described only in as yet unpublished reports, a summary of the work which has been done and the characteristics of these detectors may be of interest here. Members of the team presenting this proposal have worked on high resolution spark chambers[1,2] and high resolution proportional chambers[3]. At the present moment, the wire spark chambers have higher accuracy, and our experimental design is based on the resolution which can be achieved in this way with the techniques we have demonstrated. This resolution, 50 μm, is about five to ten times better than that usually achieved in wire spark chambers.

A parallel effort in proportional chambers is yielding very encouraging results. We are confident of achieving an effective resolution within a factor of three of the above value with the present techniques, and we may reasonably hope for further improvements in the near future. Our plan for this experiment is to prepare the wire spark chambers which we know will provide the resolution needed, but to pursue the proportional chamber development as well. If the latter turn out to meet the resolution requirement, we would certainly adopt them to gain the advantage of a factor of a hundred or more in rate and much better time resolution.

The improvement in the performance of the wire spark chamber resolution derives from a program which attacks each of the primary limitations in wire spark chamber accuracy. The diffusion of electrons in the spark

---

[1] W. J. Willis, W. Bergmann, and R. Majker, "High Resolution Optical Spark Chambers," (to be submitted to Nuclear Instruments and Methods).

[2] W. J. Willis and I. J. Winters, "High Resolution Wire Spark Chambers," (ibid.).

[3] M. Atac and J. Lach, "High Spatial Resolution Proportional Chambers," NAL Report FN-208, April 1970.

chamber gas, the basic limitation, is reduced by increasing the gas pressure. The effect of structure and instabilities of the spark column is reduced by reducing the gap width, and thus the spark length. This is permissible because of the higher pressure, which increases the number of ions per unit length, and reduces the spark formation time. Reducing the gap width also decreases the effects of track inclination to the spark chamber plane. In using magnetostrictive readout, the resolution is improved by reducing the size of magnetostrictive wire in the pick-up coil, and by providing a scale magnification by fanning out the wires to four times larger spacing at the readout line.

The wire planes which have been used so far are etched from 10 μm copper on a Kapton backing, with a spacing of eight wires per millimeter. A spacing of twelve wires per millimeter is also feasible with the same technique. The chamber is operated at a pressure of 5-15 atmospheres of 90% neon, 10% helium, 1% argon, 0.1% CH_4. A set of these chambers 4 x 4 cm^2 has been operated in a low energy test beam to measure the resolution. The results, which were limited by multiple scattering, gave an upper limit on the resolution of 65 μm (1 standard deviation limit). It should be possible to attain 25 μm resolution with these chambers. In gases at reasonable pressures, diffusion sets the ultimate resolution limit at 10-15 μm.

The developments in proportional chambers have so far relied on careful field shaping and the possibility of variable pressure[3]. Chambers have been operated with a spacing of one and two wires per millimeter. Both chambers operate well, and the former has been operated in a test beam, with demonstrated efficiency and resolution. With a pair of staggered chambers, this promises 125 μm resolution. Further development is continuing steadily, and within a few months we should know if it is possible to produce proportional chambers of the required resolution at the date needed for this experiment.

III.   B.   HYPERON EXPERIMENTAL ARRANGEMENT

General

This phase of the program breaks naturally into two parts.   The first is a survey of hyperon production and search for new particles, and the second is a study of the small angle hyperon-proton scattering.   Here, we intend to study the range of t from $|t| \cong 0.1$ to $|t| \cong 0.6$ for which one may usefully detect the recoil proton.   Detection of the recoil is necessary in the hyperon scattering experiments in order to provide a trigger which efficiently selects scattering events.

Figure 3 is a diagram of the experimental arrangement of the short lived particle phase of the program.   A beam of 200 GeV protons impinges on a target of cross section 1 mm x 1 mm and approximately one interaction length in the beam direction.   High energy negative particles produced in the forward direction are transmitted by a magnetic channel.   Following the channel approximately 5 m is available to insert precision wire chambers, focusing Cerenkov counter, and/or a liquid hydrogen target.   A focusing Cerenkov counter will be used in the new particle search and as a check in the survey of hyperon production fluxes.   Then begins the decay region followed by the first analyzing magnet, A1.   This magnet allows a determination of the momentum of the low energy particles, leptons, and mesons, produced in the decay.   The high momentum protons produced through a decay chain such as

$$\Omega^- \rightarrow K^- \Lambda^o$$
$$ \hookrightarrow \pi^- p$$
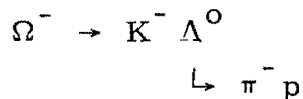
are further deflected from the long lived component of the negative beam by A2.   They strike the proton trigger counter shown in Fig. 3.   High energy neutrons produced in decays such as

$$\Sigma^- \rightarrow n \pi^-$$
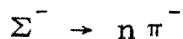
are identified in the neutron shower counter indicated in the same figure. We now discuss the arrangement in more detail.

The Magnetic Channel

The magnetic channel we have chosen is 6 m long and is a modified main ring bending magnet. Figure 4 is a cross section view of this magnet. The inner coils of a standard main ring magnet have been removed and the pole tips closed down to a gap of 1 cm. Computations with the LRL magnet design code, LINDA, indicate that with this modified configuration one could achieve a field of 40 kG. The channel is tapered in the horizontal plane from an aperture of 2 mm increasing to 6 mm at the channel exit. The channel has as its central momentum 150 GeV/c at a field of 30 kG. With this channel geometry one could easily deflect particles of up to the full beam energy down the channel. The actual design would have an enlarged portion of the channel in the region of the target so as not to confuse interactions in the walls with those in the target. The properties of this channel have been investigated extensively using a Monte Carlo computer code. The full momentum band transmitted by the channel is 10%. However, momentum and exit position and angle are highly correlated, and with our detectors the momenta of individual hyperons can be determined to within 0.1%.

Hyperon Fluxes

We have used the hyperon production cross sections suggested by Sandweiss and Overseth[1] to estimate the hyperon fluxes emerging from our magnetic channel and surviving to 5 m beyond it which is the start of the

---

[1] J. Sandweiss and O. Overseth, TM-199, NAL, January 1970.

decay region. They estimate that using 200 GeV incident protons to produce Σ^- at 150 GeV/c in the forward direction the cross section is

$$\frac{d^2 N}{d\Omega dp} = 0.038 \ \Sigma^- /\text{int. proton/ster/GeV/c.}$$

For the channel we have described and for 10^{10} protons interacting in our target this results in a flux of

1775 Σ^- per pulse.

If we assume the production cross section for Ξ^- is lower by a factor of 30 and of Ω^- by a factor of $(30)^2$ we observe at 150 GeV/c

60 Ξ^- per pulse

0.6 Ω^- per pulse.

Using the Hagedorn-Ranft computations[2] we will also have emerging from our channel

83,000 π^- per pulse.

This is a flux of pions which will give no problem with accidentals and indicates that incident proton fluxes of up to 10^{11} protons per pulse might be desirable.

An estimate of the Σ^+ has been made by Hagedorn-Ranft[2] and give at 150 GeV/c for 10^{10} interacting protons per pulse

35,000 Σ^+ per pulse.

The proton and π^+ contribution to the beam will be according to the same Hagedorn-Ranft computation

and

3,000,000 protons per pulse

450,000 π^+ per pulse.

---

[2] T. G. Walker, NAL, 1968 Summer Study, Vol. 2, p. 59.

If these predictions have any validity we should be able to extract a fair amount of physics with this Σ^+ beam. There are no predictions for the expected yields of the other positive hyperons.

High Resolution Cerenkov Detector

A high resolution Cerenkov counter[3] used at the magnetic channel exit would provide detection of hyperon fluxes regardless of their decay mode. This counter would be used to check the production fluxes of the known hyperons, which would be determined primarily by decay identification, and to search systematically for new particles which might not be detectable via their decay with our apparatus. The results of our studies can now be summarized as follows:

1) We propose the construction of a 4-meter, low-pressure gas focusing Cerenkov counter. The cone angle will be from 7 to 12 mrad, a parabolic or spherical mirror will be used, and a ring aperture on a single 2-inch fused silica-window photomultiplier will provide velocity selection and hence particle identification. The attainable resolution in β, limited by the energy spread of the beam and the angular divergence accepted, will be in the range 5 to 10 x 10^{-6}, and will be adjusted to just separate adjacent mass particles; the most severe requirement is the $\Sigma^- \text{-} \Xi^-$ separation. The data of Reference 4 indicate that we should average 8 photoelectrons per particle.

2) Suitable angular restriction of the accepted beam, which must be held to ±0.2-0.3 mrad, will be obtained from coincidences with the hodoscopes required to determine the hyperon direction with high precision.

---

[3]A. Roberts, M. Atac, R. Stefanski, NAL internal report.

[4]Yu. P. Gorin et al., IHEP 69-63, Serpukhov 3-20 (1969).

3) The dispersion and momentum acceptance of the presently conceived magnetic channel are such that the angular restriction required for the Cerenkov counter will admit only about 1-2% of the total hyperon beam. This appears to be adequate for survey purposes, although not for experiments on the rarer hyperons.

4) The resolution of the counter is adequate for separation of all particles heavier than kaons; it is marginal for kaon-pion separation and inadequate for lighter particles. For survey purposes, the resolution can be varied, so that it is adjusted to be sufficient for the known hyperons; for a search for heavier particles, it can be decreased to make the search easier. The mass search is conducted by varying the counter pressure, thus varying the velocity interval accepted.

Hyperon Decay Spectrometer

Table 1 is a summary of the maximum decay angles of the hyperon decays of interest at 150 GeV/c. For comparison we also list the decay angles at 23 GeV/c which are appropriate to the hyperon experiment being done   by this same group at Brookhaven National Laboratory. The angles of the two experiments scale approximately as the ratio of the momentum of the hyperons. The most crucial measurement is the determination of the hyperon angle which is accomplished by high resolution wire chambers. As was mentioned earlier we believe we can achieve spatial resolutions of 50 μ which means that the initial hyperon direction can easily be determined to the required accuracy before and after scattering from the 40 cm liquid hydrogen target in the 5 m between the magnetic channel and the start of the decay region. For both the initial hyperon flux measurements and the hyperon scattering experiment the hyperons will be identified by their decay products. It is worthwhile to consider in some detail the kinematics of the relevant decays. Consider first the decay of $\Sigma^- \to n\pi^-$. The π^- angle and momenta are determined by spectrometer A1 and wire spark planes of conventional design (resolution ∼0.3 mm). The neutron direction is determined

by a hadron shower counter similar to the one used in our BNL experiment. To achieve equivalent angular resolution, assuming the neutron interaction position can be determined to about 1 cm requires a neutron detector of 1 m x 1 m in size positioned about 100 m from the channel exit. The neutrons resulting from the Σ^- decay are of high energy and the neutron detector need only give us a very crude indication of energy.

The signature of the Ξ^- will be

$$\Xi^- \rightarrow \pi^- \Lambda^o$$
$$\llcorner \pi^- p \,.$$
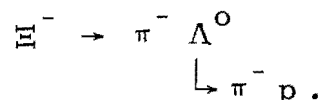
The π^- kinematics are determined by A1 as well as the properties of the π^- resulting from the Λ^o decay. The proton from the Λ^o decay is further deflected by A2 and is well separated ($\sim$0.75 m) from the π^- beam emerging from the channel at about 50 m from it. Here a wire chamber array and a proton trigger counter will be located. The emergence of a positive nucleon from a well defined negative beam should provide a powerful trigger for Λ^o events. The kinematics and triggering of the $\Omega^- \rightarrow K^- \Lambda^o$ decays is qualitatively similar but can easily be distinguished in this highly overconstrained fit (4c) from the Ξ^- decay. The apertures required of A1 and A2 are modest. Standard BNL 18D72 magnets would be adequate.

We note that the hyperon beam described here offers many potential advantages for the study of rare hyperon decay modes. In particular the longer decay lengths at NAL energies implies substantial improvements both in absolute rates and in beam background. We anticipate that the production fluxes and the developing techniques of particle identification at high energies will make these experiments feasible and attractive.

New Particle Search

The beam geometry used for the short-lived particle phase of this experiment is ideal for a search for new particles of lifetime 10^{-11}-10^{-10} seconds. This lifetime range is not accessible to the conventional beam

survey experiments. Such particles are detectable with a focusing Cerenkov counter or by their decay products. The detection via the Cerenkov counter would, of course, be independent of decay mode; but because of the limited angular acceptance of the Cerenkov counter only about 1-2% of the beam could be counted. The flux of such a presumed particle would depend on three factors; its production cross section, its lifetime, and mass. Figure 5 indicates the regions of these variables in which our search would be significant. In that figure we relate the production cross section of our particle to that of the Hagedorn-Ranft π^- production cross sections. We have plotted for a given production cross section the lifetime versus mass which would give us one count in the Cerenkov detector for 10^{11} interacting protons. The efficiency of the Cerenkov counter (1%) has been included in these calculations. Both positive and negative particles could be investigated in this manner.

For the case of detection via decay only, the sensitivity would be increased by a factor of 50-100 (the loss due to Cerenkov acceptance) but reduced by its branching ratio into a detectable decay mode.

In the decay experiment the system trigger would be various combinations of a high momentum neutral or positive particle (presumably the fast baryon) in coincidence with a lower momentum particle (presumably meson or lepton).

IV. SUMMARY OF RATES AND BEAM REQUIREMENTS

Diffraction Peak Measurements with Hyperons

Here, at least for the Ξ^- and Ω^-, the experiment is limited by available beam flux. On the other hand we do not attempt to measure the Coulomb interference so less data is needed. As noted earlier in these measurements we must detect the recoil proton and measure its energy. This limits the t range to $|t| = 0.1$ to 0.6. Also measurements will most likely not be made for the anti-hyperons so the measurement matrix is smaller than for the stable particles. These factors nearly compensate and we expect that this phase of the experiment will also take about 200 hours of ideal time to complete. It should be noted however that there are large uncertainties in the estimates of the hyperon fluxes, particularly for the Ξ^- and Ω^-. These fluxes will hopefully be better estimated after the BNL Y^- experiment has run in 1970-71.

Experimental Equipment Required

Much of the counting and data collecting equipment required for the experiment is very similar to that being developed by this group for the BNL hyperon experiment. This experiment will require an on-line data collecting computer such as the NAL PDP-15 which will be used for the BNL hyperon experiment. The interfaces being developed for its BNL usage would also be needed for this experiment, and it is requested that this same machine be made available to us. Ideally, as in our BNL usage, we would like a link from the PDP-15 to a larger machine capable of carrying some fraction of the data through to the final analysis. However if this is not available access to a larger on-site computer which would be capable of reading the magnetic tape output of the PDP-15 would be essential.

We require a high energy ($\sim$200 GeV) proton beam of intensity 10^{10}-10^{11} protons per pulse focused to a spot of about 1 mm in cross sectional area.

We believe the proposed diffracted proton beam planned for Area 2 would be suitable. We believe the magnetic channel can be a main ring bending magnet with the inner coils removed and magnet channel sketched in Fig. 4 inserted. Two analysis magnets comparable to BNL 18D72 magnets and a liquid hydrogen target complete the list of requirements.

Table 1

Hyperon Decay Kinematics

Maximum Laboratory Angles

		23 GeV/c	150 GeV/c
$\Sigma^- \rightarrow n\,\pi^-$	θ_n	10.7 mr	1.63 mr
	θ_π	71.7	11.00
$\Xi^- \rightarrow \Lambda^o\pi^-$	θ_{Λ^o}	7.15	1.10
	θ_π	57.2	8.78
$\Omega^- \rightarrow \Lambda^o K^-$	θ_{Λ^o}	19.1	2.93
	θ_K	153.0	23.4
$\Lambda^o \rightarrow \pi^- p$	θ_p	5.17	0.79
	θ_π	34.8	5.34

Figure 1

Pomeranchuk (?)

pp elastic scattering

α_{eff}

P', ω trajectory

$- t \ (GeV/c)^2$

Pomeranchuk (?)

$\pm$ p elastic scattering

α_{eff}

P', ρ trajectories

$-t \ (GeV/c)^2$

From; G. Fox, High Energy Collisions

Figure 2
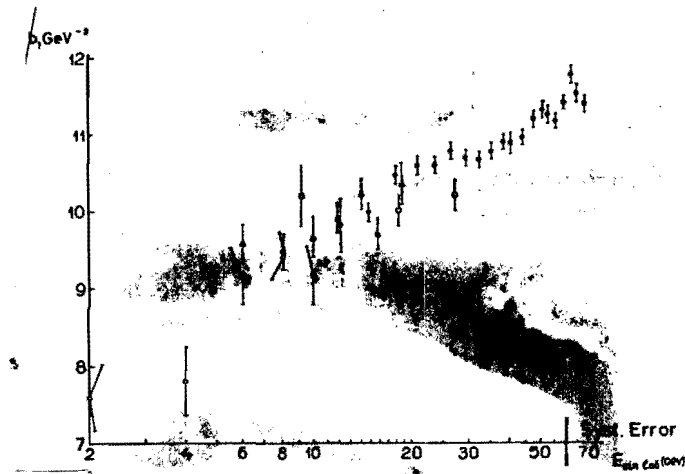
The slope parameter b_1 from elastic proton-proton collisions (see text) as a function of energy. The symbols represent data from Ref. 14, Ref. 16, Ref. 17 and Ref. 18.

Figure 3

Hyperon Experimental
Arrangement

End Y⁻ Detector
Start Decay Region
X=5m

Neutron Counter
X=100m

A1   A2

Y

200 GeV Protons → X

Target
1mm x 1mm

Origin of
Coordinate System

6m Magnet
H= 30kG
0.2 cm. x 0.6cm. Channel
Set to 150 GeV/c

A1   18D72
H=20kG
A1 Center
X= 17m
Y=0
Gap: 8 inches

A2 Same as A1
X=24m
Y=0

Proton Counter
X=50 m
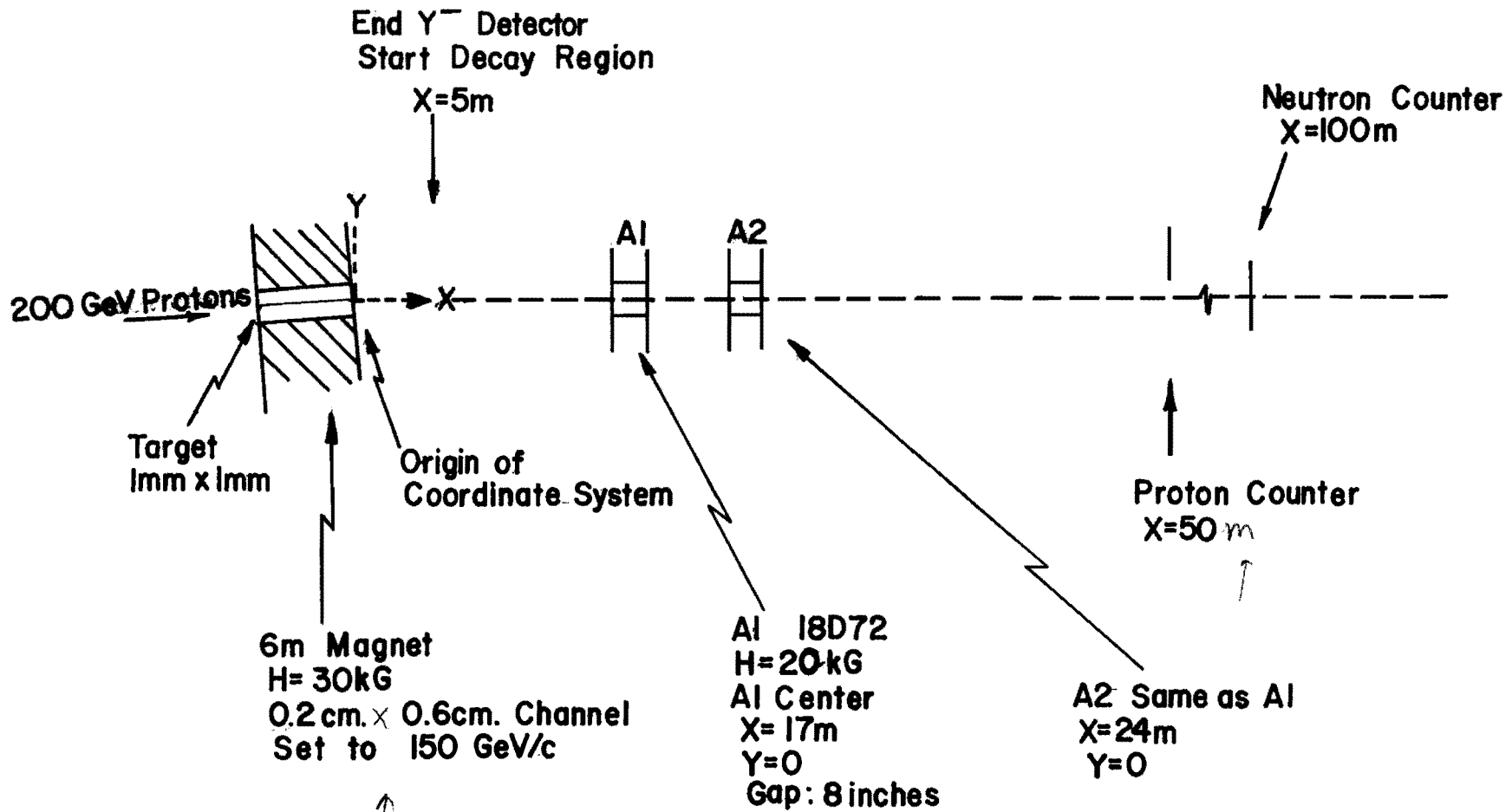
Figure 4
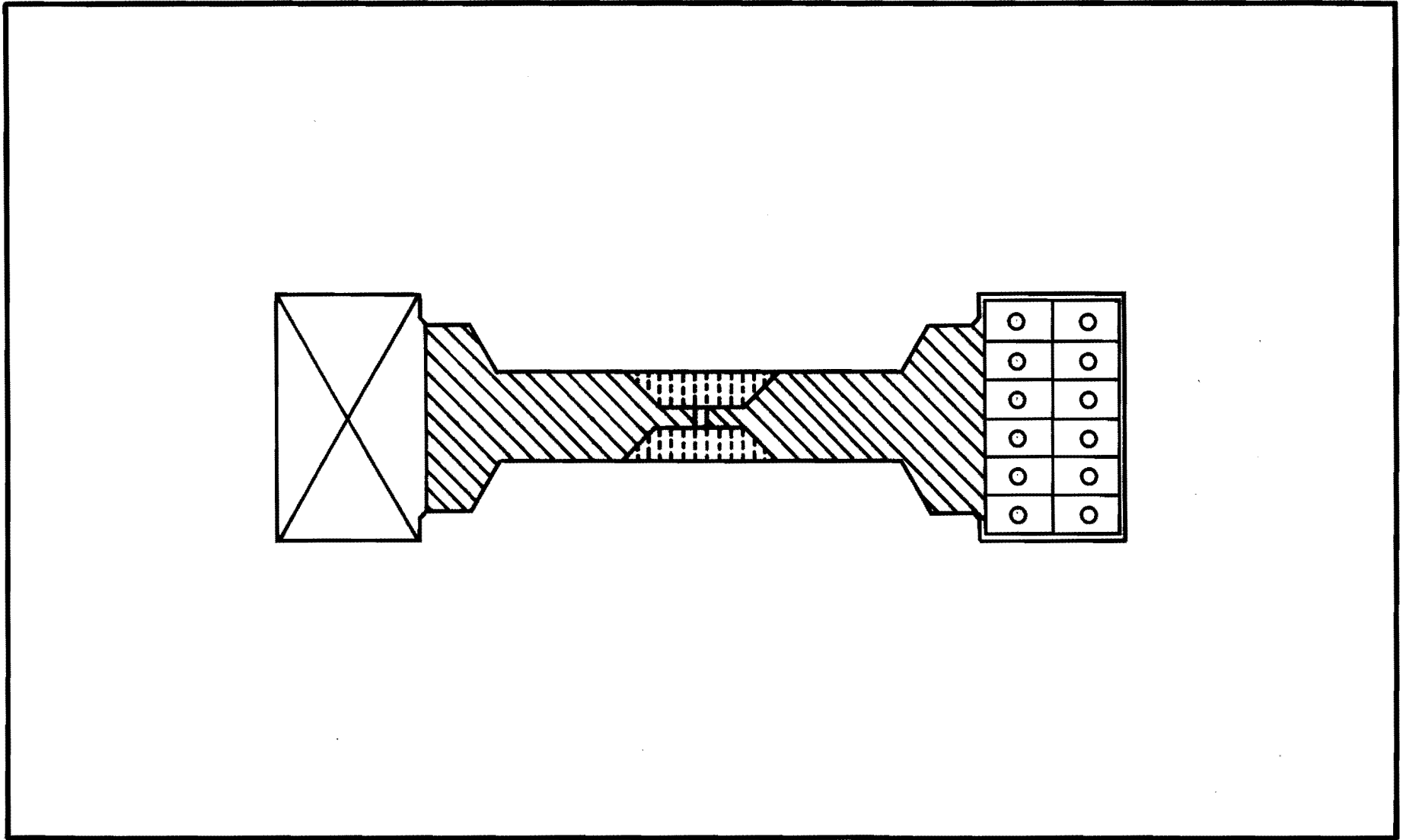
Scale: 2.5" per inch

//// Brass Shield

||||| Co-Fe Pole Tip

Mass and Lifetime Range
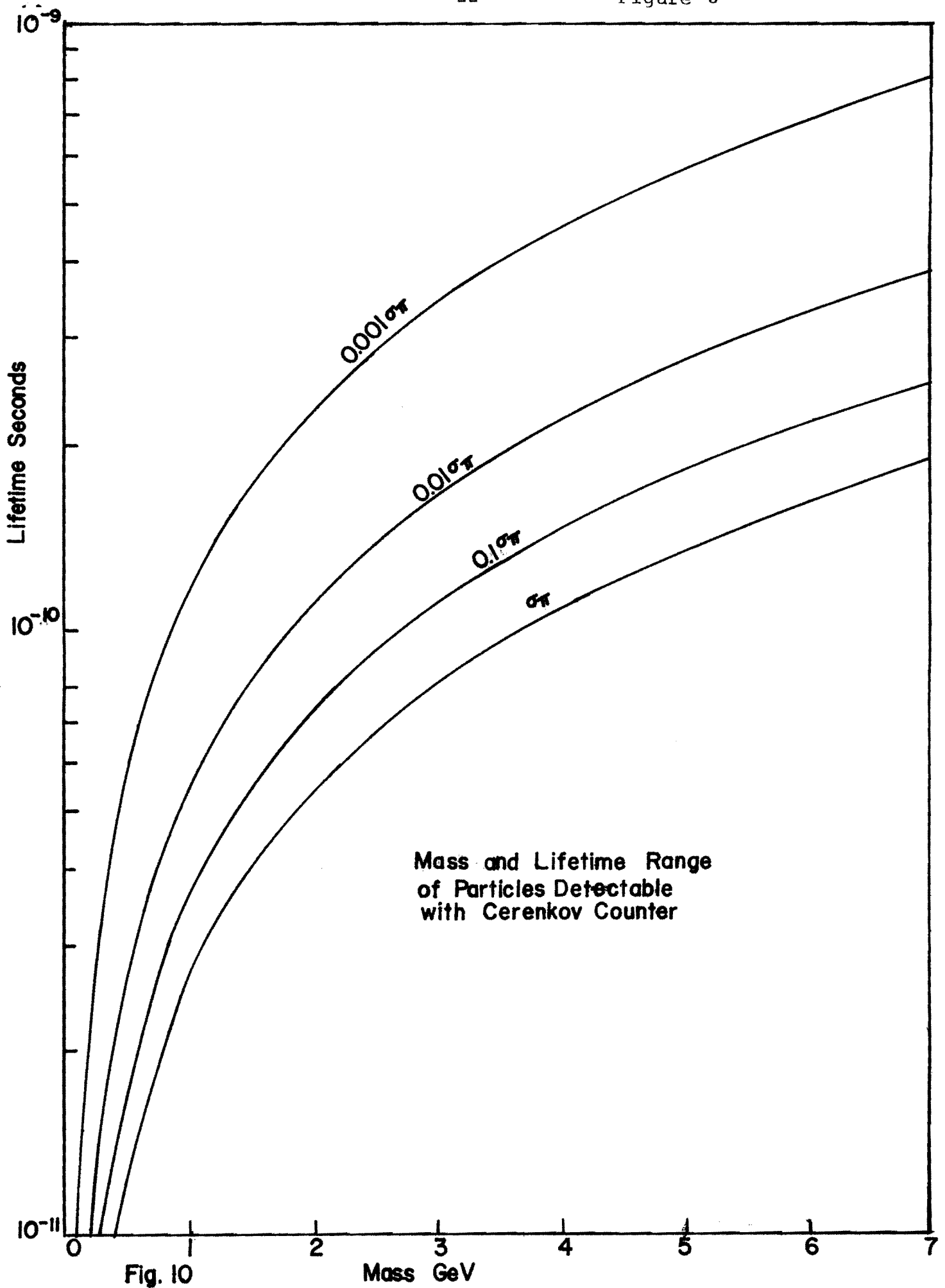of Particles Detectable
with Cerenkov Counter

Fig. 10   Mass GeV

May 13, 1976

ELASTIC SCATTERING OF THE HYPERONS - ADDUNDUM TO E97

M. ATac,

C. Ankenbrandt, S. Ecklund, P. J. Gollon,
J. Lach, J. MacLachlan, A. Roberts,
and G. Shen
Fermi National Accelerator Laboratory,
Batavia, Illinois 60510

and

L. A. Fajardo, R. Majka, J. N. Marx,
P. Nemethy, J. Sandweiss, A. Schiz,
and A. J. Slaughter
Yale University
New Haven, Connecticut 06520

In this note we update our charged hyperon E97. We had written E97 and it was approved in 1970 before the successful operation of either the CERN or our BNL hyperon beam. In the intervening years both of these beams have demonstrated the richness of the hyperon beam technique as a way of measuring the basic properties of the hyperons. We need only recall the CERN measurements of the hyperon total cross sections[1] and our measurements of the $\Sigma^- p$ differential cross section[2] and program of hyperon weak decays[3] using the beam we constructed[4] at BNL. We have gained much experience using hyperon beams since E97 was written and we now wish to embody this experience into our Fermilab program.

About a year ago we pointed out the desirability of moving E97 from the M2 beam of the Meson Laboratory into a new area which we proposed building downstream of proton center. This new hyperon area would allow us to take advantage of the excellent optical properties of the primary proton beam and allow use of higher intensities and higher energy when it becomes available.

The configuration of this new area was discussed in detail during a workshop held at Fermilab in December 1975 and reported in the March 1976 issue of NALREP. The changes we will now make in E97 incorporate changes necessitated by this move, additional knowledge gained by our BNL experience, especially in better hyperon flux estimates, and finally the advances made in instrumentation during the last half dozen years.

The physics we wish to do was fundamental and important in 1970. It has lost none of its luster and we have lost none of our enthusiasm to pursue it.

Physics Goals

The physics goals are the same as in the original proposal. They center around the measurement of the hyperon proton differential cross sections in the nuclear region. These would include, $\Sigma^- p$, $\Xi^- p$, $\Sigma^+ p$, and possible $\Omega^- p$. We would make these measurements as a function of incident momentum from about 100-350 GeV/c consistent with the available hyperon intensities. The first step would be a measurement of hyperon fluxes so that a reasonable program could be planned. In particular the estimates of the Ω^- flux is very uncertain and we have only tentatively included it in our list of cross sections that we plan to measure. The flux measurements themselves have significant physics interest since the forward production spectra of Σ^-, Ξ^- and Ω^- gives insight into the exchange mechanics leading to high strangeness states. Another interesting question we would investigate is whether charged hyperons are produced with significant polarization similar to

the substantial polarization of Λ^{o}'s seen in Fermilab E8. We would also search for new particles with lifetimes of ~10^{-11} seconds. It is worth noting that no Ω^- particles have been detected at Fermilab and only a few Ξ^- have been seen in bubble chamber pictures so we feel that this lifetime range is very poorly explored at Fermilab energies. Our physics goals are the same as in the original proposal and we refer the reader to it for a more detailed discussion. The extensions are due to the increased accelerator energy (E97 was proposed when Fermilab's accelerator was a 200 GeV machine) and the higher intensity available in the Proton Laboratory.

Hyperon Fluxes

Figure 1 shows the available data on the production cross sections for the charged hyperons. The data shows the invariant cross section plotted as a function of α, the hyperon momenta divided by the incident beam momenta. In this range it is very close to the Feynman x variable. The data shown are measurements from the CERN and BNL hyperon experiments. We assume that these cross sections scale to Fermilab energies. In the following discussion we assume that the Ω^- is below the Ξ^- flux by the same ratio that the Ξ^- flux is below the Σ^- flux. With channel designs discussed in the next section we should be able to attain 10^4-10^5 Σ^-, 10^2-10^3 Σ^+ and Ξ^-, and a few Ω^- per pulse assuming a total of ~10^6 particles per pulse exiting the hyperon beam channel. These are extraordinary hyperon fluxes; the fractional content of Σ^- is comparable to that of K^- in Meson Area beam lines; the Ω^-

fluxes would allow one to equal the world sample of Ω^- in one or two minutes!

The Hyperon Beam Channel

The design of the hyperon channel has evolved from the rather crude design in our original proposal - remember no hyperon beam had yet operated - to our latest and most sophisticated version described in TM-610 by A. Roberts and S. Snowdon, which is attached. Intermediate versions are described in our hyperon decay proposal E353 and the attached internal note by C. Ankenbrandt. A simplified drawing of the Roberts and Snowdon design is shown in Fig. 2. Figure 3 is the design of the hyperon beam for the CERN SPS. Both designs use superconducting quadrupole magnets to increase the acceptance and to render the beam parallel so that a differential Cerenkov counter can be effectively used. The superconducting quadrupole design was pioneered by the CERN group and used successfully in their experiment done about six years ago. The quadrupoles we propose to use are very similar to those being planned for use in the Fermilab Energy Doubler/Saver. The maximum channel momentum is 360 GeV/c. The hyperon fluxes quoted in the previous section are typical and the reader is referred to TM-610 for details.

If 1000 GeV protons were available from the Energy Doubler/ Saver they could be utilized with the present design. Although the maximum channel momentum is fixed at 360 GeV/c, increasing the incident proton energy from 400 to 1000 GeV would correspond to changing the α in Fig. 1 from 0.90 to 0.36 and hence much larger flux of the heavier hyperons Ξ^- and Ω^-. Of course if one wanted

a hyperon beam at higher momenta, additional magnets would have to be added to the channel. This would be desirable for studies of the s-dependencies of strong interaction processes but for studies of the decay properties of hyperons it is not necessarily the higher hyperon energy that is desirable but the increased flux.

Cerenkov Counter

An integral part of the system is a Cerenkov detector which we have designed to identify hyperons as they exit the channel. This counter is described in the enclosed technical note FNAL, YJS-1 by J. Sandweiss. The counter and the design of the hyperon channel must be considered together in order to match their acceptances. This counter uses a Channel Electron Multiplier Array (CEMA) to achieve simultaneous identification of the three charged hyperons. The CEMA technology is advancing rapidly and provides a way of obtaining high spatial resolution with the quantum efficiency of the best photomultipliers. This "Phase I" design has as a back-up position the ability to substitute a conventional photomultiplier for the CEMA. The very desirable feature of simultaneous identification of the three hyperon types would not be possible in this alternative.

Analysis Magnets

We feel that analysis magnets somewhat larger than those requested in the original E97 proposal would be highly desirable. Two of the newly designed ECHO series of magnets 12 x 24 x 72"

would appear to be adequate for a substantial initial program.
The full program of weak interaction physics proposed in E353
would benefit if the first analysis magnet had larger aperture
and higher field integral. For both E97 and E353 we would be
willing to undertake the initial program with two of the ECHO
series magnets.

Instrumentation

The instrumentaion in our original proposal was state of the
art in 1970 but antiquated by modern standards. We would use
instead of the high resolution spark chambers ($\sigma \sim 65\mu$) propor-
tional chambers which we have developed and successfully used
for E69 which have similar spatial resolution. We would use the
E69 high resolution chambers which have a 3 cm aperture but in
addition would have to build at least one cluster of such cham-
bers with approximately double that aperture. Although chambers
of that size and resolution have not been built before, we believe
we have that technology well in hand.

The proportional chamber readout system used in E69 would
also be used for the hyperon experiment except that we would re-
design that section of it which uses a LeCroy hybrid circuit
containing a one shot delay. This now represents a substantial
electronic dead time (~ 600 nsec) which we believe can be greatly
reduced. We are well satisfied with the system organization of
our E69 readout system and in particular the ease with which it
allows the proportional wire chamber addresses to be interfaced
to our analog processors. These analog processor allow us to

trigger on tracks which appear to change directon (kinks which could indicate a scatter or decay). Such a system has demonstrated its utility and reliability in E69 and we would plan to use a up-dated version of it in our hyperon program.

During the last few years our group has developed and tested small high resolution (50-100μ) drift chambers. We believe these chambers can be scaled up to sizes of about 1 m^2 and have spatial resolutions of about 100μ. A special precision wire placement machine is now being completed for the construction of these chambers. A prototype drift chamber readout system matching this chamber resolution has been constructed and is ready for testing. We thus would like to replace the spark chambers used for the momentum analysis of the hyperon decay products by drift chambers.

We estimate that the flux measurements and new particle search will require about 600 hours of accelerator time and the measurements of the differential cross sections will require another 600 hours.

REFERENCES

[1] J. Badier, et al., Phys. Lett. $\underline{41B}$, 387 (1972).

[2] P. Nemethy, et al., Proceedings of the 1976 Particles and Fields Conference in Seattle, Washington p. 335 Sept. 1975.

[3] W. Tanenbaum, et al., Phys. Rev. $\underline{D12}$, 1871 (1975).

[4] V. Hüngerbuehler, et al., Nucl. Instr. and Methods $\underline{115}$, 221 (1974).

FIGURE 1
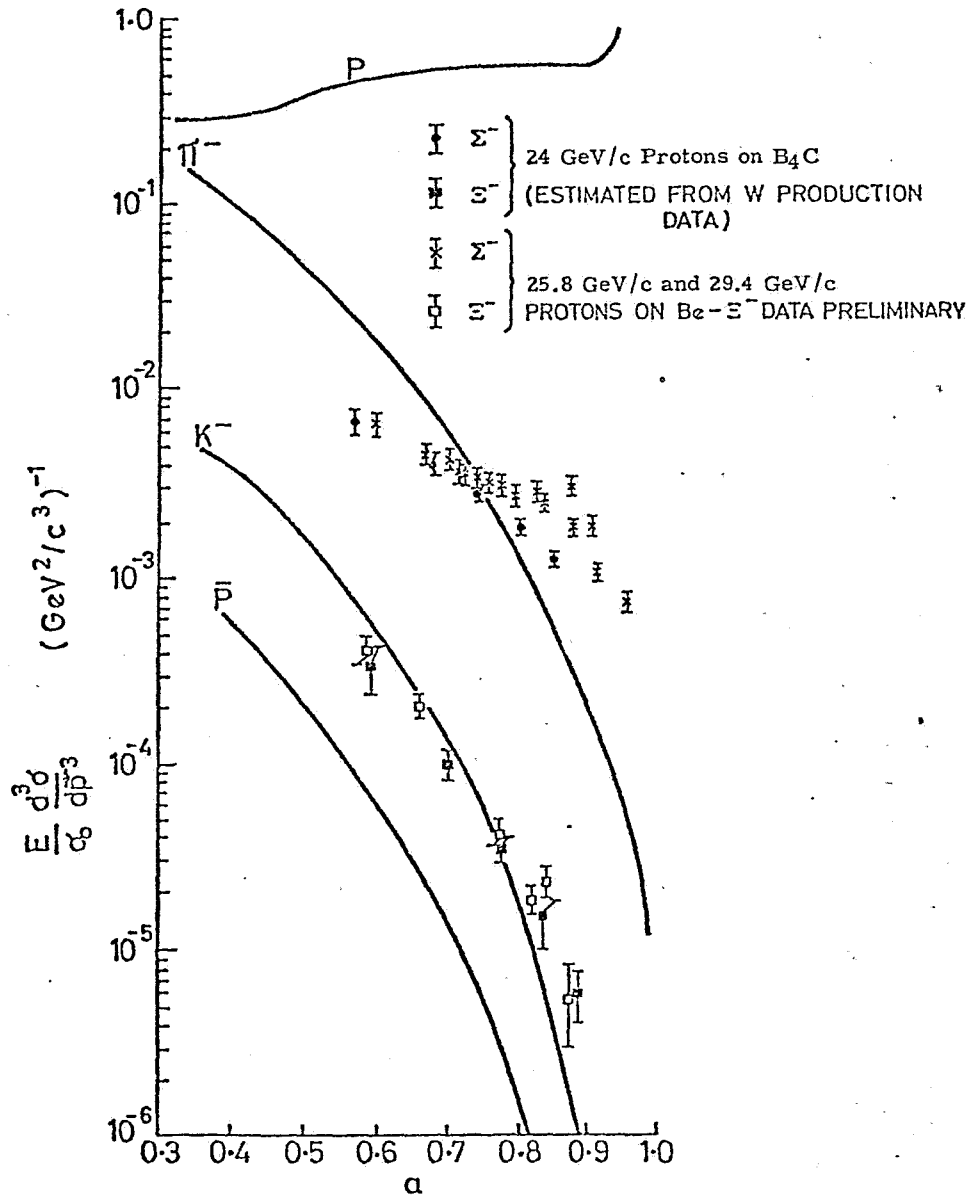
The invariant inclusive cross section plotted as a function of the longi-
tudinal laboratory momentum normalized to its kinematic limit for various
particles produced in p-Be collisions.

FERMILAB HYPERON BEAM

J. LACH
MAR. 14, 1976

Preliminary Design from: TM-610
Roberts + Snowdon

400 GeV/c MAX. MOMENTUM

1m

TGT

BM1

BM2

Q1V

Q2H
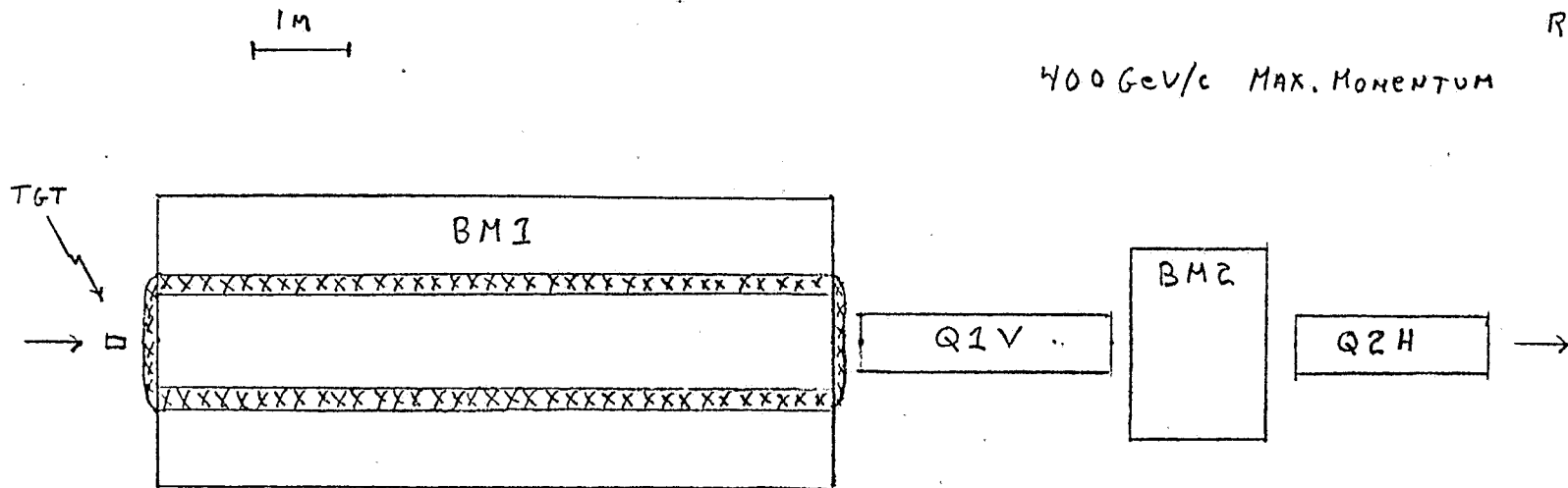
BM1 7.0 M long, gap ~ 3cm
40 KG Superconducting

BM2 1.5 M long, gap ~ 3cm
40 KG Superconducting

Q1V 3.1 M long, 3cm diameter
100 T/M (25.4 KG/IN.)
SUPER CONDUCTING

Q2H 2.0 M long, 3cm diameter
100 T/M (25.4 KG/IN.)
SUPER CONDUCTING

FIGURE 2

CERN SPS HYPERON BEAM

J. LACH
MAR. 14, 1976

150 GeV/c MAX. MOMENTUM

1 M

TGT.

200 GeV
PROTONS →

M1   M2   M3   Q1   Q2 →
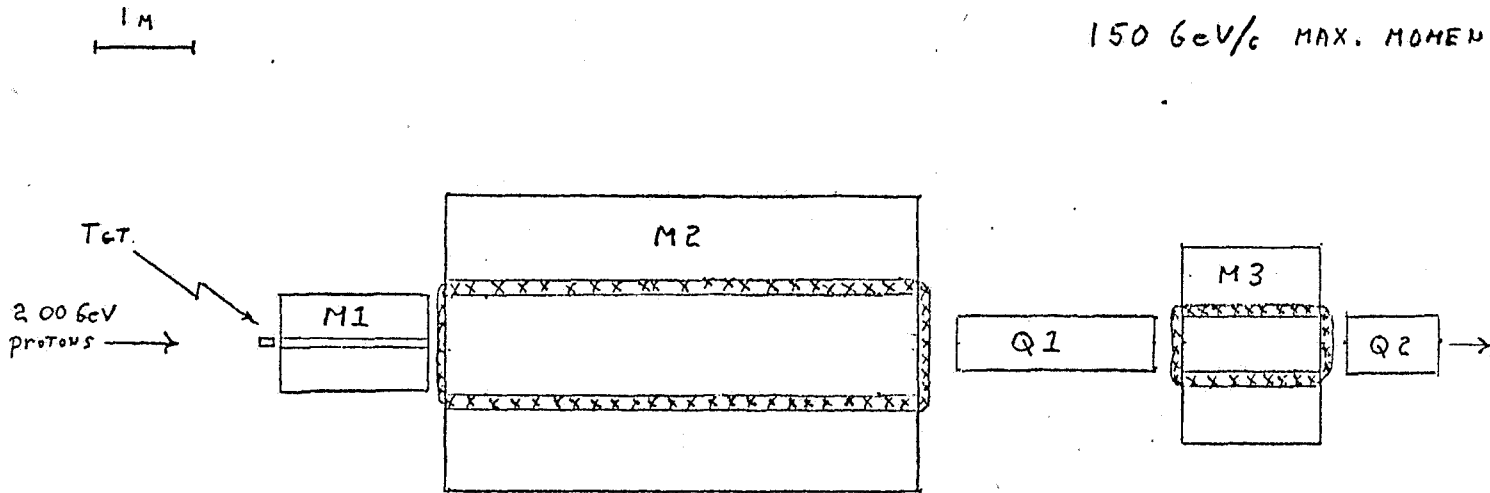
M1   1.5M long, gap ~ 5cm
41 KG   NON SUPER-CON.

M2   4.0M long, gap ~ 4cm
35 KG   pole = 1M × 8cm
NON S.C.

M3   1.5M long, gap ~ 10cm
20 KG   NON. S.C.

Q1   2M, 4cm diameter
81 T/M (20.6 KG/IN.)
SUPER CONDUCTING

Q2   1M, 4cm diameter
105 T/M (26.7 KG/IN.)
SUPERCONDUCTING

FIGURE 3

DESIGN OF A CHARGED HYPERON BEAM TRANSPORT SYSTEM

AND CERENKOV DETECTOR FOR THE ENERGY RANGE

150 - 400 GeV

by

A. Roberts and S. C. Snowdon
Fermi National Accelerator Laboratory,
Batavia, Illinois 60510

ABSTRACT

The design of a charged hyperon beam to cover the momentum range 150 - 400 GeV/c at Fermilab is investigated. The following conclusions are reached:

1) An achromatic beam design is superior to a conventional dispersive beam; it allows the production of a parallel beam, the use of Cerenkov detectors of much simpler and more powerful design, and particle identification and tagging to higher momenta. In addition, with a conventional detector, a wider momentum range can be accepted.

2) Beams to cover the range 150 - 400 GeV can be designed; the change required to cover this range may be merely retuning, but this is wasteful of decay length. The recommended arrangement is to change the cone angle of the focusing Cerenkov detector from 7 to 11.5 mrad to cover the range, with a corresponding change in length, 15 m and 7 m. Separation of sigma from xi should be feasible to energies of 320 GeV or more.

For the Cerenkov detector, the DISC is rejected as less flexible than the focusing counter. In later phases of the work, if and when CEMA (channel electron multiplier array) image intensifier tubes with segmented anodes becomes available, the system should become capable of simultaneously processing all the hyperons.

3) The reduction in muon background to be expected with a special beam-dumping, muon-deflecting first bending magnet has been investigated, using the program HALO. The residual background is worst at the lowest values of alpha; but even there the background level still seems well within tolerable limits.

4) All magnets, including the beam dump, may use super-conducting coils; the quadrupoles require them to achieve the necessary gradients.

I. DESIGN OF FERMILAB CHARGED HYPERON BEAM

A. Requirements

The design study to be described is a continuation of earlier studies for a charged hyperon beam, whose results have been embodied in several reports, as well as proposals for experiments[1-5]. It deals only with the production of a beam of charged, tagged hyperons; the experimental equipment for the study of decays and interactions will be treated elsewhere.

Until early in 1975, the general assumption was that a charged hyperon beam would be built in the meson area, replacing the neutral hyperon beam in M2. The beam design therefore used the same large sweeping-analyzing-beam-dumping magnet. The beam design was, in fact, of minimum sophistication; aimed at a maximum momentum of 150 GeV/c, it included only a bending magnet and a quadrupole pair, to give point-to-parallel focusing, but with the momentum dispersion imposed by the bending magnet.

The requirement of a parallel beam is due to the need to identify beam particles. The negative beam contains at least eight different kinds of particles, the positive six, not counting in either case the anti-hyperons present; adding them brings the count to 9 in both cases. Particle identification in such a beam is best done by a focusing Cerenkov detector, which demands a parallel beam. The Yale-NAL-BNL hyperon beam at BNL did not include a Cerenkov detector, (and we sometimes wished it had); the corresponding CERN PS beam did have one. At Fermilab energies, where the additional length required for a Cerenkov detector is far less costly in hyperon decay than at BNL, such a detector is clearly worthwhile.

The design criteria for an ideal charged hyperon beam thus include the following points:

1)   Since baryon yields are maximal in the forward direction, the secondary beam should be taken in the forward direction for best signal-to-noise ratio.

2)   At any primary proton energy, the secondary beam should be capable of covering a fairly wide range of alpha (ratio of secondary to primary momentum.)   The yields of different hyperons are known (from our BNL work[6]) to peak at different values of alpha.

3)   For maximum flexibility it is wise to design for the full range of primary proton energies likely to be available in the next few years, and for as wide a hyperon momentum range as possible. A suitable range is 150 - 400 GeV.

4)   The beam should provide for identifying and tagging the various particles composing it.   By tagging, we mean providing a prompt electronic identification signal for use in event logic. The ability to simultaneously identify and tag all the particles in the beam is not required;   the particles lighter than protons need not be separated, only rejected.   The minimum requirement is to tag at least one kind of hyperon at a time; it is desirable to be able to tag more than one, but not essential.

5)   The beam characteristics and shielding must be such as to provide an adequate flux of hyperons for experiments without an excessive background.   Two different backgrounds are of concern:

the pion (and other light particle) flux in the charged beam, and the diffuse muon background produced in the same target as the hyperons. The total beam flux is limited not so much by the proton beam current or the beam optics, but by the need to individually count beam particles. The muon flux downstream, in drift chambers and other large area detectors, must be tolerable at the full intensity level of the beam; this requirement imposes a need for a special muon-deflecting magnet at the front end of the beam.

6) Since the beam will contain a momentum bite of several percent, it must also include means for measuring the momentum of individual hyperons to at least 0.5%, in order to give sufficiently precise information for kinematic reconstructions.

B.   Decay Lengths

The overriding consideration in beam design is the short lifetime of all known hyperons. The decay lengths are conveniently stated in units of length per GeV/c, since they are proportional to momentum. For Σ^-, the decay length is 3.71 cm/GeV/c; for Ξ^-, 3.75; for Ω^-, 2.3 $^{+.53}_{-.35}$; and for Σ^+, 2.00 cm/GeV/c. At 150 GeV/c the Σ^- decay length is thus 5.67 meters, and at 400 GeV/c it is 14.8 meters. At 400 GeV/c one can think in terms of 40 to 50 meter beams of sigmas. The omega decay length imposes a more stringent constraint, since the yields are much lower and the lifetime more uncertain. The most stringent constraint arises at the lowest momentum at which it is desired to work. It is fortunate that the properties of Cerenkov detectors are such that

it is possible to design a flexible optical system to use small cone angles and greater lengths to give better resolution at high energies, and large cone angles and shorter lengths at low energies where the decay is more rapid.

C. Tagging

The ability to tag individual hyperons (absent in our BNL experiments) allows many experiments otherwise difficult or impossible. An example is the study of branching ratios among different decay modes, which is necessary, e.g., for a study of the $\Delta I = 1/2$ selection rule. It is this requirement that makes the use of a Cerenkov detector mandatory, despite the additional decay length introduced. However, it is important that the Cerenkov detector have a high efficiency for detecting beam particles; its acceptance should match, or at least approach the beam phase space, otherwise the study of rare particles like the omega is greatly handicapped.

The original dispersive beam first proposed[4] for the hyperon beam suffered severely from this difficulty; particles of a given momentum were parallel, but the dispersion meant that the direction varied with momentum, and this led to efforts to design special Cerenkov detectors of the image-dissecting type[5], that could cope with this problem. The need for this complexity has now been removed by the introduction of the achromatic beam, which will allow matching to the acceptance of a conventional Cerenkov detector.

D. Multiple Tagging

The tagging requirement introduces another possibility at the other end of the scale. The relative abundance of hyperons observed in the negative beam is expected to be about in the ratio 10^5, 10^3, 1, for Σ^-, Ξ^- and Ω^- respectively; in addition there is a large accompanying flux of pions and other junk. We must be able to tag each of these three hyperon components correctly. Multiple tagging is not needed for sigma or cascade detection; it would be most useful in allowing rare omega events to be accumulated while studying the more abundant particles.

Multiple tagging is useful in a negative sense, in that it can be used for anti-coincidence signals to give purer tagging signals. In this sense it is an important feature of Cerenkov counter design.

E. Mass Resolution

Aside from multiple tagging, the greatest difficulty arises in the need to distinguish particles whose masses are nearly the same and whose velocity differences are therefore small. The most difficult case is of course the separation of sigma from xi. The mass difference is only 10%, and the velocity differences at high energy eventually vanish; there is always a maximum momentum at which separation is feasible for any particular experimental setup. The angular separation $\Delta\theta$ at a cone angle θ is given by

$$\theta\Delta\theta = (m_\Xi^2 - m_\Sigma^2)/2E^2 = .156/E^2, \quad E \text{ in GeV/c, } \theta \text{ and } \Delta\theta \text{ in rad.}$$

As we will see, we should be able to separate Σ^- from Ξ^- up to at least 320 GeV/c.

II. DESIGN OF THE BEAM TRANSPORT

A. <u>Procedure</u>

The procedure used to investigate the beam design has been as follows:

1) Use of the beam-optimizing program TRANSPORT to determine the magnet characteristics to achieve desired beam performance. TRANSPORT will optimize on any well defined beam parameter, subject to a large variety of constraints. One can specify the proton target dimensions, the acceptable hyperon solid angle, momentum range, and the focusing requirements; magnet aberrations, slits, misalignments, etc. can be introduced; and both first and second order calculations can be made.

2) A necessary supplement to TRANSPORT is TURTLE, a ray-tracing routine which verifies and amplifies the predictions of TRANSPORT by actually tracing rays through the system. TURTLE assumes lumped beam elements whose properties can be described in the usual multipole expansions. To the extent that the beam conforms to these assumptions, its output is correct to all orders. The histogramming facilities of TURTLE allow the phase space if the beam anywhere in the system is to be accurately pictured.

3) In addition to the calculation of the beam phase-space parameters, it is also important to determine the flux of background muons that inevitably accompanies any proton target bombardment. In the case of the relatively short hyperon beam this presents special difficulties, since without corrective action the detectors could readily be swamped by high energy muons

impossible to absorb. For this purpose we have adapted to our use the CERN program HALO, which can trace muons arising from pion or kaon decay through any beam transport system using standard transport magnets for which a map of the magnetic field can be supplied. Unfortunately the repertory of standard magnets is based on standard CERN designs, and does not include all the design types one would like to try. For our purposes, it was found necessary to modify HALO by adding a provision to include muons produced directly in the target by the primary protons. At high transverse momenta, such muons are known to be present to an abundance of 2×10^{-4} as compared with the pions; we have assumed the same ratio for the forward direction as well.[*] Thus for high-energy pions which enter the beam dump, and which have available only a short decay path, the relative contribution to the muon halo of the directly produced muons will exceed that of the pion decay for energies above 90 d GeV, where d is the decay path in meters.

In order to carry out the HALO calculations, it is necessary to have a fairly accurate idea of the actual iron configurations of the magnets used. This is especially important for the high

_____

[*] Note added in proof. New data from Adair et al. (private communication[8]) have just been received, which indicate lower yields in the forward direction by factors of 2 to 5, depending on the muon energy. They arrived too late to incorporate in the present report; their effect will clearly be to lower the predicted muon backgrounds by at least a factor of 2 for muons above 50 - 75 GeV/c.

energy muons, whose trajectory differs little from that of the main channel.

HALO also allows the insertion of muon absorbers and deflectors of various sorts, so that muon backgrounds can be minimized.

B.   Beam Layout

Figure II-1 shows a schematic of the proposed hyperon beam. The beam includes a momentum-selecting dipole, BM1, a quadrupole doublet Q1V and Q2H, a reverse bend BM2, and a focusing Cerenkov detector.

The reverse bend is due to a suggestion by C. M. Ankenbrandt[9], and significantly modifies the dispersive beam originally proposed[+] for Exp. 97. Without the reverse bend the beam may be characterized as a simple dispersive point-to-parallel focusing system, in which particles in a narrow momentum range are essentially parallel, but the beam is dispersed in direction according to their momentum. The introduction of the reverse bend has the effect of allowing the beam to be achromatized over a significant momentum range - several percent - so that the emergent beam is all effectively parallel within this range. The major advantage of this modification is the great simplification and increase of detection efficiency of the Cerenkov detector that follows. A much simpler, more or less conventional focusing detector can now be used, and the phase space of the beam will match its admittance. To achieve this in the dispersive beam required a rather elaborate image-dissecting system[5]. The achromatic design was apparently considered at one time by the CERN group, but abandoned for reasons not entirely clear to us.

The four magnets required would all have magnetic fields as large as can be conveniently achieved, so that their lengths can be minimized. For the required apertures, it appears that conventional quadrupoles would be about twice as long as super-conducting ones. For this and a variety of other reasons, including energy saving, initial cost, and operating cost, it seems desirable to look to superconducting magnet designs, and we have concentrated on these.
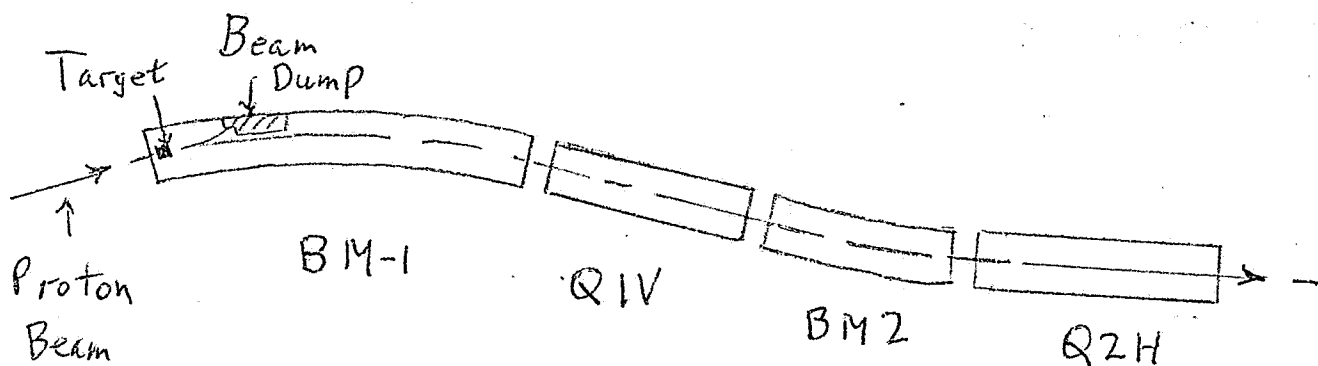
Fig. II-1. Achromatic Hyperon beam, schematic.

The superconducting quadrupole pair require as high a gradient as possible to keep the length down. The final value chosen for the gradient was 10 kgauss/cm (25 kgauss/in) which gives reasonable lengths and promises sufficiently small aberrations.

The first magnet, BM1, combines momentum selection, beam dumping, and muon deflection. It is patterned after a similar magnet[7] used, with much lower intensity proton beams, by experiment E8 in beam M2, for the production of neutral hyperon beams. BM1 is also subject to the constraint that if a superconducting coil is used, the thermal pulse due to radiation from the proton

target must not quench the superconductivity; this appears feasible. The total thermal load due to the beam likewise seems tolerable. The effects of radiation damage on the superconducting coil appear not to be important.

C.   Magnet Design: BM1

The length and field strength of BM1 are, in a sense, free parameters for the system; they are not critical. Since the overall shielding and, more important, the muon deflection, depend on them, an overall length of 7.0 m and a 30. kgauss field were decided on when the maximum hyperon momentum contemplated was 240 GeV/c. A few computations were made with a 5 m length; the overall savings in length was only 1.5 m, since longer focusing magnets were required. The longer value seemed desirable both for muon deflection and for shielding. The magnetic field was originally fixed at a conservative 30 kG.

As important as the narrow central field region is the secondary "weak" field region, in which the field is lower but where most of the flux is. This is the part of the magnet, filled with absorber, in which the major portion of the muon halo is deflected away from the downstream detection apparatus. Figure II-2 shows a cross-section of BM1 as presently conceived, and Fig. II-3 a detail of the coil cryostat.

The "weak" field region determines the momentum that muons must have to reach the return yoke before they leave the magnet. Muons that reach it will be deflected back toward the downstream detectors; this momentum limit should be as low as possible.
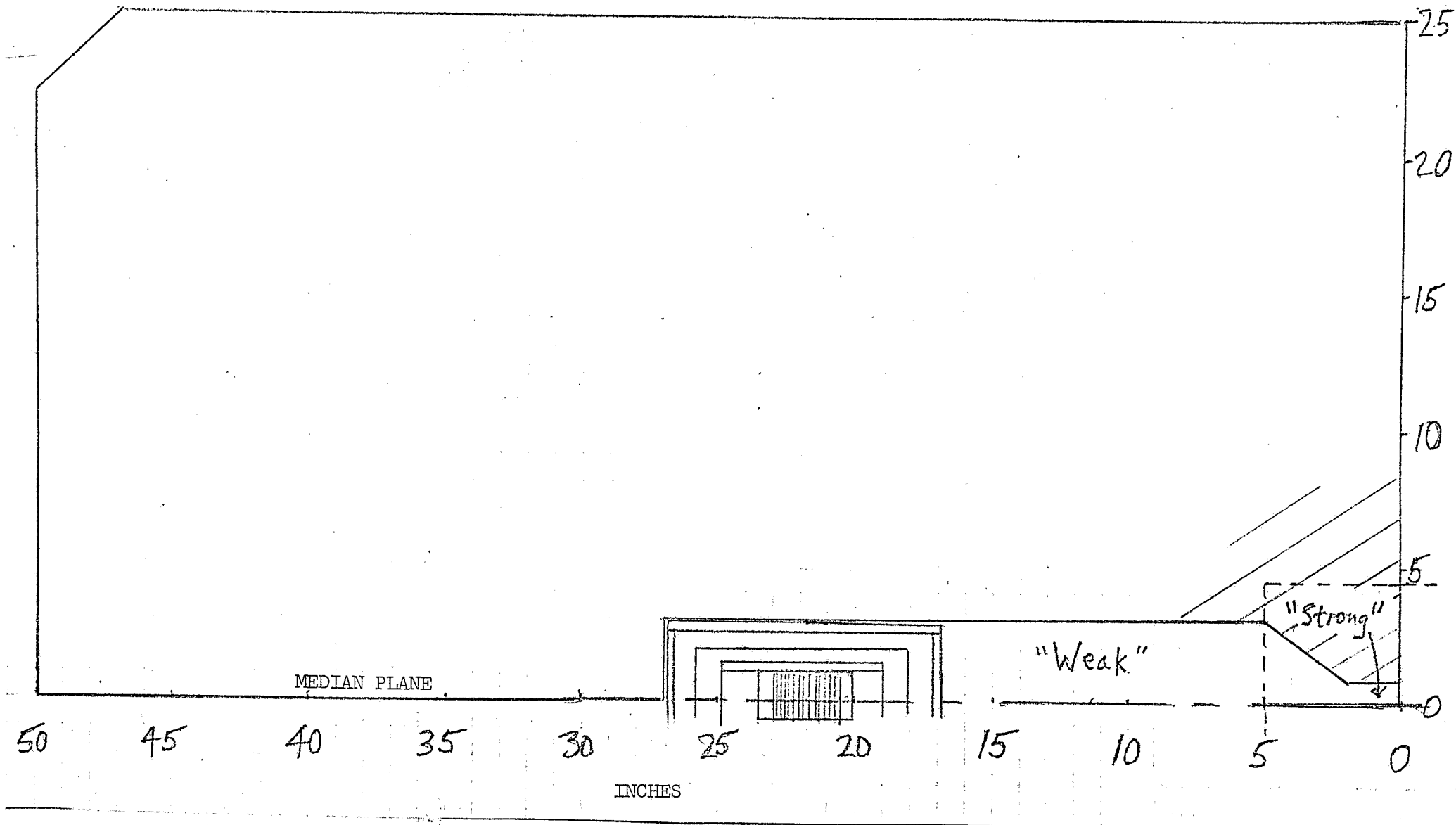
Fig. II-2. Cross-section of BM-1 as presently conceived. One quadrant only is shown. The magnet will separate in the median plane to allow assembly. The central region indicated by dotted lines should be interchangeable to allow target, beam dump, trajectory, and collimation changes. The sagitta of the trajectory is about 1 inch. The "weak" field region, about 19 kG, designed for muon deflection, will be filled with an absorbing material such as zinc. As shown, the magnet would weigh about 170 metric tons.

VACUUM

LIQUID NITROGEN
SHIELD

SUPERINSULATION

VACUUM

SUPERINSULATION

LIQUID HELIUM
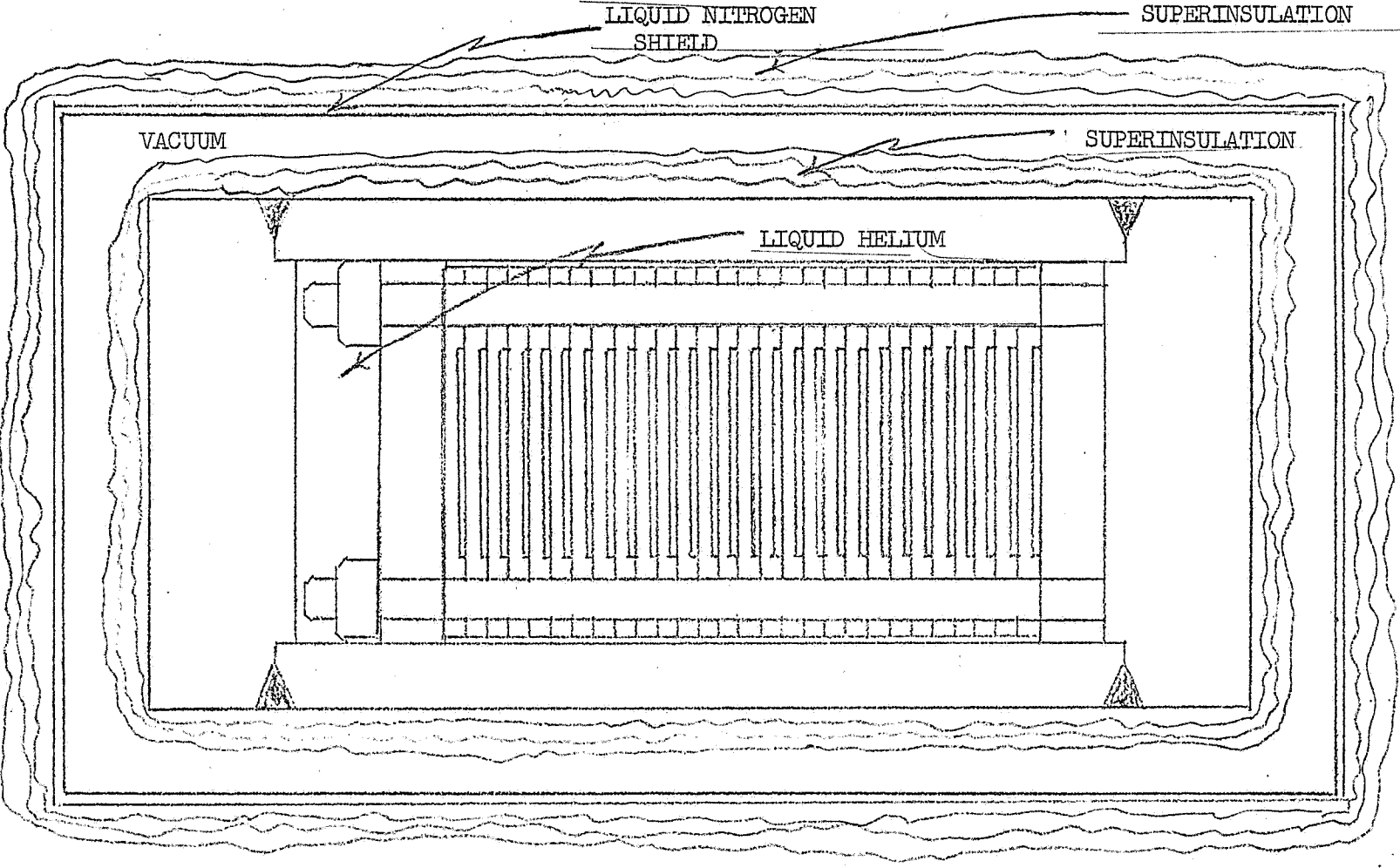
Fig. II-3. Typical Cryostat Cross-Section for Superconducting Dipole BM-1

In August 1975 it was decided, in view of probable developments in proton energy to extend the maximum energy of the secondary beam to 400 GeV/c. When this was done it turned out that the 30 kg field and 7 m length gave insufficient dispersion at 400 GeV/c to allow the design of a satisfactory slit system to limit the momentum acceptance. The possible remedies were to increase the length of the magnet or to increase its field. Since by far the greatest fraction of the flux in the magnet is devoted to muon deflection in the "weak" field region (see Fig. II-2) it proved to be possible to increase the field along the hyperon trajectory to 40 kgauss, which is sufficient for our needs.

Radiation Quenching

Figure II-4, for which we are indebted to A. Van Ginneken, shows the relative intensity contours for the energy deposited in a large iron beam dump by a 400 GeV/c proton. The contours represent the energy dissipated per unit volume, in GeV/cm^3 per incident 400 GeV/c proton. The maximum value at the coil location corresponds to 10^{-5} GeV/cm^3, or 1.6×10^{-15} joules/cm$^3 \cdot 400$ GeV proton. For a 10^{12} proton beam burst, this becomes $1.6 \cdot 10^{-3}$ joules/cm^3 pulse. For copper, density 9., specific heat $C_p = 1.0 \times 10^{-4}$ joules/gm. degree at 4° K, we find 1.75×10^{-4} joules/gm. pulse, giving rise to a temperature rise of just over a degree (the specific heat increases as the cube of the temperature). More important, the pulse is not short enough to be adiabatic provided the magnet is designed with a short thermal time constant. Unpublished experiments by G. Danby[10] on a magnet with a short

CONTOURS OF EQUAL STAR(ENERGY) DENSITY, IN UNITS OF STARS(GEV)/(CM3*INC.PTCLE)
CONTOURS ARE SHOWN FOR THE INTEGRAL POWERS OF 10

-17-

R A D I U S

D E P T H (CM)
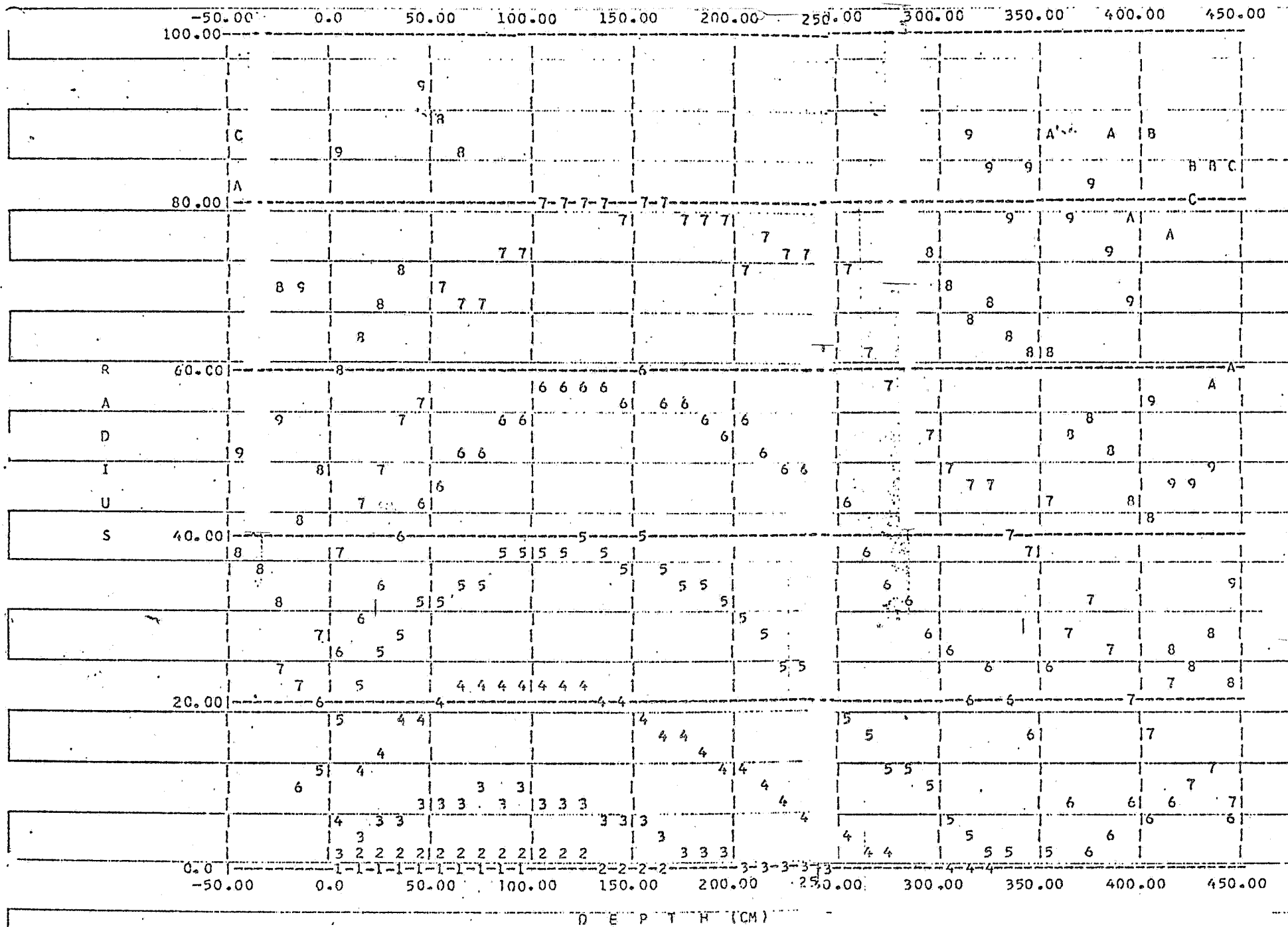
R-LABELS REFER TO SMALLER VALUES OF CORRESPONDING BINS
LEGEND : NUMERICAL SYMBOLS REFER TO THE NEGATIVE POWER OF 10 OF THE STAR(ENERGY) DENSITY E.G., 5 REFERS TO THE 10**-5 CONTOUR

Fig. II-4. Energy deposited in a large iron beam dump by a 400 Gev/c proton.

(~ 0.1 sec.) thermal time constant, using beams with a 1 sec. flat top, indicate that a safe limit is about 6. x 10^{-4} joules/gm. pulse, with quenching at 3.10^{-3} joules/gm. pulse. We conclude that a superconducting coil can be made and used safely. In practice the peak heat load may perhaps be reduced with local tungsten shielding in the weak field gap.

Radiation Damage

Superconductors are themselves not particularly susceptible to radiation damage, and the radiation levels in the coils are not thought to offer any hazard to the superconductor or to its associated copper and stainless steel supports. However, one must watch out for insulators, e.g., epoxy. If they cannot be entirely avoided, perhaps they can be kept out of the high intensity radiation regions.

Removable Central Region

Like its predecessor, it is envisaged that the central region of BM1, comprising perhaps four to eight inches to each side of the center line, and one or two inches of pole face, should be made so as to be removable. This would include a considerable portion of the beam dump, the target, the collimator and slit system. Thus a change of trajectory could be achieved with relative ease; and all critical alignments could be carried out on the bench in a radiation-free environment.

Neutral Beams

Since the sagitta of the charged hyperon beam is only an

inch or so, the use of BM1 as a sweeping magnet for a neutral beam appears straightforward. All that is required is to change the central beam section to one with a straight path and corresponding collimation.

D.   Quadrupole Pair

The quadrupole pair will have to be superconducting, or else the gradients will have to be drastically reduced, and the quads correspondingly longer. There seems to be no reason why they cannot be superconducting; magnets not too different from the ones proposed have been built at Argonne. At the exit of the bending magnet BM1 we are outside the beam dump, and radiation heating or damage is no longer a serious problem. A design that permits a useful aperture about 3 cm in diameter has been worked out, and is shown in Fig. II-5.

E.   BM2

Not too much attention has been given to BM2. It is assumed that the design of a uniform field dipole, with at most a 3-cm gap, and a 40-kG field, with a superconducting coil in a low radiation intensity environment, should not offer any great difficulties. It is desirable, though not essential, for it to be a C-magnet rather than an H-type, if possible; this will tend to decrease the muon flux refocused along the beam.

$B_o' = 25\,kG/in$

$N = 104\,turns/pole$

$I = 320\,A$

Iron

Y(in)

X(in)
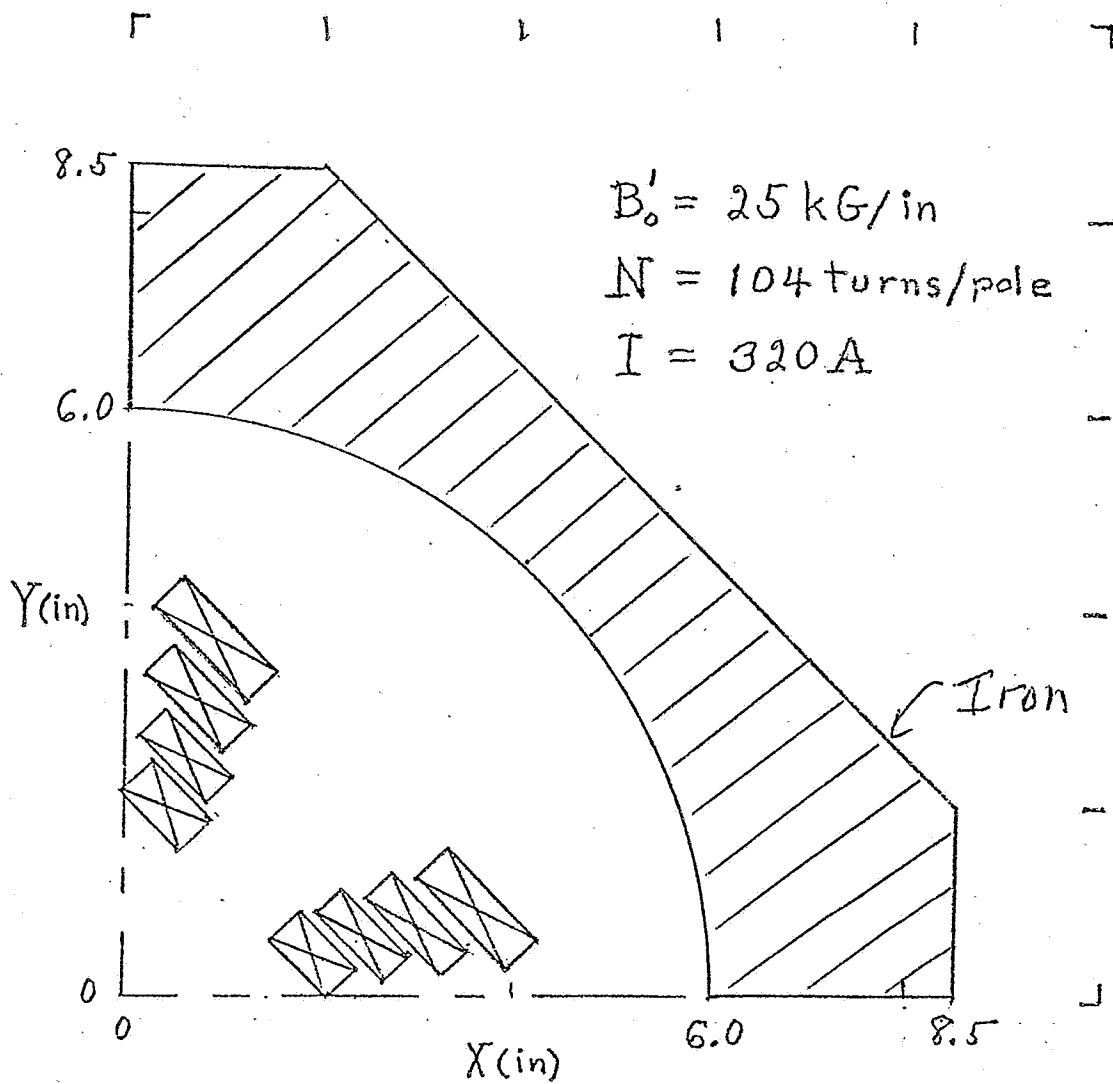
Fig. II-5. Superconducting Quadrupole Cross-Section (first quadrant only)

III. DETAILS OF BEAM TRANSPORT DESIGN

A. TRANSPORT Calculations

A fixed length and field, were postulated for the first
bending magnet, BM1. The order of the three remaining compon-
ents – the quadrupole pair and the reverse bend – was varied, and
it was determined that by far the best results came with the
vertical focusing quad first, and the horizontal focusing quad
last. The criterion for the design was to minimize simultaneously
the angular divergence of the outgoing beam and the momentum dis-
persion. The quantities specified were the dipole fields and the
quadrupole gradients and apertures. The quantities varied for
optimization were the lengths of the two quadrupoles and the
reverse bend. 0.2 m drift spaces separated all magnets.

B. TURTLE Calculations

Using the data for lengths thus supplied by TRANSPORT, runs
were made with TURTLE to plot the phase space occupied by the
beam at various points along it; at first with a "zero phase-
space" beam, in which the x, x', y, and y' ranges of the beam
were infinitesimal, and the momentum spread alone allowed to be
large; thus the focusing could be examined as a function of
momentum. To determine the effects of target size, proton beam
phase space, aperture and slit constraints, one then can simply
insert these quantities one at a time and observe the effect.
Figures III-1 to 6 show a set of such runs for the 400 GeV/c beam.
Second-order focusing was used in all runs.

TWO DIMENSIONAL PLOT OF XPR VS DP/P

```
                   -4.000      -1.500      1.000       3.500     TOTALS
                 I**___**___**___**___**___**___**__I_____
-.150 TO   -.145 I                                       I       0
-.145 TO   -.140 I                                       I       0
-.140 TO   -.135 I                                       I       0
-.135 TO   -.130 I                                       I       0
-.130 TO   -.125 I                                       I       0
-.125 TO   -.120 I                                       I       0
-.120 TO   -.115 I                                       I       0
-.115 TO   -.110 I                                       I       0
-.110 TO   -.105 I                                       I       0
-.105 TO   -.100 I                                       I       0
-.100 TO   -.095 I                                       I       0
-.095 TO   -.090 I                                       I       0
-.090 TO   -.085 I                                       I       0
-.085 TO   -.080 I                                       I       0
-.080 TO   -.075 I                                       I       0
-.075 TO   -.070 I                                       I       0
-.070 TO   -.065 I                                       I       0
-.065 TO   -.060 I                                       I       0
-.060 TO   -.055 I                                       I       0
-.055 TO   -.050 I $                                     I     157
-.050 TO   -.045 I $$                                    I     254
-.045 TO   -.040 I  $S                               $ I     472
-.040 TO   -.035 I  2$3                             $$ I     597
-.035 TO   -.030 I   P$1                           $$ I     628
-.030 TO   -.025 I    Z$1                         B$$ I     677
-.025 TO   -.020 I     S$I                       $$E I     768
-.020 TO   -.015 I      B$$                     $$ I     894
-.015 TO   -.010 I       $$4                   $$$ I    1034
-.010 TO   -.005 I      V$$G              $$$ I    1284
-.005 TO   -.000 I           N$$$$$$$$$$$$ I    2943
-.000 TO    .005 I              O$$F I     292
 .005 TO    .010 I                                       I       0
 .010 TO    .015 I                                       I       0
 .015 TO    .020 I                                       I       0
 .020 TO    .025 I                                       I       0
 .025 TO    .030 I                                       I       0
 .030 TO    .035 I                                       I       0
 .035 TO    .040 I                                       I       0
 .040 TO    .045 I                                       I       0
 .045 TO    .050 I                                       I       0
 .050 TO    .055 I                                       I       0
 .055 TO    .060 I                                       I       0
                 I**___**___**___**___**___**___**__I_____
                 I                                       I
                 I                                       I
                 I 3333333332233332333322332333333332 I
                 I 20110222078133182419802912200049 I
        TOTALS   I 69142668336134639557973055478528 I   .9999
```

TOTAL NUMBER OF ENTRIES = 10000 INCLUDING UNDERFLOW AND

Fig. III-1. Phase-space plot of x' vs momentum (in % dp/p).

"Zero" phase-space beam (point target).

25 cm Target, no slits

TWO DIMENSIONAL PLOT OF XPR VS DP/P

```
                    -4.000     -1.500      1.000      3.500     TOTALS
                    I**---**---**---**---**---**---**---**--I--------
 -.150 TO  -.145 I                                          I      0
 -.145 TO  -.140 I                                          I      0
 -.140 TO  -.135 I                                          I      0
 -.135 TO  -.130 I                                          I      0
 -.130 TO  -.125 I                                          I      0
 -.125 TO  -.120 I                                          I      0
 -.120 TO  -.115 I                                          I      0
 -.115 TO  -.110 I                                          I      0
 -.110 TO  -.105 I                                          I      0
 -.105 TO  -.100 I                                          I      0
 -.100 TO  -.095 I                                          I      0
 -.095 TO  -.090 I 11                                       I      2
 -.090 TO  -.085 I 1                                        I      1
 -.085 TO  -.080 I 911                              24      I     17
 -.080 TO  -.075 I 7822                            155      I     30
 -.075 TO  -.070 I E9981                          14AG     I     72
 -.070 TO  -.065 I HG9861                        122GE     I     92
 -.065 TO  -.060 I KLC845                        449FC     I    114
 -.060 TO  -.055 I KDFFDA4                      1387D<J    I    161
 -.055 TO  -.050 I FVPFNJ62                     59AEMKK    I    236
 -.050 TO  -.045 I HNUSEIA54                   138GAEKUE   I    265
 -.045 TO  -.040 I OKMRNPIA711                 34CCVMWTZ   I    350
 -.040 TO  -.035 I OPOVOMHH8321               1399CVOVSWQ  I    404
 -.035 TO  -.030 I PORUSFYOE855              1149FOVPPYQIM I    467
 -.030 TO  -.025 I SNOKRKSZIJJIE2            35BEJVQPVXZJQK I   597
 -.025 TO  -.020 I KJJJOSPTNNILJ85473FDMRS4SWZUKUHB I     673
 -.020 TO  -.015 I CEIHVUUSYXSXJROMRQSUPXWXVEXWSMTG I     878
 -.015 TO  -.010 I 6BFHMTSSSTBSSSSYSZSSTSSZVSSSTSFKE I    1009
 -.010 TO  -.005 I 58GLOLQXSPWXSSSSSSZYSSSSSARRKJAH I     974
 -.005 TO  -.000 I 399ENIPTXSZSSSSSSSSSSSSUSJVEIA94 I     931
 -.000 TO   .005 I 346A3JLPUQSSSSSWSSSSSWSKPRLLBA78 I     879
  .005 TO   .010 I 2 87CECFNONYSSSSSSSSSRXSRLGSA8621 I    705
  .010 TO   .015 I   223F9BGMVUSXSYZSSUKNID7345535 I      521
  .015 TO   .020 I   32238A89FIKRTNONEODB7986312   I      322
  .020 TO   .025 I    1 1 3445A78AA6935A43433 3    I      118
  .025 TO   .030 I      1   3112 1            1     I       10
  .030 TO   .035 I                                 I        0
  .035 TO   .040 I                                 I        0
  .040 TO   .045 I                                 I        0
  .045 TO   .050 I                                 I        0
                 I**---**---**---**---**---**---**---**--I--------
                 I                                        I
                 I                                        I
                 I 2223233332233332333223323333333232 I
                 I 7890922207313318241980291220 0927 I
          TOTALS I 30717668335134639557973055474128 I   9828
```

TOTAL NUMBER OF ENTRIES =   9828 INCLUDING UNDERFLOW AND

Fig. III-2. Same as Fig. III-1, with 25-cm target, no momentum-defining slits.

25 cm target, with slits

TWO DIMENSIONAL PLOT OF XPR VS DP/P

			-4.000	-1.500	1.000	3.500		TOTALS
			I**---**---**---**---**---**---**--I---------					
-.150	TO	-.143 I					I	0
-.143	TO	-.135 I					I	0
-.135	TO	-.128 I					I	0
-.128	TO	-.120 I					I	0
-.120	TO	-.113 I					I	0
-.113	TO	-.105 I					I	0
-.105	TO	-.097 I					I	0
-.097	TO	-.090 I					I	0
-.090	TO	-.082 I					I	0
-.082	TO	-.075 I					I	0
-.075	TO	-.067 I					I	0
-.067	TO	-.060 I					I	0
-.060	TO	-.052 I					I	0
-.052	TO	-.045 I					I	0
-.045	TO	-.037 I					I	0
-.037	TO	-.030 I	1 1				I	2
-.030	TO	-.022 I	1121421 43 11 1 211232 3221				I	41
-.022	TO	-.015 I	57789E696G8AI49373577C769541733				I	239
-.015	TO	-.007 I	3A6C7EJKJILPLOMMN0FJLJGGF46465				I	461
-.007	TO	.000 I	499EFBJKNOWROUPSZNUIC9DC7F2695				I	510
.000	TO	.008 I	5736FIELOOVVMPNKVLGKCD9398475				I	452
.008	TO	.015 I	124B839JMMJRGXVOKHCFC978843				I	366
.015	TO	.023 I	1 34337DAGGEC887354411				I	143
.023	TO	.030 I	4 1				I	5
.030	TO	.038 I					I	0
.038	TO	.045 I					I	0
.045	TO	.053 I					I	0
.053	TO	.060 I					I	0
		I**---**---**---**---**---**---**--I---------						
		I					I	
		I					I	
		I	111111111				I	
		I	224356779912121221088666442221				I	
	TOTALS	I	294817438619775039807874901666983				I	2219

TOTAL NUMBER OF ENTRIES =   2219 INCLUDING UNDERFLOW AND

Fig. III-3. Same as Fig. III-2, with addition of momentum-defining slits.

TWO DIMENSIONAL PLOT OF YPR VS DP/P

```
                    -4.000      -1.500      1.000      3.500    TOTALS
                    I**---**---**---**---**---**---**--I--------
 -.150 TO   -.140  I                                           I        0
 -.140 TO   -.130  I                                           I        0
 -.130 TO   -.120  I                                           I        0
 -.120 TO   -.110  I                                           I        0
 -.110 TO   -.100  I                                           I        0
 -.100 TO   -.090  I                                           I        0
 -.090 TO   -.080  I                                           I        0
 -.080 TO   -.070  I                                           I        0
 -.070 TO   -.060  I                                           I        0
 -.060 TO   -.050  I                                           I        0
 -.050 TO   -.040  I                                           I        0
 -.040 TO   -.030  I                                           I        0
 -.030 TO   -.020  I                                           I        0
 -.020 TO   -.010  I                                           I        0
 -.010 TO    .000  I $$$$$$$$$$$$$$$$$$$$$$$$$$$$$$$$$$$$$$$  I     5060
  .000 TO    .010  I $$$$$$$$$$$$$$$$$$$$$$$$$$$$$$$$$$$$$$$  I     4940
  .010 TO    .020  I $$$$$$$$$$$$$$$$$$$$$$$$$$$$$$$$$$$$$$$  I     4940
  .020 TO    .030  I                                           I        0
  .030 TO    .040  I                                           I        0
  .040 TO    .050  I                                           I        0
  .050 TO    .060  I                                           I        0
  .060 TO    .070  I                                           I        0
  .070 TO    .080  I                                           I        0
  .080 TO    .090  I                                           I        0
  .090 TO    .100  I                                           I        0
  .100 TO    .110  I                                           I        0
  .110 TO    .120  I                                           I        0
  .120 TO    .130  I                                           I        0
  .130 TO    .140  I                                           I        0
  .140 TO    .150  I                                           I        0
                    I**---**---**---**---**---**---**--I--------
                    I                                           I
                    I                                           I
                    I 3333333332233332333223323333332  I
                    I 20110222078133182419802312200049 I
        TOTALS      I 69142668336134639557973055478528 I     9999
```

TOTAL NUMBER OF ENTRIES =   10000 INCLUDING UNDERFLOW AND

Fig. III-4. Phase-space plot of y' vs. momentum (in % dp/p).

"Zero" phase-space beam (point target).

25 cm target   no slits

TWO DIMENSIONAL PLOT OF YPR V'S DP/P

		-4.000	-1.500	1.000	3.500	TOTALS
		I**---**---**---**---**---**---I				
-.200 TO	-.190	I				
-.190 TO	-.180	I			I	0
-.180 TO	-.170	I			I	0
-.170 TO	-.160	I			I	0
-.160 TO	-.150	I			I	0
-.150 TO	-.140	I			I	0
-.140 TO	-.130	I			I	0
-.130 TO	-.120	I			I	0
-.120 TO	-.110	I			I	0
-.110 TO	-.100	I			I	0
-.100 TO	-.090	I			I	0
-.090 TO	-.080	I 44 1			I	0
-.080 TO	-.070	I 5611		1	I	10
-.070 TO	-.060	I B3873421		2 135	I	24
-.060 TO	-.050	I DD6A967331		1 436BB	I	75
-.050 TO	-.040	I DD6A967331	12434589DD		I	142
-.050 TO	-.040	I CHFDJGEJ353 2	1 58509GIKPG		I	281
-.040 TO	-.030	I MTSHOLKTPFJFAA5 4798MI4FBTORNESR			I	572
-.030 TO	-.020	I LNQUSIWWOUWVRV$S$$$UXOVZ$SJZPL$J			I	960
-.020 TO	-.010	I KRUYX$$$$SZ $$$$$$$$$$$$$$$$$V$NJ			I	1337
-.010 TO	.000	I UGUXX$$$$$$$$$$$$$$$$$$$$$$$$$JTRYO			I	1521
.000 TO	.010	I LVTXN$$$$$$$$$$$$$$$$$$$$$$$$V$ZSX			I	1546
.010 TO	.020	I OUSTZ$$$$$$$$$$$$$$$$$$$$$$$Y$$$$$O4W			I	1310
.020 TO	.030	I I4UMNNSUTW$V$$$$W$ORZJQ$TSUWQI			I	980
.030 TO	.040	I LJKRKNRJIHAB3671345ACIE9MIOVS$BH			I	520
.040 TO	.050	I JKHGJI879431 137B3AHFGHJM			I	290
.050 TO	.060	I HBFG3A6421 125AA8I9			I	158
.060 TO	.070	I 748A2511 1454499			I	74
.070 TO	.080	I 6352 123			I	22
.080 TO	.090	I 221 1			I	6
.090 TO	.100	I			I	0
.100 TO	.110	I			I	0
.110 TO	.120	I			I	0
.120 TO	.130	I			I	0
.130 TO	.140	I			I	0
.140 TO	.150	I			I	0
.150 TO	.160	I			I	0
.160 TO	.170	I			I	0
.170 TO	.180	I			I	0
.180 TO	.190	I			I	0
.190 TO	.200	I			I	0

```
        I**---**---**---**---**---**---**--I-------
        I                                  I
        I                                  I
        I                                  I
        I 222323332233332333322332333333232 I
        I 789092220781331824198029122000927 I
TOTALS  I 30717653361346395379730554744128 I   9828
```

TOTAL NUMBER OF ENTRIES = 9828 INCLUDING UNDERFLOW AND

Fig. III-5. Same as Fig. III-4, with 25-cm target, no momentum-defining slits.

25 cm target, with slits

TWO DIMENSIONAL PLOT OF YPR VS DP/P

```
                  -4.000      -1.500      1.000      3.500    TOTALS
                I**---*---**---*---**---**---**---I------
-.150 TO  -.140 I                                          I      0
-.140 TO  -.130 I                                          I      0
-.130 TO  -.120 I                                          I      0
-.120 TO  -.110 I                                          I      0
-.110 TO  -.100 I                                          I      0
-.100 TO  -.090 I                                          I      0
-.090 TO  -.080 I                                          I      0
-.080 TO  -.070 I                                          I      0
-.070 TO  -.060 I     11    1                  1 1         I      5
-.060 TO  -.050 I    1  2 421              331 11 1        I     20
-.050 TO  -.040 I     2 3114223       126243 11            I     38
-.040 TO  -.030 I     2 43392796345 114422424411223       I     94
-.030 TO  -.020 I  143424264G8FEHHBECDH9AB4554144          I    242
-.020 TO  -.010 I  12266677EBFJMJNRJTIGDF57543363          I    335
-.010 TO   .000 I  11251778JACMHPURKOKJEFJEA7852463        I    384
 .000 TO   .010 I   436477EGHMJOILL$3NOMFAFA371254         I    416
 .010 TO   .020 I 1322157AB989KNFFPKIFH775978764 2         I    299
 .020 TO   .030 I 134838697ABGD8F7CGBBC6459275 11          I    231
 .030 TO   .040 I 11442445324723211355525554 31231         I     95
 .040 TO   .050 I   122233 4321      2 13331163121          I     50
 .050 TO   .060 I    1 2 11               1 21             I      9
 .060 TO   .070 I    1                                     I      1
 .070 TO   .080 I                                          I      0
 .080 TO   .090 I                                          I      0
 .090 TO   .100 I                                          I      0
 .100 TO   .110 I                                          I      0
 .110 TO   .120 I                                          I      0
 .120 TO   .130 I                                          I      0
 .130 TO   .140 I                                          I      0
 .140 TO   .150 I                                          I      0
                I**---**---**---**---**---**---**---I------
                I                                          I
                I                                          I
                I             111111111                    I
                I    224356779912121221088556442221        I
         TOTALS I 2948174386197750398078743015б983         I   2219

         TOTAL NUMBER OF ENTRIES =        2219 INCLUDING UNDERFLOW AND
```

Fig. III-6. Same as Fig. III-5, with addition of momentum-defining slits.

In addition the effects of magnet aberrations or imperfections could be investigated, as well as end effects and the effects of various beam misaligments.

C. RAYTRACE Calculations

Since TURTLE is a matrix procedure using lumped elements, it does not handle end effects and fringing fields explicitly for quadrupoles (it can of course include edge focusing effects for dipoles.) Since the required parallelism of the output beam is rather stringent, it was thought to be worth while to check the results of TURTLE by means of a ray-tracing program, which would automatically be correct to all orders, since it simply integrates the Lorentz equations of motion. The only limit with such a program is that involved in specifying the field accurately enough.

An MIT ray-tracing program, which we renamed RAYTRACE, furnished by S. Kowalski, was used for this purpose. The program is not designed for high energy physics use, but for spectrometers in the 1 GeV region; consequently it is set up with rather different objectives in mind. However, it was found to be usable. The axial rays give results identical to those of TURTLE. The results of other rays, selected to sample the phase space, were in good agreement with TURTLE results. This indicates that the fringing field effects are essentially negligible.

D. HALO Calculations

The muon background at the downstream detector position was

investigated by forcing decay of all pions at 0.5 meters from the target. As explained above, it was necessary to add directly produced muons, since they constitute the largest part of the background above 50 to 100 GeV. The design of BM1 is such that all low energy muons are deflected far away from the spectrometer detectors. Only the highest energy muons, which closely parallel the hyperon beam and traverse the hyperon beam transport magnets, contribute to the final background. There is a small flux of very low energy muons (15 GeV and less) that reach the return yoke of BM1 and are deflected back toward the detectors; few in number, they have been ignored). Filling the gap of BM1 with an absorber like Cu or Zn has the beneficial effect of degrading and scattering the muons, thus decreasing the background.

The HALO calculations show that the greatest flux of interfering particles at the downstream detectors is found when the hyperon beam is tuned to energies considerably lower than the incident beam energy, i.e., at low values of alpha. In view of these findings, it is not necessary to consider adding special muon deflecting magnets or shields at this time. The major background is that which traverses the iron of the beam transport magnets. It is of relatively high momentum; in fact, near the hyperon momentum.

Figure III-7 indicates the result of a 150 GeV/c HALO run (α = 0.5) with all beam magnets in place, with 300 GeV/c protons incident. The plot indicates the geometrical location of halo particles striking a detector plane 52.8 m downstream from the

HISTOGRAM NO. 3
HORIZONTAL AXIS... X   IN MM   .FOR HALO AT   DATE 07/23/75
VERTICAL AXIS... Y   IN MM   .FOR HALO AT   52.790 M   (POSITION NO. 11)
FLAGS = F5   52.790 M   (POSITION NO. 11)

Fig. III-7. Muon halo background at a detector plane 52.8 m downstream from the target. Proton beam 300 Gev/c, hyperon beam. 150 Gev/c. Horizontal and vertical cooridinates in mm. One halo particle represents 1000 muons. The origin is the intersection of the central beam ray with the detector plane.

target. The coordinates are in mm, the origin at the location of the transmitted hyperon beam. Each halo particle represents 1000 muons; the beam is 3.3×10^{11} interacting protons.

We see that the peak intensity, between ± 100 mm points, reaches 25 halo particles or 2.5×10^4 muons in a strip 2 cm wide by 60 cm high at the location of the primary beam. If this is the area covered by a single drift-chamber collecting wire, it indicates that the peak background muon flux averages one particle every 40 μsec during the beam spill. A 10 cm lateral displacement will reduce this peak value by a factor of 5. The muon halo spectrum ranges from about 60 to 230 GeV/c, peaking around 110. As noted above, the new data of Adair et al.,[8] indicate that the above numbers are too high by at least a factor of 2.

IV. RESULTS OF BEAM DESIGN CALCULATIONS

Three different momenta were used in the principal phase of the design study, and TRANSPORT calculations made for them; most of the preliminary work was done at 240 GeV/c. The major beam parameters obtained are shown in Table IV-1. The quadrupole gradients were 10 kgauss/cm., the bending magnet fields 30 kgauss. Elements are separated by 0.2 m drift spaces.

As may be seen from Table IV-1, the change in field in the dipoles from 400a to 400b does not change the beam optics or magnet lengths. The desired improvement in dispersion is evident only when slits are inserted.

TABLE IV-1

A. Magnet lengths in meters, deflection angles in degrees,
    for the Achromatic beam, with zero phase space. 400a
    and 400b refer respectively to runs with the dipoles
    at 30 and 40 kgauss respectively

Beam Element	Momentum, GeV/c			
	240	320	400a (30 kG)	400b (40 kG)
BM1	7.00	7.00	7.00	7.00
Q1V	1.959	2.540	3.092	3.092
BM2	1.699	1.584	1.486	1.486
Q2H	1.319	1.673	1.996	1.995
Bend, BM1	1.503	1.127	.902	1.203
Bend, BM2	-.365	-.255	-.192	-.256
Total Bend	1.138	.872	.710	.947
Total Beam Length	12.58	13.40	14.17	14.17

B. Parameters for Achromatic Focusing

Momentum, GeV/c	a	b	c
240	0.002	.0012	.0037
320	.002	.0014	.0028
400a	.002	.0006	.0023
400b	.002	.0016	.0032

The parameters for achromatic focusing a, b, and c refer

to the empirical equation representing x' focusing:

$$x' = a + by + cy^2 \qquad\qquad (IV-1)$$

where y represents percent momentum deviation from the central

value, and x' is in mrad. The momentum values y at which x'

reaches a given value V can be obtained by solving the equation

$$y = -b/2c \pm (b^2 + 4 \ vc)^{1/2}/2c \qquad\qquad (IV-2)$$

E.G., for x' = -.018 at 320 GeV/c, which gives a total span of

x' of .020 mrad, we find the two values of y are +2.93, - 2.43

(for a zero size target).

It is noteworthy that the rate of change of overall length

of the beam with the energy between 240 and 400 GeV/c is almost

exactly 1.00 cm per GeV/c. But, as we have seen, the decay

lengths of all the hyperons exceed 2. cm/GeV/c. Thus the fraction

of hyperons decaying in the beam decreases with increasing energy.

A.   Contributions to Beam Phase Space from Target Dimensions

and Proton Divergence

Target Size

The parabola (Eq. IV-1), representing the variation of x'

with momentum, defines the achromatic focusing property of the

beam. The other beam properties are simpler; The mean x coordi-

nate at the output, $\bar{x}_4$, changes almost linearly with momentum;

y and y' do not change. The x_4 dispersion may be characterized

as follows:

TABLE IV-2

Dispersion at End of Beam

Momentum GeV/c	Rate of Change of x_4 with Momentum
240	-0.35 cm/% dp/p
320	-0.30 cm/%
400	-0.24 cm/%

These numbers are relevant to the measurement of individual particle momenta in the beam, as we will see later on.

To determine the effect of target size, the point of origin of the beam was displaced from the origin of coordinates in one dimension and the effect on the beam dimension observed. As might be anticipated, x affects mainly the conjugate coordinate x', and similarly y mainly y'. The coupling between x and y is very small. In like fashion, x' determines final x and y' the final y. The effect of target height and width can be summarized as follows:

TABLE IV-3

Variation of Beam Divergence with

Target Parameters

	E, GeV/c = 240	320	400
a. Variation of x' with horizontal target displacement x, = x"	x" = .05 mr/mm	.044	.044
b. Variation of y' with verticle target displacement y, = y"	y" = .20 mr/mm	.20	.20

Target Length

Investigation of the effect of target length on focusing

properties shows that there is practically no observable effect

from moving the source axially 10 cm in either direction from

its initial position at the entrance to BM1. However, there is

another important effect, in that the effective target height

and width change with location along the target if the primary

proton beam is not perfectly parallel - which of course it is not.
This is illustrated in Fig. IV-1.

Proton Beam Phase Space

Table IV-4 shows values quoted to us as nominal optimum

values to use for the phase space of the incident proton beam

in Proton Central[11]. They can be expected to show variations,

of perhaps as much as a factor of 2.

Fig. IV-1. Target illumination by the incident proton beam.

TABLE IV-4

Proton-Central Beam Phase Space

Horizontal proton beam admittance:

Phase space area 0.25π mm. mrad

Vertical proton beam admittance:

Phase space area 0.10π mm. mrad

It can be shown that the minimum contribution to secondary beam

angular width will be obtained when the contributions due indi-

vidually to minimum beam height and to increase of height in the

target (because of primary beam angular divergence) are equal.

Thus optimum shape of the primary beam phase space will depend

upon the target length as shown in Fig. IV-1. Table IV-5 shows

the contribution to angular spread in y' due to target length l,

and thickness t, and in x' due to target width, assuming the

contribution suitably minimized. Y_o and θ_y are the coordinates

of the proton beam vertical phase space, x_o and θ_x of the hori-

zontal.

TABLE IV-5

Contributions to Angular Divergence

from Target Length

A. Vertical Divergence: $y'' = 0.20$ mrad/mm (at all energies)

Length, l	y_o	θ_y	t	y'
100 mm	0.1 mm	1.0 mr	0.2 mm	0.04 mr
200 mm	.14	.707	.28	.056
250 mm	.157	.64	.314	.063

B. Horizontal Divergence: Take $x'' = 0.048$ mr/mm as average at all energies

Length, l	x_o	θ_x	t	x'
100 mm	.158 mm	1.6 mr	.316 mm	.016 mr
200 mm	.224	1.1	.45	.022
250 mm	.25	1.0	.50	.024

These contributions are quite unequal, due to the much greater sensitivity of the beam to vertical height than to horizontal width. There is, however, another source of divergence that contributes to horizontal width alone, thus tending to equalize the divergence. As we have seen, this is the beam momentum spread and the imperfect achromatization.

Proton Beam Steering

Since the secondary beam is so narrow, it will clearly be
necessary to provide steering magnets to allow the proton beam
to be accurately directed at the target. Control of both position
and direction will be required.

B.   Contributions due to Momentum Width

The momentum width permitted in the beam contributes to the
loss of angular resolution in two ways. One is the failure to
achieve perfect achromatization described above; the other is a
change of radius of the Cerenkov ring, since the cone angle is a
direct function of particle velocity. This decreases the separa-
tion of particles of different masses.

Table IV-6 summarizes these effects at 240 GeV. At higher
energies these quantities are somewhat reduced.

TABLE IV-6

Effects of Target and Beam Size and Momentum

Spread at 240 GeV

Target Size: 250 mm x 1 mm x .32 mm. Values shown
               are full widths at about 90% area.

$\Delta x'$ min	.05 m
$\Delta x'$ for ± 2% δp	.065
$\Delta x'$ for ± 3% δp	~ .08
$\Delta y'$ min	.06
$\Delta y'$ for ± 2% δp	.07
$\Delta y'$ for ± 3% δp	~ .08

C. Effects of Magnet Imperfections

   1) Dipoles

The effect of sextupole components in the two dipole fields was investigated. In BM2 a sextupole has a much smaller effect than in BM1, as might be expected; an amplitude of .001 (0.1% field error 1 cm from orbit) was unnoticeable. A sextupole field of amplitude .001 in BM1, on the other hand, increased the defocusing of off-momentum particles by a factor between 2 and 2.5; it acts to decrease the achromatization by about 30%. The effect can be seen in Table IV-7, which shows how the focusing is affected. For this table, the value of x', the horizontal angular coordinate, is treated as a parabola, as we did above in discussing achromatic focusing. The result of the sextupole aberration is to change the coefficients of the parabola.

TABLE IV-7

Sextupole Effect on Achromatization at

240 GeV/c

Parameter	a	b	c
No sextupole	.002	.0012	−.0037
Sextupole = .001	.002	.0039	−.0075

An x' range of .03 mr allows a 5.7% $\delta p/p$ range with no sextupole; 4.0% $\delta p/p$, 30% narrower, with .001 sextupole.

   2) Quadrupole Imperfections

Sextupole components in the quadrupole field had similar but much smaller effects. In addition, the effect is sensitive to

the phase of the quadrupole field (rotation) with respect to the sextupole field; it is much smaller when the two are in phase. The major effect was the introduction of a slight variation in the mean y' with momentum; but this is much smaller than the spread in y' from other causes.

D. Effect of Misalignments

We have investigated the effect of displacements and rotations on individual magnets, and on the beam as a whole (excluding BM1 which is regarded as fixed.) Displacements and rotations cause angular displacements and tilts, respectively; the effect when the entire transport (two quads and BM2) is simultaneously displaced being a third to a quarter as great as the effect of the single most sensitive component, which depends on the coordinate examined. It is therefore highly desirable that the two quads and the bending magnet, which have an overall length of about 7 meters, be mounted upon a single fixed base, and individually aligned with respect to it; then motions of the base will have much less effect on the particle beam. Displacements of 0.5 mm have noticeable effects on the beam direction; the y displacement is much more sensitive than x, as is to be expected from the target sensitivity. It will be necessary to provide means for monitoring and adjusting the beam transport location.

Table IV-8 shows the effect of some misalignments. Small changes in mean direction x' and y' are of little consequence; such small displacements provide a method for steering the beam accurately. Large changes introduce chromatic effects which should be avoided.

TABLE IV-8

Effects of Misalignment of Entire Beam

Misalignment	Momentum, GeV		
	240	320	400
x displacement = 1. mm (entire beam)	x' shift = -.05 mrad	x' shift = -.046 mr	x' shift = -.042 mr
y displacement = 1.0 mm	y' shift = -.21 mr	y' shift = -.20 mr	y' shift = -.19 mr
Rotation, 1. degree	y slope = .0025 cm/1% dp/p	y slope = .0025 cm/1% dp/p	y slope = .0025 cm/1% dp/p
	y' slope = .003 mr/1% dp/p	y' slope = .0022 mr/1% dp/p	y' slope = .0018 mr/1% dp/p

E.   Determination of Individual Particle Momenta

As anticipated in our preliminary report, it has proved to be possible to determine the momenta of individual particles in the beam by correlating their x coordinates at two points in the beam. It turns out the best place to make these observations is at x_1, just after BM1, and x_4, at the end of the beam transport, at the entrance to the Cerenkov counter. Accurate location at the latter point is required in any case to obtain the final particle direction. The correlation is capable of yielding reasonably good accuracy in momentum, provided one has detector planes of sufficient accuracy. Table IV-9 shows the precision obtained with a 25 cm. target. The width is due almost entirely to target size; the resolution can readily be improved by reducing the target size.

TABLE IV-9

Momentum Resolution at 240 GeV/c

from x_1, x_4

All runs made with 25 cm. target:

    1.4 mm slit at 3.5 m, 2.8 mm slit at 7. m,
7. mm slit after BM2.

FWHM in x_1 at a single momentum: 0.014 cm.

$(\Delta x_1/\delta p/p)_{x_4 = constant}$:   0.023 cm/1% $\delta p/p$

Momentum resolution: 0.014/.023 = 0.6%
                                    FWHM

F.   Beam Solid Angle, Acceptance, and Particle Yields

To calculate the flux of secondary particles in a given beam it is necessary to know the production function, and the solid angle. No direct data on charged hyperon production at Fermilab energies is available; the highest energies for which production data are available is 31 GeV, from our BNL run. In addition there are now some data on neutral hyperon production at Fermilab. For the purposes of this report the direct production cross-sections can be taken as those predicted by the Wang formula[13], with sufficient accuracy. This is most useful not only for the overall yield functions, but for the angular distributions as well. At the energies under consideration the yield falls off so rapidly with angle that it is easy to design beams with angular acceptances large compared to the width of the angular distributions.

Figure IV-1 (p. 37) shows the target illumination produced by the divergent proton beam. The horizontal spread of the proton beam is large (± 1. mrad) compared to the secondary beam acceptance (less than 0.5 mrad) so that the secondary beam phase space is uniformly filled, though not with equal efficiency, by all incoming protons. However, the proton beam divergence in the vertical plane is only ± 0.64 mrad for a 250 mm long target, and 1. mrad for a 100 mm target. These numbers are small compared with the acceptance possible in the vertical plane, which is at least ± 2.0 mrad. Table IV-10 shows the angular distribution function in the Wang production formula, which is a simple exponential function exp $(-4.247\ p_t)$, where p_t is the transverse momentum of the (negative) secondary particle, in GeV/c. From this universal function, the following table can be made.

TABLE IV-10

Angular Production Function from the Wang Formula

$$F = \exp\ (-4.247\ p_t)$$

| Particle Momentum, GeV/c | Production Angle, mrad: | | | | |
	0.	0.5	1.	1.5	2.0
150	1.00	.727	.529	.385	.280
200	1.00	.654	.428	.286	.183
240	1.00	.601	.361	.216	.130
320	1.00	.507	.257	.124	.066
400	1.00	.428	.183	.078	.033

The total production can be found by integrating the angular function out to infinity, giving the value 1/4.247 = .236. Thus the area is that contained in a uniform distribution out to a transverse momentum of .236 GeV/c. The corresponding production angle is just this quantity divided by the beam momentum. Thus, at 236 GeV/c the total angular distribution is that contained in a 1 mrad angle, or in π microsteradians. In the vertical direction the acceptance may extend well beyond this angle, so that the entire production is contained; in the horizontal direction, the large proton beam divergence (± 1. mrad) and the small equivalent horizontal acceptance, about ± .25 mrad, cut down the yield. Consequently it seems expedient to change the horizontal proton focusing to get less divergence.

The optimum horizontal focusing was defined as that giving the smallest target size. It was found at a waist of ± .25 mm and a divergence of ± 1.0 mrad, giving a horizontal target width of ± .50 mm. If we depart from the optimum and make the waist ± 0.4 mm, the divergence ± .625 mrad, we get a target width of ± .56 mm, but now the secondary beam angles with the primary proton direction are much reduced, with correspondingly increased yields. There is no sacrifice in resolution either, since the x' width is smaller than the y' in any case.

We thus end up with the following table of calculated π^- yields, IV-11. In this table, we have used the Wang formula; we have converted the yields to be per μsterad·GeV · 0.37×10^{12} interacting protons, where 0.37 is an assumed target efficiency; this yield we call N. In addition we introduce an angular yield

function f_o, which depends only on the secondary beam momentum; it is the effective solid angle available to the secondaries (= .236/E), multiplied by 0.5 to account for the loss of accept- ance in the horizontal direction. The final calculated yield is then Y_f, the product of these factors.

TABLE IV-11

Overall Yield Calculation for Negative Pions

Secondary Particle Momentum GeV/c	f_o, Corrected Angular Yield	Final Yield: No. of π^-/GeV/c.37 x 10^{12} interacting protons.			
		E_p = 400 GeV		E_p = 500 GeV	
		N	Y_f	N	Y_f
160	.735	7.0 E07	5.1 E07	11.0 E07	8.0 E07
240	.49	2.7 E07	1.3 E07	7.6 E07	3.7 E07
320	.37	3.7 E06	1.4 E06	2.4 E07	8.7 E06
400	.30	--	----	4.4 E06	1.2 E06

To convert from pions to hyperons we use the following ratios, which for simplicity we assume independent of alpha[*]; this does not introduce errors as large as a factor of 2. In addition we need decay factors, which depend upon the beam length and the particle momenta.

---

[*]This is somewhat inaccurate for Σ's, where yield is lower below α = 0.8, higher above 0.8. For Ξ it is quite good (the Ξ yield being almost identical with K^-). For Ω there are no data, and the number given is a guess.

TABLE IV-12

Ratio of Hyperon to Pion Yield

(assumed independent of α)

---

1. Σ^-/π^- . = 1.0

2. Ξ^-/π^- . = 0.02

3. Ω^-/π^- . = 2. x 10^{-4}

We now combine all these factors in Table IV-13 to get final yield figures.

TABLE IV-13

Hyperon Yields, taking into Account Production and Decay.

No. of Particles/µster · GeV/c/.37 x 10^{12} Interacting Protons.

Proton Mom. GeV	Hyp. Mom.	Total Beam Length	Pion Yield	Decay Factor			Hyperon Yield		
				Sigma	Xi	Omega	Sigma	Xi	Omega
400	160	21.5 m	5.1E7	.0266	.0278	.0029	1.26E6	2.8E4	29.6
400	240	21.5	1.3E7	.0893	.0917	.0203	1.2E6	2.4E4	53.0
400	240	29.5	1.3E7	.0363	.0377	.0048	4.7E5	1.0E4	12.5
400	320	29.5	1.4E6	.0834	.0856	.0182	1.2E5	2400	5.1
500	400	29.5	1.2E6	.137	.137	.0408	1.6E5	3300	9.8

TABLE IV-14

Ratio of Hyperons to Pions at Beam Exit

Beam Momentum GeV/c	Sigmas per 10^6 pions	Xis per 10^6 pions	Omegas per 10^6 pions
160	4.2E4	860	1.2
240 (21.5 m)	8.1E4	1700	3.5
320	8.5E4	1700	3.7
400	1.2E5	2400	6.7

Note: At 400 GeV/c a momentum acceptance of ± 3% would cover a range of 24 GeV/c; the beam would then have to hold to 4×10^{10} incident protons to keep the total particle flux down to 10^6/sec.

Note on Further Reduction of Muon Background

Since the increase of muon background at low momenta comes from decreasing the field in BM1 and thus failing to deflect the muons adequately, it should be possible to circumvent this difficulty, if necessary, by keeping the field in BM1 at a high value and changing the central plug to give a more curved trajectory. The rest of the beam will have to be retuned, but with more deflection the beam performance should improve. To avoid moving the beam transport, magnets to deflect the incident proton beam could be used to compensate for the change in position of the target.

V.   DESIGN OF THE CERENKOV DETECTOR

The design of the Cerenkov detector takes as its starting point the physics requirements of the experiment. We take it as required to separate and identify hyperons to energies as high as possible - up to 400 GeV/c if possible. To do this implies a focusing type of detector with ring images. Threshold counters in this momentum range are far too long.

A.   Angular Resolution

The angular resolution that determines whether two different ring images are separable is the product of contributions from the beam, and from the Cerenkov detector itself. We have already considered the former; the latter contains several important components.

Counter Contributions

1)   Variation of diameter of ring image with particle momentum. This effect limits the momentum acceptance to a maximum of about ± 3% or less, if sigma-xi separation is to be retained. However, this imposes no great hardship, since in practice we will almost certainly not require so large a momentum bite. However, the slits available for momentum restriction in the beam are not infinitely sharp, and there is always a tail in the momentum pass-band; this is not expected to be troublesome. The sigma-xi separation is always equivalent to a change in momentum of 10%, at any energy or cone angle.

2)   Chromatic dispersion in the gas is always the most serious aberration; it enters through the variation of n in the basic

equation $\cos \theta = 1/n\beta$. It is this quantity that dictates the choice of cone angle. By using the least dispersive gases – helium or neon – and limiting the wavelength region used, the chromatic aberration is kept under control.

3) Multiple scattering in the gas, windows, etc. This is negligible in all practical cases, for the momentum ranges under consideration.

4) Optical imperfections and aberrations. These must be kept sufficiently small not to make significant contributions to image width; there are no difficulties in meeting the requirements.

Table V-1 shows the width of a ring image due to chromatic dispersion in He (for which it is minimal) for the wavelength range 280 – 440 nm, for three different cone angles. For comparison we show the angular separations $\Delta\theta$ of Σ^- and Ξ^- rings as well. The angular spread of the 240 GeV/c beam was given in Table IV-1; it is .06 – .08 mrad, depending on the momentum bite and target size, and decreases only slightly at higher energies.

We have included for comparison the corresponding data for the DISC counter now available at Fermilab; here, of course, the chromatic aberration has been essentially removed, leaving as the major limitation the restricted angular acceptance.

Figure V-1 shows the separation of sigma from xi graphically, for 7 and 11.5 mrad cone angles.

For these small cone angles, the gas pressure in the counter is always low. At 150 GeV/c, 11.5 mrad, it reaches a maximum of about 3 atmospheres (absolute).

Fig. V-1. Shaded Areas indicate spread due to chromatic dispersion.
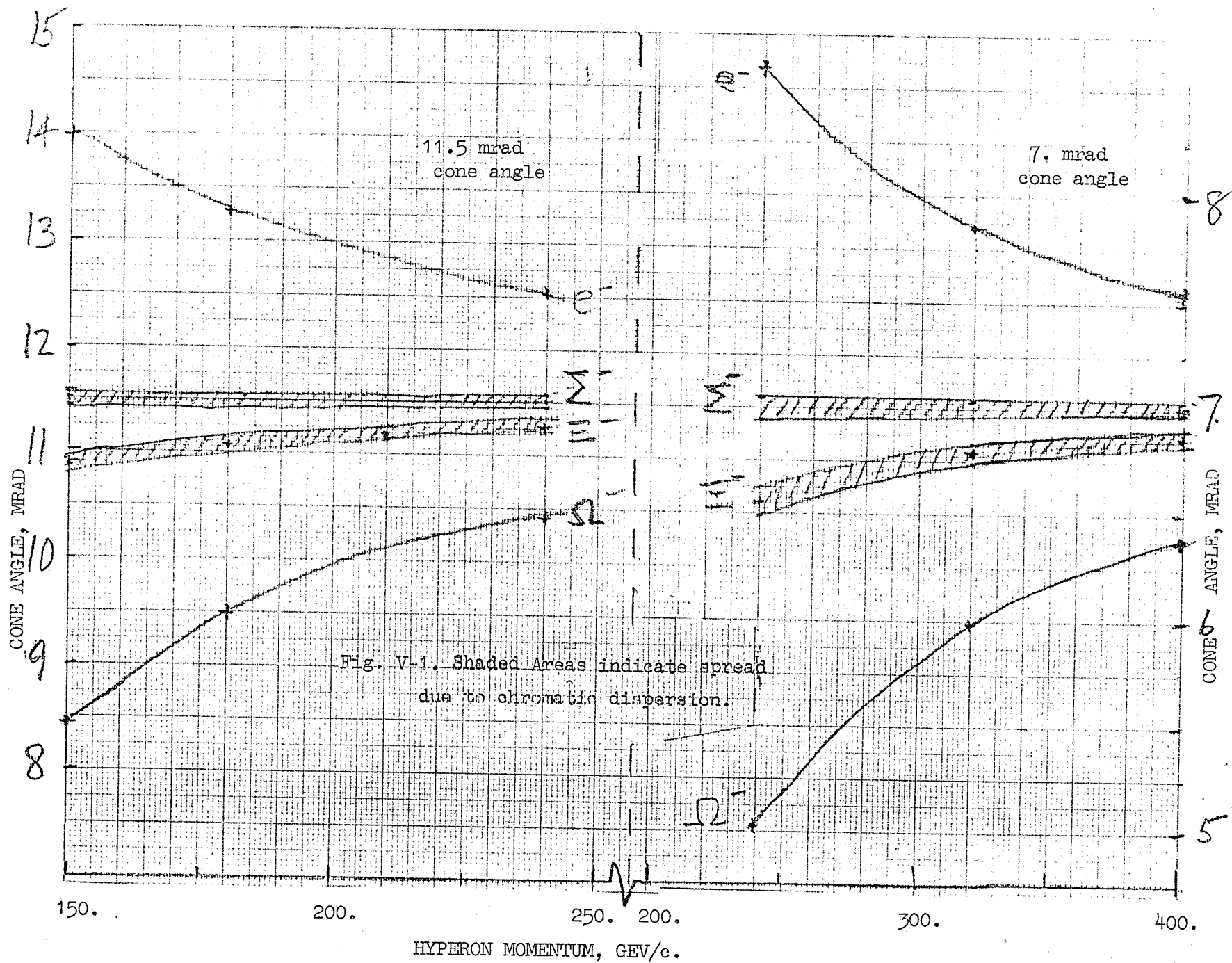
TABLE V-1

Σ^- - Ξ^- Separations $\Delta\theta$, and Chromatic Dispersion CHR, in mrad. Cerenkov Cone Angle, θ:

Hyperon Momentum GeV/c	Beam Spread, mrad*	θ = 7 mrad. $\Delta\theta$ mrad.	CHR mrad.	θ = 11.5 mrad. $\Delta\theta$, mrad.	CHR mrad.	θ = 24.5 mrad. (DISC) $\Delta\theta$, mrad.	CHR mrad.	Angular Acceptance
150	-	-	-	.603	.150	.283	(.015)	.094
180	-	-	-	.420	.139	.175	(.015)	.058
210	-	-	-	.307	.130			
240	.06 - .08	.387	.106	.235	.124	.111	"	.037
320	.05 - .07	.217	.084	-	-	.062	"	.021
360	(.06)	.172	.079	-	-	.049	"	.016
400	(.06)	.140	.077	-	-	.040	"	.013

*Beam spread is due to finite target size: it is given for a 25 cm. long target. See Table IV-1

B. Chromatic Dispersion and How to Live with It

There are two ways to handle the chromatic dispersion problem. You can suffer its slings and arrows; or, you can take arms against it, and by opposing, end it. (The third alternative, to vacillate, Hamlet-like, we reject.).

Cerenkov detectors in which the chromatic dispersion is corrected are known by the generic name of DISC. They are usually characterized by extremely high resolution and correspondingly small angular acceptance; the last entry in Table V-1 shows a typical instrument of this type. These features of the DISC are not inherent characteristics; they are consequences of a decision to use large cone angles, which keeps the counter shorter and smaller in diameter, and thus less expensive. The latter point is of great importance, since the achromatization of the DISC, extending as it must into the UV, is very expensive.

The alternative to the DISC is to use a conventional Cerenkov focusing counter, with a considerably smaller cone angle, which improves the mass resolution. One must then accept the greater length, additional hyperon decay, and decreased light output this choice entails. If the beam optics are not able to supply a hyperon beam within the phase space acceptance of the DISC counter, one must either accept the corresponding loss of beam or switch to the conventional detector.

In considering whether to use a DISC or a conventional counter, we have been influenced by the fact that there exists in the Laboratory a half-completed DISC which might perhaps be

made available to this beam; it is the one whose characteristics are described in Table V-1. Figure V-2 shows a sketch of it. Considerations of both cost and procurement time probably rule out of consideration any other DISC design, and thus we confine ourselves to this one example.

C. Performance Requirements and how to Achieve Them

An ideal Cerenkov detector would detect, identify, and tag all particles traversing it, and also measure their direction and momentum. Let us see how closely such an ideal may be approached.

First, we note that the DISC does not attempt this task. It has a single circular slit, albeit of very high resolution, and detects only those particles whose Cerenkov light passes through the slit. There are no anticoincidence circuits; it rejects unwanted particles by brute force. To achieve a reasonable degree of signal purity, at least sixfold, preferably eightfold coincidences are required for the accepted particles; thus the minimum number of photons in the ring image must be in the range 30 to 40. The resolution is excellent, and the specifications on allowable angular divergence of the beam correspondingly stringent. From Table V-1 we note that at 240 GeV/c the 24.5 mrad DISC we are considering will have an angular acceptance of .037 mrad, with correspondingly less at higher momenta. In contrast, the angular divergence of the beam is determined in practice by target size; and for the 25 cm. long target we would like to use, the beam spread is as large as .06 to .08 mrad.

DIAPHRAGM   CHROMATIC CORRECTOR   COMA CORRECTOR   MIRROR
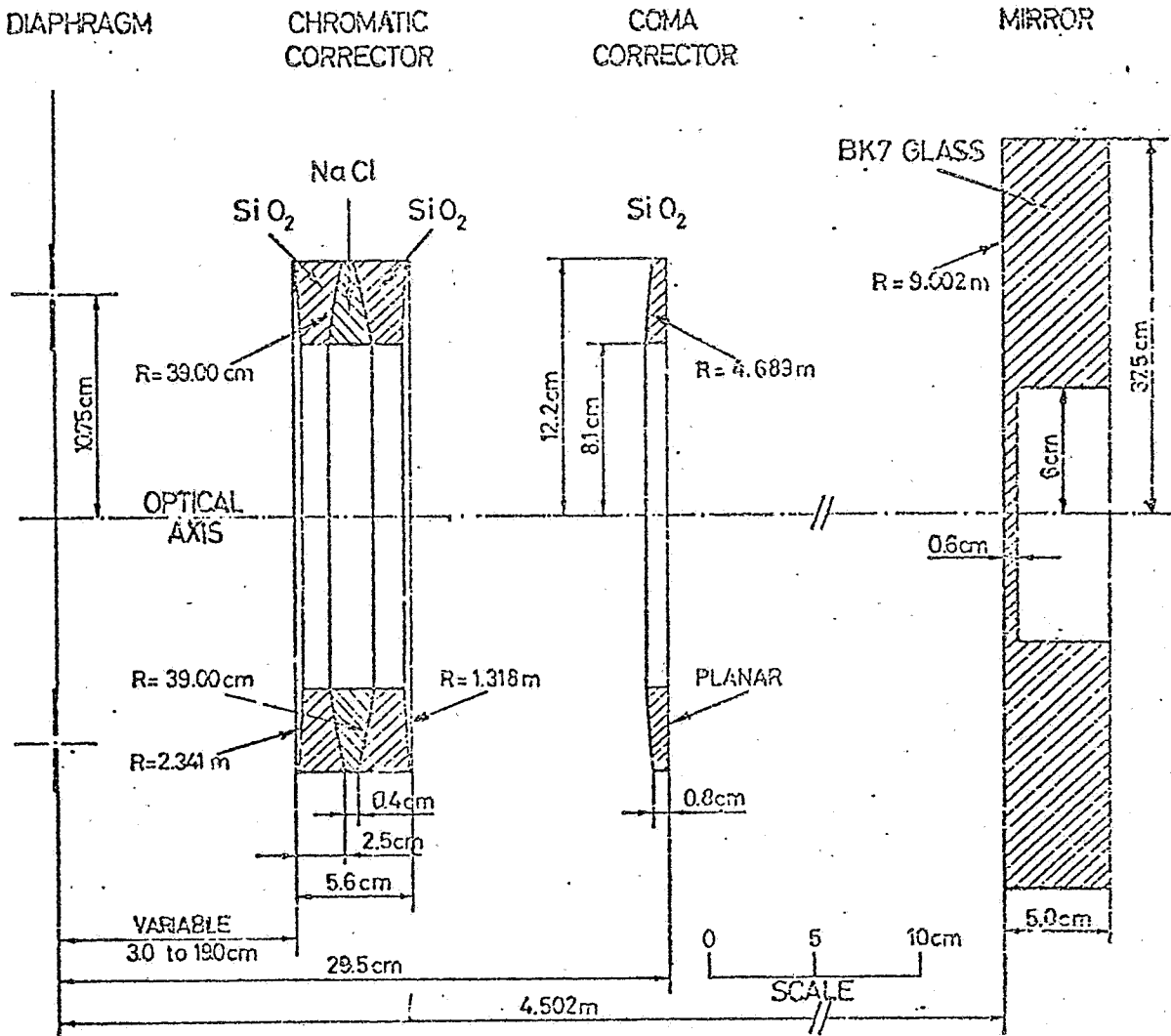
SPECIFICATIONS OF THE OPTICS FOR THE CERN DISC

CERENKOV COUNTER (JULY 1971)

Fig. V-2. Internal construction of the 24.5 mrad CERN DISC counter.

Corresponding losses in detection efficiency will be inescapable.

The alternative, the conventional ring-focusing counter, does not rely on high resolution alone to distinguish particles. It accepts the chromatic aberration in the gas radiator, and circumvents it by taking advantage of the fact that the chromatic aberration is a decreasing fraction of the angular separation of any two particles of different masses, as the cone angle is decreased.

Let us assume that the Cerenkov detector can be so constructed that its cone angle and length are variable, to allow the resolution and length to be adjusted to fit the momentum in use. To obtain sufficient light, we take a radiator length of 14 meters for a cone angle of 7 mrad. We then reduce to 6 m for an 11.5 mrad cone angle; in the latter case the total light is slightly more. We add arbitrarily, 1 meter to each length to obtain overall lengths of 15 and 7 meters.

The greater length incidental to smaller cone angles increases the decay likelihood; but up to 400 GeV/c, the overall counter length increases more slowly than the relativistic dilation of the decay length, so we can afford it. The angular separation of the particles increases as the cone angle is decreased, allowing greater beam divergence, target size, and easing alignment and constructional tolerances. Furthermore, more sophisticated means of separating particles of different masses than a single fixed slit can be used, since the optics are now simpler. The method generally used to deal with more than one ring image is usually some form of image dissection.

Image Dissection

Image dissection is the most general method available for the extraction of information from complex optical images. The prototype is the television raster scan, in which the image is dissected into a series of adjacent lines, scanned in turn to make a complete frame. For this purpose storage tubes like the vidicon are preferable, since they integrate and store an image which is then read out by a scanning electron beam. This technique is available for Cerenkov images, although not in quite so simple a form; the signal-to-noise ratio of the vidicon is inadequate for signals from single photons. The deficiency can be remedied by preceding the vidicon with one or two stages of image-intensifier. This technique for storing and dissecting ring images using image intensifiers and storage phosphors was first suggested by one of us in 1960[14], when the available image intensifiers were not really satisfactory. Present-day "second generation" intensifiers are, and one technique proposed for this experiment involves the use of such an image-dissecting system, using one or more channel electron multiplier array (CEMA) tube, with a segmented anode for image dissection[15]. In the achromatic beam the segmented anode is greatly simplified, since it becomes merely a raster in polar coordinates.

The advantage of the image dissection technique can best be understood if one imagines a Cerenkov detector whose output is a large screen on which flash the successive ring images of different particles. For each particle one can determine the

location of the center of the ring and the radius. This is all the information available; it gives the particle direction and velocity. If the particle momentum is known this determines the mass. It is the mechanization of this process that offers difficulties.

Returning to the conventional focusing Cerenkov detector, we ask: how can these results be obtained using only photomultiplier detectors, until suitable image-intensifier tubes become available? The answer clearly lies in the provision of an array of slits and photomultiplier tubes, preferably not too complicated nor too expensive.

If we now compare the requirements for the dispersive beam and the achromatic beam, the advantage of the latter becomes apparent. A method for image-dissection to identify all the hyperons in a dispersive beam was described by one of us in 1972[5]. It used a system of multiple slits, but replaced slit segments by mirror segments to add another element of freedom in the placement of the photomultiplier tubes. Figure V-3 shows the ring images for three different particles in a dispersive beam, at three different momenta. The considerable overlap would be much reduced by narrowing the momentum range; but on the other hand, increasing the momentum to 400 GeV/c would again make the separation more difficult as the velocity differences decrease. Furthermore, a completely new slit segmentation layout would be required for each momentum, since the relative radii change with momentum. Figure V-4 shows how the image dissection is accomplished. A similar
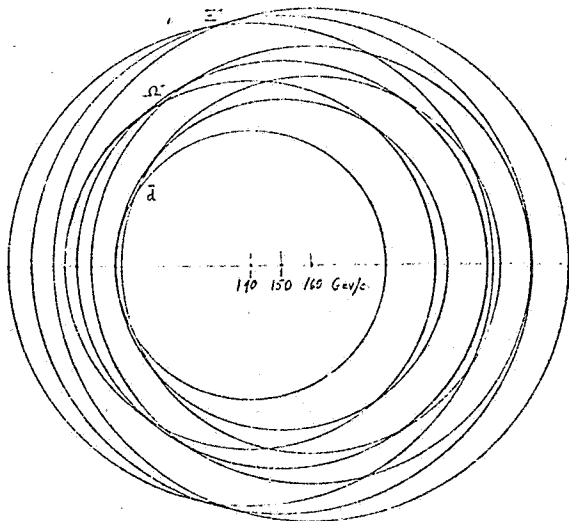
The Cherenkov circles for Ξ^-, Ω^-, and $\bar{d}$ at 140, 150 and 160 GeV/c, showing the approximate focusing for each kind of particle, the considerable overlapping at the right hand side, and the possibility of mass determination even without using the focus. Centers for each momentum are shown. $n = 1.00011$.

Fig V-3. Ring images in the dispersive

hyperon beam.
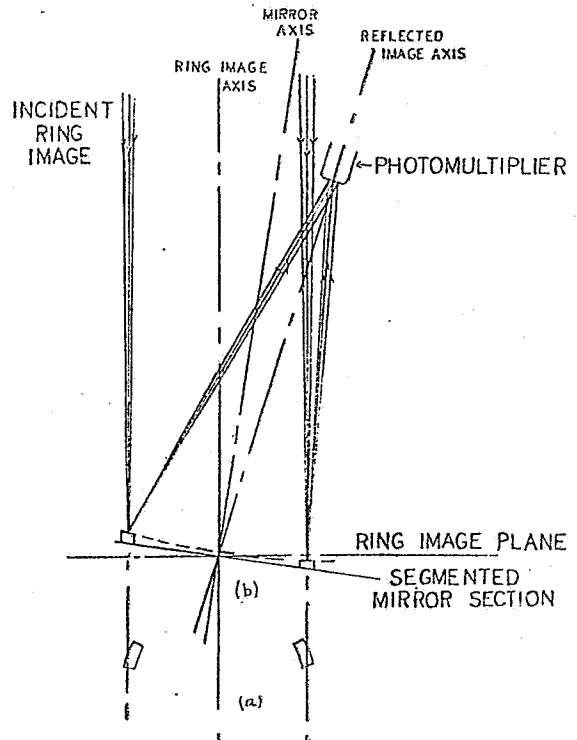
The use of concave mirror segments in the Cherenkov ring image plane to separate and collect the light falling on a specified symmetrical pair of segments. (a) A pair of circular segments in the image plane, seen from the direction of the incident light. (b) A slight tilt of the axis of the segmented mirror results in the collection of the light in a phototube out of the way of the incident light. Note that the focus of the incident Cherenkov light must be at the mirror plane in order to use the mirror segments as velocity slits.

Fig. V-4. Image dissection with

segmented mirrors.

design for CEMA tube with segmented anode structure has been proposed by J. Sandweiss[15].

In contrast to Fig. V-3, now consider the achromatic beam ring images, which are merely a set of concentric circles, all the centers now being coincident. In principle, the slits can now be simple circular mirror segments. The design simplification is very great, and the performance improvement should be dramatic. Exactly similar arguments apply to the segmented-anode CEMA tube, which is the analogue of the mirror system just discussed. In this case, the rearrangement of segments required by a momentum change might be logical rather than hardware, if the anode segmentation is sufficiently fine-grained. In both cases, the image dissection is reduced by achromatization to the trivial case of a raster in polar coordinates. Figure IV-5 shows the components of a CEMA detector.

There is one point of conflict between the CEMA type image intensifier detector and the slit or mirror-imaging dissecting system using phototubes; this is the size of image required. CEMA tubes are presently limited, by cost considerations, to a maximum diameter of 40 mm. One can use several tubes, but clearly image diameters should not be much over 80 or 90 mm. On the other hand, the optics and mechanics for slit and mirror segment systems are easier for larger sizes. We consider below some possible solutions and compromises of this problem.

The image-dissection system can of course be simplified and varied. The simplest form is a slit for the accepted particle,

DUAL HIGH-GAIN MICROCHANNEL PLATE

INCIDENT
RING IMAGE

SEGMENTED ANODE

PHOTOCATHODE
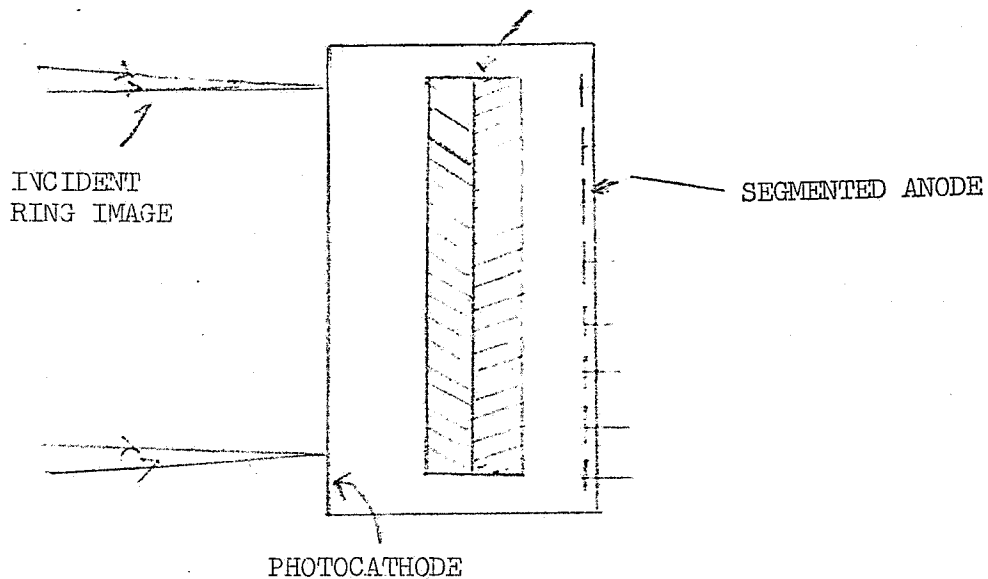
Fig. V-5a. CEMA image intensifier tube with segmented anode. Proximity
focusing is used both at the cathode and anode.
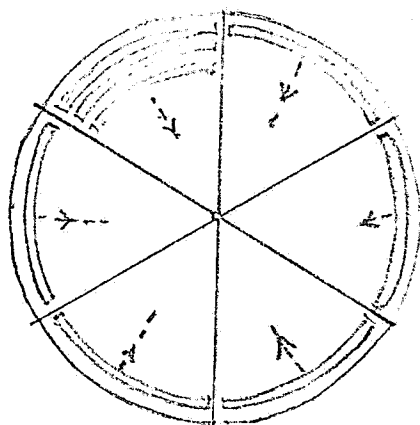
Fig. V-5b. Segmented anode, with concentric 60° segments. Only a
few segments have been drawn in.

and mirrors for the rejected ones, in anticoincidence; this form
has been used by Ozaki et al.[16] Versions that accept and indi-
vidually tag all the hyperons can readily be envisaged. Experi-
ence with a model of a sigmented mirror detector indicates that
the only problem is the mechanical mounting of the mirror seg-
ments and that it is soluble, most readily when the segments are
not too small.

TABLE V-2

Slit Parameters for Photomultiplier Detector System,

with a 5.0 m Focal Length Mirror. $\Delta\theta$ is

the Σ^- - Ξ^- Angular Separation

A. 7.0 mrad cone angle (for sigmas): image radius 35 mm.

P GeV/c	$\Delta\theta$ mrad.	Sigma-Xi sep, mm	Slit Width, mm	Cone angle, mrad for β = 1	Max. image radius, mm
240	.387	1.935	0.75	8.6	43.0
320	.217	1.085	.62	7.82	39.1
400	.140	0.70	0.55	7.61	38.05

B. 11.5 mrad cone angle: image radius 57.5 mm.

150	.603	3.0	1.00	14.0	70.0
180	.420	2.10	.85	13.3	66.5
210	.307	1.54	.80	12.8	64.0
240	.235	1.18	.75	12.5	62.5

D. Mirror Optics

The mirror optics required for the Cerenkov detectors depends not only on the length and cone angle of the Cerenkov radiator, but also on the image size required by the detector. Three different detector arrangements can readily be envisaged: one in which only conventional photomultipliers are used, one using a single 40 mm CEMA image intensifier tube, and one using several such tubes in order to obtain larger images and better resolution.

The optical quality of the mirrors is not as high as that needed for astronomy or photographic purposes, where the diffraction limit is in the region of 0.002 mrad. A mirror whose resolution is ten times worse than that would still be perfectly acceptable. Aberrations up to .02 mrad can likewise be tolerated. The size of mirror needed is given by the longest radiator, 14 m, and the largest cone angle which is 8.6 mrad. This gives a mirror aperture requirement of 120 mm radius; a 10" diameter mirror is indicated. The 11.5 mrad detector, with a much shorter (6m) radiator does not need the full diameter.

For photomultiplier detectors, with several photomultipliers - say 4 - desired per particle in order to obtain high-order coincidences for background reduction, a large image format is desirable; this makes the slits easier to make, and allows them to be closer together. Thus, a 5 meter focal length would give a maximum image diameter, with the 8.6 mrad cone mentioned above, of 86 mm. The image would be larger with the 11.5 mrad system, where a maximum cone angle of 14. mrad yields an image diameter of 140 mm.

Table V-2 shows the separations and slit widths needed for this system, for the photomultiplier detector array and a 5.0 m focal length mirror. For the arrangement using four 40 mm CEMA tubes, each one occupying a quadrant of the image (whether together or separated by dissecting the primary mirror, as suggested by Sandweiss[15]), the range of image radii that can be accommodated is from about 13 to 43 mm. From Table V-2, this would be entirely satisfactory with a 5 m focal length mirror for the 7 mrad cone angle, but not for the 11.5 mrad. For that angle, to keep the maximum radius within range, the focal length should not exceed 3.0 m. That mirror, however, needs a diameter of only 158 mm.

The case of the single 40 mm CEMA tube is a rather special one; it requires the best resolution in the detector because of its small area, and thus the shortest focal length mirrors. Sandweiss has estimated a focal length of about 1.25 m for this detector, which would give a maximum 35 mm diameter image at 14 mrad. It is interesting to contemplate the possibility of using a Schwarzschild optical system, as suggested by Sandweiss, with a 3 m focal length first mirror, and a second mirror to give a final focal length near 1.25 mm. To use the system with the 4-tube CEMA array, the second mirror could be replaced by a plane reflector, giving a 3 m focal length. The mirrors would have to be so figured as to be usable either singly or together.

To summarize, the general design of the focusing Cerenkov detector that emerges from our considerations requires variation of the Σ^- cone angle from 7 to 11.5 mrad, to cover the momentum range 150 - 400 GeV/c. The length will change correspondingly from 7 to 15 meters. Distinguishing sigmas from xis should be possible for all momenta up to somewhere between 320 and 400 GeV/c. Simultaneous tagging of omega (and/or $\bar{p}$) with either sigma or xi appears feasible.

Such a detector appears preferable to the DISC on the grounds of flexibility, ability to utilize the proton beam efficiently (with minimum muon background) at all energies, multiple tagging and anticoincidence possibilities, and cost.

Figure V-6 shows how the beam and Cerenkov detector system envisaged would appear.

BM1   Q1V   BM2   Q2H   Cerenkov Detector
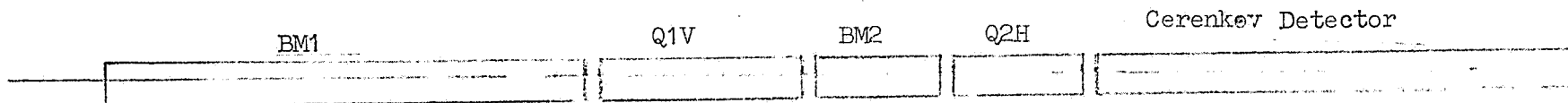
a) 150 – 240 Gev/c. Overall length 21.5 m. Cerenkov cone angle 11.5 mrad.
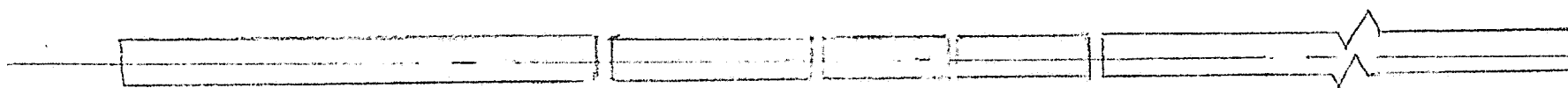
b) 240 – 400 Gev/c. Overall length 29.5 m. Cerenkov Cone angle 7. mrad.

0   5   10   15   20

Scale, meters

Fig. V-6. Beam layout for two different energy regions, using variable-length Cerenkov detector.

VI. SUMMARY

1. An achromatic hyperon beam has been designed for the proton central area, to cover the momentum range 150- 400 GeV/c, with incident protons up to 500 GeV/c. It requires four superconducting magnets of special design: two dipoles and two quadrupoles. Cerenkov detectors capable of accepting all particles in the transmitted momentum interval (up to several percent) are described.

The performance of the transport and Cerenkov detector allow separation and identification of all hyperons at all energies in this range (with the possible exception of sigma-xi separation near the top end of the range.) The required proton beam will not exceed 10^{12} protons per pulse, and may well be less. The incident proton beam must have as a high a quality (small acceptance) as possible; it is the limiting factor in the obtainable angular and momentum resolution.

2. Calculations on muon background indicate it to be adequately low, except possibly at the lowest secondary beam momenta. If it does become a problem, steps to ameliorate it are feasible.

3. Considerations on the types of Cerenkov detector possible for use with an achromatic beam lead us to recommend a conventional focusing detector, so designed as to allow:

a) A change of cone angle and length between the 7 mrad, 15 meters; and 11.5 mrad, 7. meters.

b) An interchangeable optical system permitting the use of either a conventional system with photomultiplier sensors, or a CEMA detector with a segmented anode system.

We have not yet concerned ourselves with some important problems that still require attention. These include steering and focusing for the incident proton beam, and the details of the collimator in BM1.

We conclude that the achromatic beam concept is a valid and important advance; that it makes possible simple, efficient and powerful Cerenkov detectors, and the extension of the useful energy range to above 300 GeV/c; and that the beam may be designed to render the muon backround innocuous. Table VI-1 summarizes the properties of dispersive and achromatic beams and the corresponding Cerenkov detectors.

TABLE VI-1

Comparison of Dispersive and Achromatic Beam

Properties and Their Implications for Detectors

Characteristic	Dispersive	Achromatic
Momentum Range $\delta p/p$	Up to $\pm$ 6 - 10%	Up to $\pm$ 3%
Horizontal Angular Dispersion (150 GeV/c)	0.22 mr/1% $\delta p/p$	.02 mr. for $\pm$ 3% $\delta p/p$
Vertical Angular Dispersion (150 GeV/c)	$\pm$ .06 mr ($\pm$ 6.6% $\delta p/p$)	$\pm$ .03 mr. for $\pm$ 3% $\delta p/p$
Method of Momentum Determination	Measurement of horizontal direction at exit.	Horizontal location at two points along beam.
Accuracy of Momentum Determination	Limited (in both cases) by target size. For small targets (< .2 mm) achromatic beam may be limited by location accuracy (70 µ) at about $\pm$ 0.3%.	
Sigma-Xi separation:	Fraction of beam accepted by a Cerenkov detector with .06 mr vertical aperture, at 240 GeV/c:	
	Momentum acceptance 0.3%	Momentum acc. $\pm$ 3%
	Vertical acceptance 50%	Vertical acc. 100%
Type of detector needed for detection efficiency above 10%	Special image-dissecting type; image-dissecting scheme changes with particle momentum.	Conventional. (100% efficient)
Beam length at 240 GeV/c, not including Cerenkov detector.	10.7 m	12.6 m.
Maximum momentum at which sigma-xi separation is feasible	200-240 GeV/c?	320-400 GeV/c

REFERENCES

[1] Proposal, E97.

[2] Proposal, P-353.

[3] Fermilab Internal Report E97-1, by A. Roberts.

[4] Fermilab Internal Report, A. Roberts, M. Atac, and R. Stefanski, May 7, 1970; R. Stefanski, FN-239, December 10, 1971.

[5] A. Roberts, Nucl. Instr. and Meth. 99, 589 (1972).

[6] V. Hungerbuehler et al., NAL Pub. 73/16 Exp; Phys. Rev. Lett. 30, 1234 (1973).

[7] R. March and R. McCracken, TM-330, Nov. 1971.

[8] R. Adair, private communication.

[9] C. M. Ankenbrandt, Internal memo, February 27, 1975.

[10] P. Sanger, private communication.

[11] C. T. Murphy, private communication.

[12] CERN/74-32, SPSC/P2 Add. 1, Addendum to Charged Hyperon Proposal, R. Baldi et al., March 1974.

[13] C. L. Wang, Phys. Rev. D7, 2609 (1973); ibid D10, 3876 (1974).

[14] A. Roberts, Nucl. Instr. and Meth. 9, 55 (1960).

[15] Fermilab, E-97, YJS-1, June 1975: Cerenkov Counters for E-97, P-353, J. Sandweiss.

[16] S. Ozaki, J. J. Russell, E. J. Sacharidis and J. T. Reed, Nucl. Inst. Meth. 35, 301 (1965).

Cerenkov Counters for E-97, P(E)-353, A Proposal

J. Sandweiss, Yale University

I. General

The purpose of this document is two fold:

a) to present a brief description of a Channel Electron Multiplier Array (CEMA) type of Cerenkov counter, pointing out its unique capabilities for these experiments. A more complete and detailed paper on the CEMA counter is in preparation in collaboration with Stan Ecklund, Dick Majka and Satish Dhawan.

b) to present the design of a "Phase I" counter which could be used with CEMA tubes as in (a) but which could also be used with ordinary photomultipliers as a viable alternative to the DISC. Indeed, we shall argue that in addition to the advantage of being compatible with the CEMA tubes, the Phase I counter will have certain other advantages relative to a DISC counter of the E-69 design.

We note that the Phase I design is more than preliminary but less than final for the following reasons:

i) a small amount of "fine tuning" remains to be done on the design presented,

ii) the design should be studied to see if conic sections of revolution (conicoids) would be sufficiently close approximations to the aspheric surfaces. Such conicoids would be less expensive to polish and test.

iii) clearly it would be desirable for the calculations to be independently checked and/or other comments and suggestions of E-97, P(E)-353 physicists to be incorporated.

II.   The CEMA Counter

In the focal plane of the optical system which, as we shall see in section IV, can be made so that aberrations are negligible, the Cerenkov light from a given particle will fill an annular ring of average radius $\overline{R}$ and width ΔR where:

$$\overline{R} = f\ \overline{\theta}_c \tag{1}$$

$$\Delta R = f\ \Delta\theta_c \tag{2}$$

In (1) and (2) f is the optical focal length, $\overline{\theta}_c$ is the average Cerenkov angle and $\Delta\theta_c$ is the spread of Cerenkov angles due to the variation of index of refraction of the radiator gas with optical wavelength.

Although we shall return to the choice of system focal length later in this section, for the following analysis it is convenient to measure radii and radial widths directly in terms of angles (i.e. equivalent to choosing units of length so that f=1).

It is convenient to describe the position of a point on an arbitrary ring of light in terms of polar coordinates referred to a system centerpoint as illustrated below.
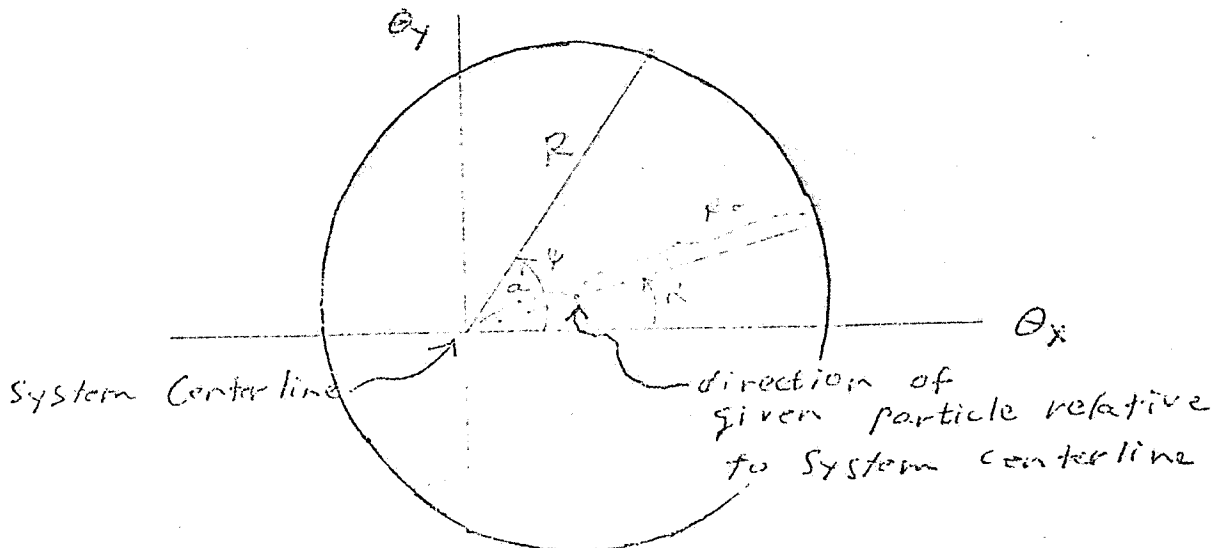
Neglecting terms of order $(a/R_o)^2$ or higher, i.e. to an accuracy of ~1% we can write:

$$R = R_o + a \cos(\psi - \alpha) \tag{3}$$

We suppose that the CEMA counter would be used with a beam design which is made parallel (to ±.1 mr) in the vertical direction but could be as divergent as ±1.5 mr in the horizontal direction.[1] A typical set of curves for P, Σ, Ξ, Ω at 180 GeV/c are shown in figure 1. As illustrated in the figure the most difficult separation is between Σ and Ξ.

At any given beam momentum we must operate the counter pressure (i.e. Cerenkov angle) so that the particles we wish to distinguish are separated by a sufficient number of $\Delta\theta_c$'s, or colloquially, a sufficient number of dispersion widths. In this type of counter all of the observed $\Delta\theta_c$ will be due to dispersion and furthermore the CEMA tubes with the proposed optics will cover a very large band of angles simultaneously and thus will permit very powerful anticoincidence conditions on background particles, delta rays, etc. For these reasons it seems reasonable to choose as a nominal design choice particle separation by 2.2 dispersion widths.

Table I shows the Cerenkov angles and separations for 180 GeV/c and Tables II, and III show them for two modes of operation at 100 GeV/c. We anticipate that the Table III mode will be favored in that it gives substantially more light than the Table II mode.
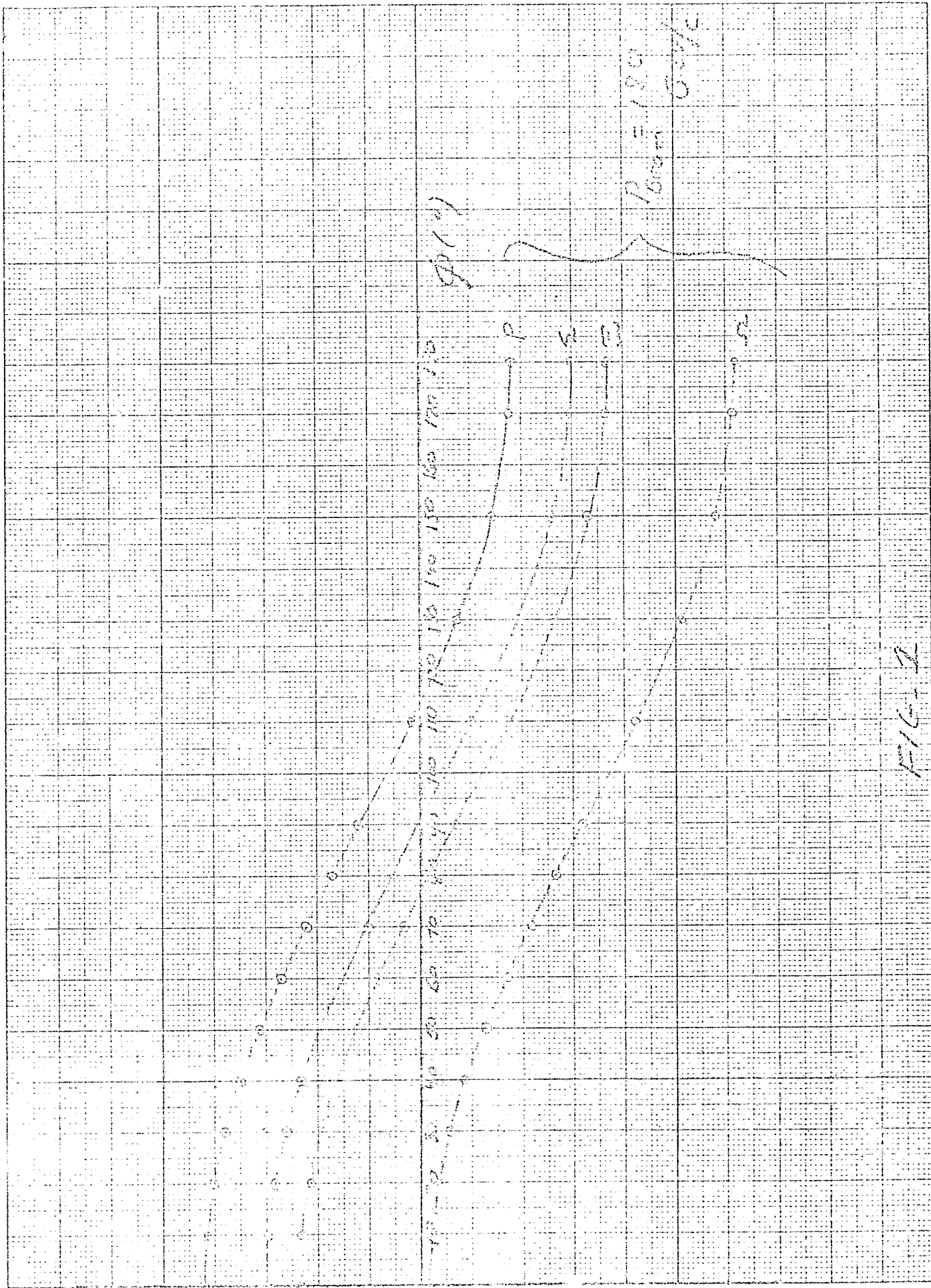
FIG. 2

Table I

Cerenkov Angles and Dispersion Widths at 180 GeV/c

Particle	$\overline{\theta}_c$ (mr)	$\Delta\theta_c$ (mr)	$\left[\overline{\theta}_c(i) - \overline{\theta}_c(i+1)\right]/\Delta\theta_c$
π	15.48		
P	14.597		
Σ	14.000	.16	2.175
Ξ	13.652		
Ω	12.408		

Table II

Cerenkov Angles and Dispersion Widths at 100 GeV/c, Mode I

Particle	$\overline{\theta}_c$ (mr)	$\Delta\theta_c$ (mr)	$\left[\overline{\theta}_c(i) - \overline{\theta}_c(i+1)\right]/\Delta\theta_c$
π	18.369		
P	15.853		
Σ	14.000	22	5.19
Ξ	12.837		
Ω	7.730		

Table III

Cerenkov Angles and Dispersion Widths at 100 GeV/c, Mode II

Particle	$\overline{\theta}_c$ (mr)	$\Delta \theta_c$ (mr)	$\left[\overline{\theta}_c(i) - \overline{\theta}_c(i+1) \right] / \Delta \theta_c$
π	21.76		
P	19.687		
Σ	18.227	.206	4.26
Ξ	17.350		
Ω	14.000		

Table IV shows the operating angles and separations for a possible operation at 250 GeV/c beam momentum.

Table IV

Cerenkov Angles and Dispersion Widths at 250 GeV/c

Particle	$\overline{\theta}_c$ (mr)	$\Delta \theta_c$	$\left[\overline{\theta}_c(i) - \overline{\theta}_c(i+1) \right] / \Delta \theta_c$
π	10.180		
P	9.479		
Σ	9.000	.106	2.66
Ξ	8.718		
Ω	7.694		

We have calculated the dispersion widths $\Delta \theta_c$ via:

$$\Delta \theta_c = \frac{\theta}{2\nu} + \frac{(1-\theta)}{\nu \theta} \qquad (4)$$

where ν is the Abbe number as given by Litt and Meunier[2]
($\nu = 54.5$ for He gas).   Of course all of the analysis uses the
basic Cerenkov equation

$$\cos \theta_c = \frac{1}{\beta n} \qquad (5)$$

where β in (4) and (5) is the particle velocity divided by the
velocity of light and n is the index of the refraction of the gas.

The basic operating scheme of the CEMA counter is illustrated
in the sketch below.

High Resolution MWPC   *High Resolution MWPC*
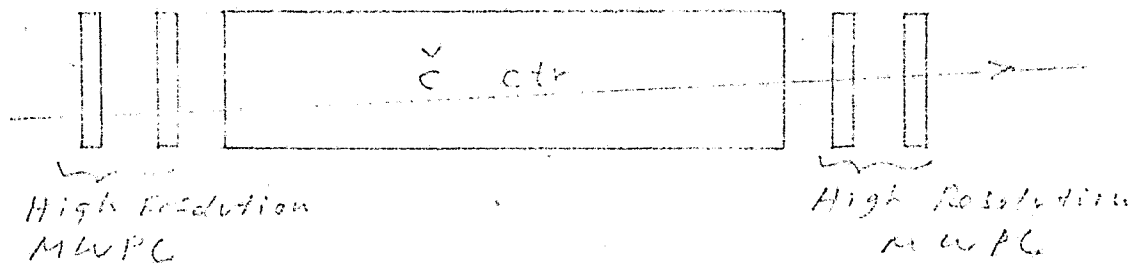
The proportional chambers provide fast on line determination
of the particle direction which is input to a microprocessor. The
microprocessor then decides (via a table look up) which set of
anode segments will intercept (multiplied) photoelectrons from,
say the annulus of θ, Cerenkov light. The design is such that
five non overlapping sets of anode segments correspond to light

from the five particle types π, P, Σ, Ξ, Ω. The amplified discriminated outputs from segments of a given set are placed in a logical OR and compared with a desired discriminator level (sets the required coincidence multiplicity). The resulting signals thus say "yes" or "no" to the five questions π?, P?, Σ?, Ξ?, Ω? and may be combined with other fast logic signals to determine the ultimate fate of the event. On all accepted events, the addresses of all struck segments would be sent to the main computer and recorded. Appendix I gives a "first cut" layout with some performance and cost estimates which has been prepared by Satish Dhawan. We note that the quantum efficiency of a CEMA tube is comparable to that of normal photomultipliers, indeed for Cerenkov light the CEMA might have a better overall quantum efficiency because the photoelectron collection efficiency does not decrease at the high frequency end of the optical spectrum. The individual segment discriminators will be set at the single photo-electron level and the detection efficiency of the counter can be calculated in the usual way from the expected number of photo-electrons and the required coincidence structure.

The angular range over which the counter will accept and utilize Cerenkov light is an important input factor to the design. The maximum angle is set by choosing the lowest momentum at which the full range from π to Ω is to be simultaneously detected. Because of the relatively short lifetime of the Ω^- a choice of 100 GeV/c for this momentum seems conservative. From Table III

we see that at P = 100 GeV/c, θ_c = 21.76 mr, adding 1.5 mr for beam spread gives 23.26 mr which we "round off" to θ_{max} = 23.5 mr.

As we shall see, the smallest angle is really set by the hole in the mirror for the beam to go through. We have somewhat arbitrarily chosen a 1.7 cm diameter hole. As will be shown later, this means that the beam can be ~1.5 cm wide horizontally and depending on its exact shape substantially larger vertically. This corresponds to a θ_{min} = 8.5 mr if light is to be collected over all but the "last" meter (closest to the mirror) of gas radiator length. This choice is very generous for operation at 180 GeV/c and with a restricted beam spread would allow $\Sigma - \Xi$ separation at 250 GeV/c as indicated in Table IV. We vote that if the length of radiator is increased (without change of the optical system) light from still smaller angles will be collected and focused without significant aberration. Finally, if deemed cost effective one can replace the missing mirror segment (beam hole) with a suitably ground and polished aluminized Berylium mirror which would be thin enough to let the beam pass through.

So far we have discussed only the range of polar angles (with respect to the beam direction) which will be detected. We consider now the required azimuthal range. This is initimately connected to the design of the CEMA anode segments. We propose to make the anode segments as circular annular strips grouped into six azimuthal sectors. Three of these sectors would be focussed on one CEMA and three on a second CEMA. This is

illustrated schematically below.

"Left" Tube   "Right" Tube
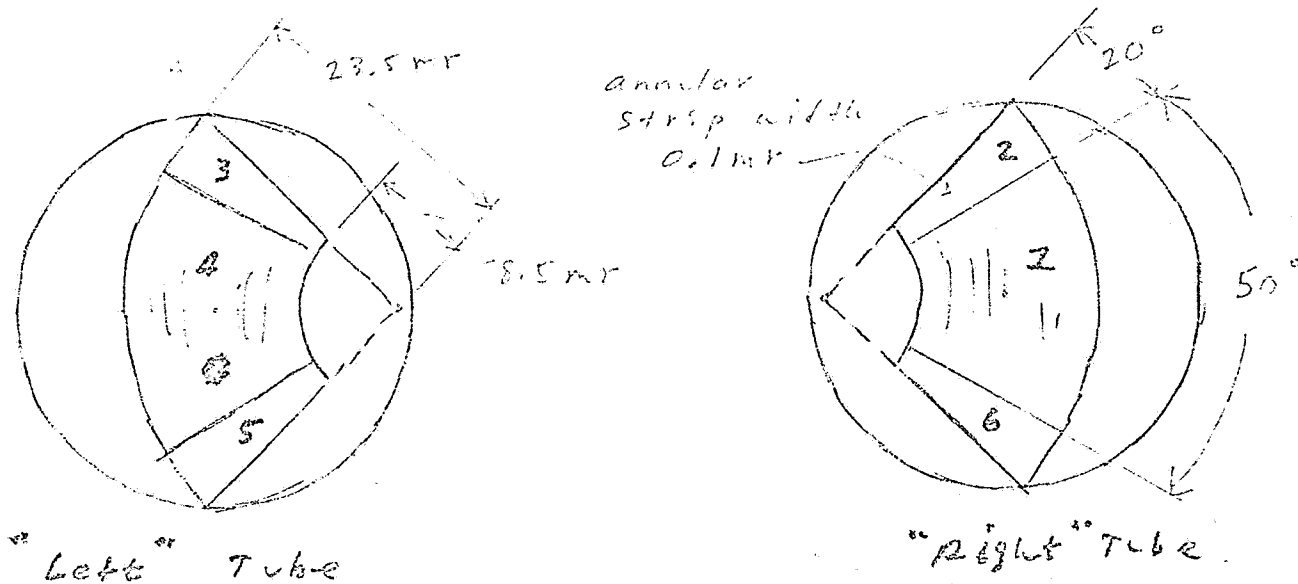
The particular parameters illustrated will be close to but
not precisely the final design. Figure 2 shows the case of
$\Sigma - \Xi$ separation at 180 GeV/c and ±1 mr beam spread. For
economy of drawing, only half of one tube is shown but the
pattern is symmetrical about $\phi = 0^\circ$. Thus A of Figure 2 corresponds
to half of say sector 1 in the sketch and B to sector 2. A
sector C ($-45^\circ < \phi < -25^\circ$) would correspond to sector 6 in the
sketch. For the case shown in figure 2, the segments shown in heavy
outline would belong to the Ξ set. As a concrete illustration we
list, for the case of figure 2, the relevant sectors belonging
to the Ξ and Σ sets (recall definition of C above).

$$\Sigma \quad \{A8, \ A7, \ A6, \ B7, \ B6, \ B5, \ C7, \ C6, \ C5\}$$

+ "corresponding" segments in 2nd tube

$$\Xi \quad \{A4, \ A3, \ B3, \ B2, \ B1, \ C3, \ C2, \ C1\}$$

+ "corresponding" segments in 2nd tube

As can be seen from figure 2, the Σ and Ξ sets are clearly differentiated. We recall also that since all struck segments are recorded, the resulting Ξ sample, for example, can be "cleaned up" by considering the Σ segments as a veto counter. Also since the counter will probably be operated with a requirment that at least one of the designated segments in each tube fires, the effect of a small overlap of Σ light into a Ξ segment (e.g. segment B3 in Figure 2) is very much reduced (it enters squared into the relevant detection efficiency). Figure 2 and the preceding discussion indicate that the design shown will work very satisfactorily at 180 GeV/c and ±1 mr beam divergence. Operation at 180 GeV/c and ±1.5 mr beam divergence may require some restriction on the accepted range of ϕ. We note that the image focal plane is outside the pressure vessel (in fact at the photocathode surface) so that an azimuthal calimator can be placed between the pressure window and the CEMA to simply effect any required ϕ restriction.

Of course it may well be that since the invention of the achromatic beam design,[3] the hyperon beam will not be operated
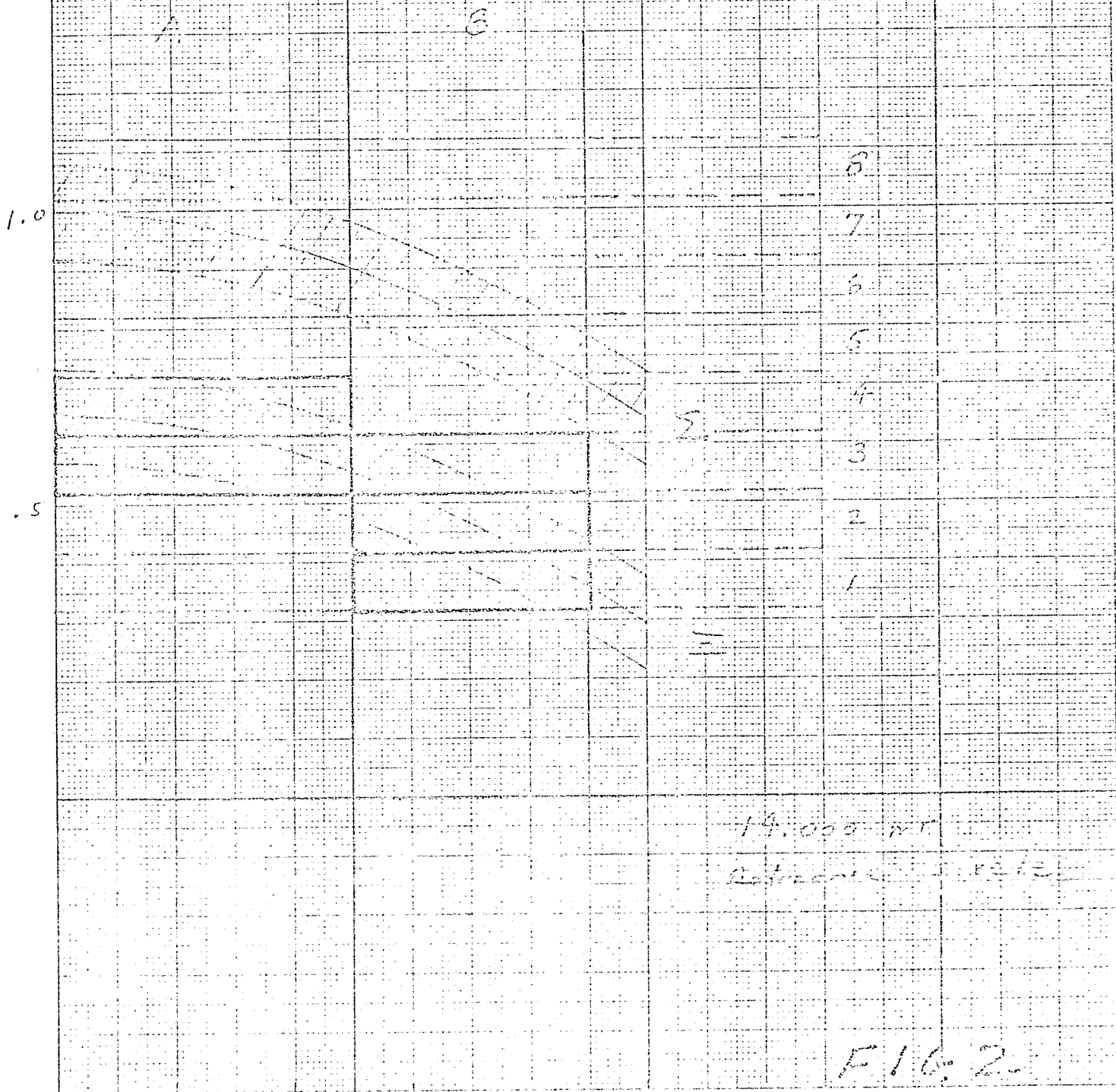
Fig. 2

at divergences greater than ±1 mr in the horizontal plane. As will be discussed later it may be desirable to operate the beam in a partially achromatized mode with the CEMA counter so as to increase the hyperon transmission, improve the accuracy of momentum measurement and (as a consequence of better hyperon acceptance) lower the muon background relative to the situation for a fully achromatized beam. From this point of view the ±1 mr seems generous. Indeed in the final system optimization one may decrease it further in order to gain more ψ range.

Finally, as noted earlier the allowed ±.1 mr of vertical divergence in the hyperon beam effectively translates curves of the sort shown in figures 1 and 2 by our amount α, defined in euation (3) and associated sketch. It is easily seen that

$$\text{Tan } \alpha = \frac{\pm.1}{a} \tag{6}$$

where a is the angular half-width of the vertical beam divergence. For $a = 1$ mr, $\alpha = 5.71°$. For the case illustrated in figure 2 we might want to exclude segment E3 from the Ξ set (for the sign of α which shifts the curves toward negative values of ψ) although C3 would be made cleaner. However, we would probably leave E3 in. By "counting squares" and making the conservative assumption that the annuli of Cerenkov light (rather photoelectrons) are of uniform intensity this adds a probability of 7×10^{-3} of mistaking a Σ for a Ξ for each tube. If we require a double coincidence (between tubes) this becomes $\sim 5 \times 10^{-5}$ probability of counting

Σ as a Ξ. If we use the Σ segments as an anti this probability
will be reduced by another factor of ~ 100 (as we shall see the
counter in better than 99% efficient at the single photoelectron
level).

It thus appears that vertical beam spreads of $\pm$ .1 mr do
not lead to significant degradation of the counter's performance.
An azimuthal (ψ) range of 180° thus appears to be a conservative
estimate. Before leaving this topic we note that the optical
system transmits a total of 270° of ψ range and there is room on
the CEMA anode of 4 cm diameter to accomodate this ψ range for
$\theta_c \lesssim 15$ mr.

We now estimate the yield of photoelectrons for the CEMA
counter. We take

$$L = \text{length of gas radiator} = 6 \text{ m}$$
$$\psi \text{ range} = 180^{\circ}$$
$$A = \text{parameter of Reference 2} = 100 \text{ cm}^{-1}$$

The parameter A characterizes the photodetector, taking into
account the Cerenkov light spectrum and the transmission of
standard optics. The numer N of photoelectrons is given by

$$N = AL \, \theta_c^{2} \tag{7}$$

High quality photomultipliers with fused silica entrance
windows[4,2] have A values ~150 cm^{-1}. The CEMA will have a very
similar (Bi-alkali) photocathode and a fused silica window.

Furthermore the photoelectrons are proximity focussed on the multiplier array and the collection efficiency should be high ($\sim 80\%$) and independent of wavelength. As an exercise, A. Schiz[5] has calculated the A value expected if the photocathode quantum efficiency was the same as for the best RCA tube (RCA spectral response curve #133). Because of the excellent photoelectron collection efficiency, the resulting A value was 200. Of course the CEMA tubes are newer devices and the process of manufacture will no doubt be less than optimum for a while. The A value of 100 can be regarded as a specification of an acceptable tube and as argued above is a reasonable expectation. We then have (at $\theta_c = 14 \ mr$)

$$N = 600 \times 100 \times \frac{180}{360} \times (14 \times 10^{-3})^2$$

whence $N = 5.88$

The single photoelectron efficiency E_1 is

$$E_1 = 1-e^{-5.88} = 99.7\%$$

The doubles efficiency (2 tubes firing) E_2

$$E_2 = (1 - e^{- \frac{5.88}{2}})^2 = 89.7\%$$

We discuss now, very briefly, the expected CEMA tube characteristics. In order to achieve gains of $\sim 10^6 - 10^7$ we require either the curved channel plate of Phillips or the Chevron (Tandem) design such as produced by Gallileo Electro-Optics. Both of these firms indicate that a 4 cm diameter is a

reasonable expectation. In fact, Phillips offers a CEMA tube
of 4 cm diameter with 100 anode segments, although as far as
is known, the first model which is being built for Meunier at
CERN has not yet been delivered. Typical channel diameters are
15-25 μm. It appears that tubes of diameter significantly
greater than 4 cm are possible to build but that, at this point,
the cost would be very substantially greater than for a 4 cm diameter
tube.   It thus appears prudent to assume a 4 cm diameter CEMA.   If
we wish to accomodate the patterns shown in the sketch on p. 10,
placing 8.5 mr to 23.5 mr on two tubes, we require an optical
system focal length f = 118.34 cm. As has no doubt been tediously
evident to my patient colleagues, an optical system with such a
short focal length and the requisite angular coverage has been
a major preoccupation of the author since January 1975.   A
successful system has been designed and is discussed in the next
section.   Table V summarizes the characteristics of the CEMA
tube counter.

We conclude this section with a brief enumeration of the
advantages which the CEMA type of multiplexed Cerenkov counter
offers for the E-97, P(E)-353 research program.

1. The beam phase space acceptance is an order of magnitude
    greater for the CEMA counter than for the DISC.   We
    illustrate this point by comparison at 180 GeV/c.
    The latest version of the achromatic beam design[3] provides
    an acceptance of

$$\Delta\Omega \frac{\Delta P}{P} = 4 \times 2.5 \times .2 \times 3 \ \mu Ster-\% $$
$$= 6 \ \mu Ster-\% $$

Table V

Characteristics of Proposed CEMA Tube Cerenkov

Counter for FNAL Hyperon Beam

Number of CEMA tubes	2
Diameter of CEMA	4 cm
Microchannel diameter	15 → 25 μm
Cerenkov angular range detected[a]	8.5 mr → 23.5 mr
Number of azimuthal sectors/tube	3, $\lfloor \pm 25°, \pm(25°-45) \rfloor$
Radial width of anode segments	118.34 μm (0.1 mr)
Number of annular divisions/tube	150
Number of anode segments/tube	450
Total number of anode segments/counter	900
Optical system focal length	118.34 cm
Length of "Optics Head"[b]	~150 cm
Nominal length of gas radiator	6 m
Nominal Cerenkov angle for Σ^- at 180 GeV/c for $\Sigma^- \Xi$ separation	14 mr
Photoelectron yield (at 14 mr, 6 m)	5.88
Single photoelectron efficiency (14 mr, 6m)	99.7%
Two tube coincidence efficiency (14 mr, 6m)	89.7%
Microprocessor decision time (total processing time)[c]	1.2 → 3.9 μs

(a) Includes beam angular divergence

(b) cf. Section III

(c) cf. Appendix I.

However, as pointed out by A. Roberts,[3] the correlation between momentum and direction together with the narrow slit needed for the DISC leads to an effective reduction of $\Delta\Omega \frac{\Delta P}{P}$ by approximately a factor of 2 thus

$$\Delta\Omega \frac{\Delta P}{P} \bigg|_{DISC} = 3 \text{ } \mu Ster\text{-}\%.$$

We use the Stefansky design report[1] to estimate the acceptance which can be achieved with the CEMA counter. The Stefansky beam fits well into the CEMA counter as described here with one small modification. The exit beam is 2 cm wide whereas the beam hole in the mirror is 1.7 cm in diameter. We must thus collimate at the exit of the doublet. We take a full beam width of 1 cm and from figure 5 of reference (1) we find the transmitted beam is reduced to 73% of its previous value. If we further limit the accepted angular range to ± 1mr we see from fugure 4b of reference (1) that the transmitted beam is reduced by another factor of .65. From figures 3, 5 and 6a of reference (1) we estimate

$$\Delta\Omega \frac{\Delta P}{P} \bigg|_{Stefansky} = 1.2 \times 2 \times \frac{2}{15} \times 100 = 32 \text{ } \mu Ster\text{-}\%.$$

Applying our two reduction factors we conservatively estimate that a practical CEMA beam will have

$$\Delta\Omega \frac{\Delta P}{P} = 15 \text{ } \mu Ster\text{-}\%.$$

One other factor remains in the comparison - the allowed
length of the hyperon production target in the beam direction.
In the achromatic design the target must be kept to not more
than 6 cm. The Stefansky report does not specifically
discuss the allowed target length but since it is a much
less tightly focussed beam it seems very likely that a
substantially longer target could be used. At Brookhaven
a 10" Be target proved optimum. Since the nuclear absorbtion
length in Be is 36 cm it seems highly probable that at least
a factor of two in hyperons per incident proton can be
obtained from a longer target. We thus see that in a
practical as well as theoretical sense the CEMA counter can
be used with a factor of ten greater yield of hyperons per
incident proton. Finally we note that if the Stefansky design
were reexamined from the point of view of limiting the beam
size to 1 cm and the angular spread to ±1 mr with a more
efficient slit system than suggested above, it is likely
that some of the .73 x .65 loss factor could be recovered.

This substantially increased acceptance and the associated
simpler beam design have a number of important advantages for
the E-97, P(E)-353 etc., program.

a) Our dependence on the perfection of the hyperon beam
design and construction is much less critical. For
example we could afford to use a target substantially
smaller than the proton beam size if it should turn out
that our proton spot is too large.

b) The muon and general room background which are basically produced by incident protons would be an order of magnitude smaller.

c) We could use the increased acceptance to push our yield measurements for Σ (and X?) closer to the kinematic limit.

d) If we wanted to carry out a two arm "Ting" type of experiment we would probably want larger hyperon production angles (recall $\theta_{TING} = \frac{1}{Y_{cm}}$) and would almost certainly be limited by incident flux and associated backgrounds.

2. The multiplex feature of the CEMA counter means that all hyperons in the beam are simultaneously tagged. Thus Σ, Ξ, Ω data could be accumulated simultaneously. Not only would this save a factor of two or three in running time but also would be very useful in helping to reduce systematic errors. For example, beam monitoring errors would, at least to first order, cancel out in the determination of the relative cross sections. The recorded outputs also constitute very powerful "anti" data.

3. A related feature of the multiplexing vis a vis backgrounds and systematic errors is the fact that the CEMA counter outputs on "pre-scaled beam" events can be analyzed off-line to give the equivalent of a continuous, simultaneous set of "pressure curves" during the run and should allow very good background subtraction under the peaks. This will probably only be important near the limits of our operating

range but should be very useful when needed.

4. In the "search for new particles" part of the experiment the ability to cover 8.5 mr to 23.5 mr at one pressure setting will enormously speed up the data taking. It should allow a careful search over beam beam momentum as well as mass - a procedure which would be prohibitively slow with the DISC.

5. In a two arm experiment the ability of the CEMA counter to simultaneously tag all beam particles from π to Ω will reduce running time by a factor of 9 to 25 (depending on the extensiveness of the combinations of particle pair masses desired) in addition to the increased beam acceptance mentioned in 1. Thus for two arm experiments CEMA counters offer effective data rate improvements of a factor $\gtrsim 1000$.

6. The broad angular coverage, the relatively short "Optics Head" (150 cm), and the CEMA tubes with multisegmented anodes provide a system of great flexibility. Radiator length can be added or subtracted to raise the upper momentum limit or lower the lower momentum limit. Various microprocessor programs can be loaded that offer different trade-offs between detected mass range, cleanliness of separation, and beam phase space acceptance. Since we might actually discover some new phenomena, this unusual

ability to respond rapidly and easily in a previously
unanticipated fashion might be of considerable importance.

7. The multiplex CEMA tube counter would, finally, give our
group experience with a new technology (the CEMA tubes)
and would continue and deepen our expertise with the
fast growing microprocessor technology.

III. Optical System

In this section we describe briefly but (hopefully) with precision, the optical system which could be used with the CEMA tubes or with a slit system and normal photomultiplier tubes as a more or less standard differential Cerenkov counter. In section IV we shall evaluate the performance as a "normal" diferential counter.

The basic layout is shown (plan view) in figure 3. The optics are symmetrical about the beam centerline. Figure 4 shows the "Optical Head" of the counter in greater detail. As shown, the Cerenkov light in the ψ range $\pm 67.5^\circ$ is reflected by a two mirror system onto a focal plane. Similarly, a symmetric pair of mirror on the other side of the beam line focusses Cerenkov light in the ψ range $180^\circ \pm 67.5^\circ$.

The two mirrors on a given side have the same optical axis which is inclined to the beam direction by 16.0 mr.

This optical system is essentially equivalent to the Swarzschild version of a Cassegrain telescope.[6,7] In brief, in a two mirror system it is possible to figure the mirros so as to simultaneously eliminate spherical aberration and coma. Chromatic effects are of course absent in reflecting systems. The remaining aberrations of astigmatism and curvature of field are minimized by choosing the direction of the optic axis to be parallel to the average Cerenkov light direction and for the small "field of view" (in a telescopic sense) of the counter are quite acceptable.

FIG 3

1 meter

PLAN VIEW

FIG. 4

Labels visible in figure:
June 10, 1975

FOCAL PLANE

OPTICAL AXIS (16. mr. w.r.t. Beam.)

$\psi = 45°$

$\theta = 23.5$ mr

$\psi = 67.5°$

$\theta = 6.5$ mr

0   50   BEAM AXIS   100   150

10 cm
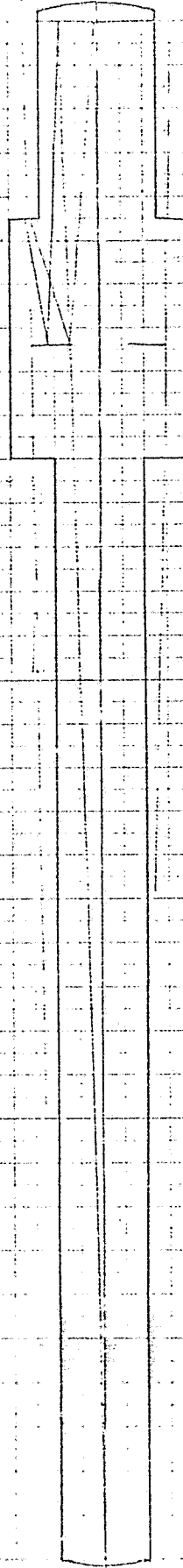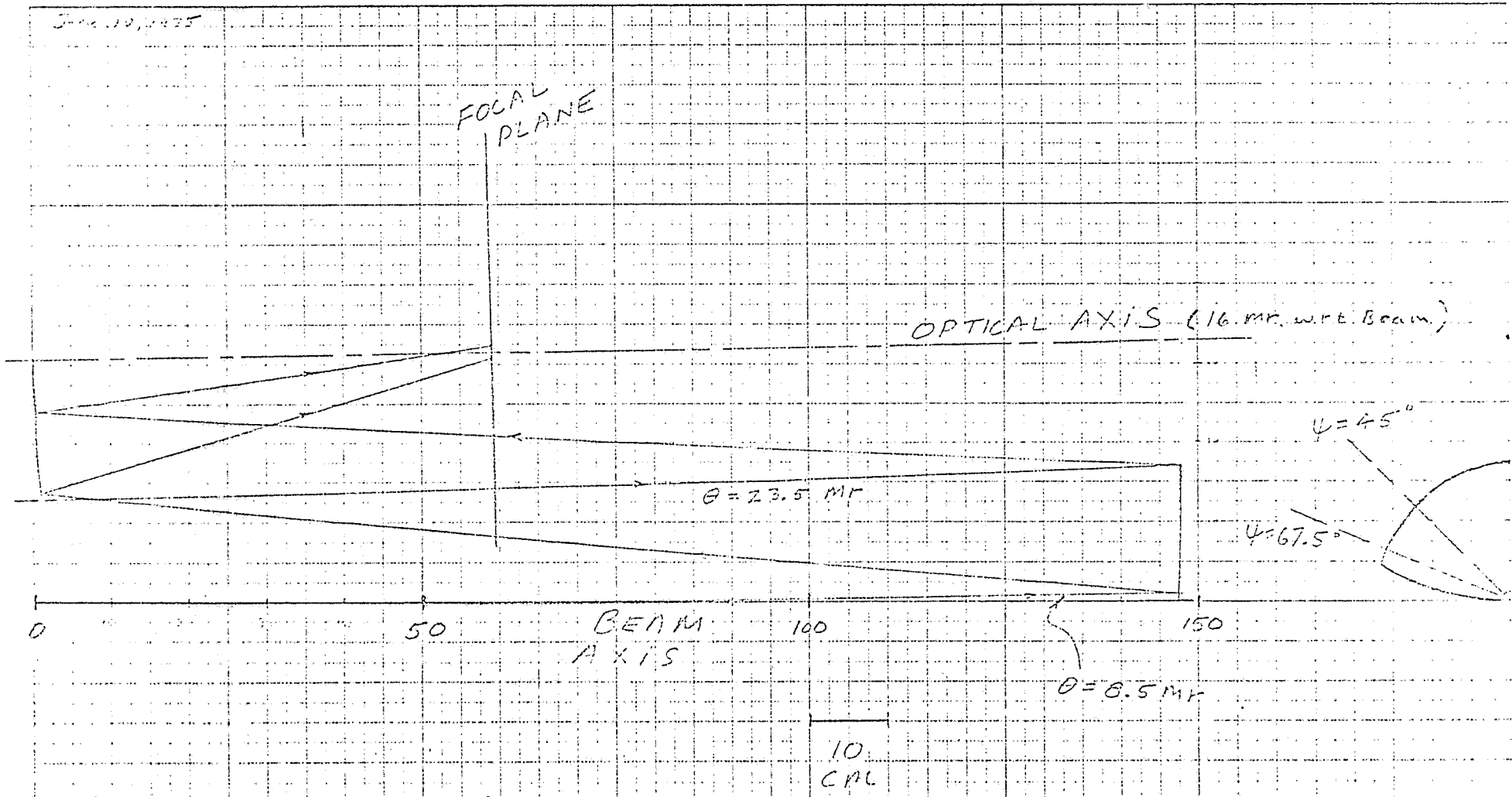
The counter will operate at pressures of a few atmospheres e.g.
at 180 GeV/c and $\theta_c(E) = 14.000$ mr the pressure is 3.65 atmospheres
of He (absolute). At lower momenta one can switch to Neon
which has almost identical chromatic dispersion but has about
2.8 times as much multiple Coulomb scattering as He for the same
Cerenkov angle. However, the multiple scattering is relatively
small, e.g. 4 atmospheres of He, 700 cm long, give an rms
transverse momentum of 1 MeV/c. Thus the maximum gauge pressure
can conservatively be taken as 5 atmospheres and a relatively thin
window used (~6 mm gives a safety factor of 4 and allows for minor
surface scratches[8]). For such a thin window, the geometrical
aberrations are alsmot negligible and can be compensated in
the final design by a slight refiguring of the mirror surfaces.
The preceding conclusion was reached independently by the author
and verified by a professional optical consultant[9] who reviewed
the optical system design. For this reason, in the analysis which
follows, the window was not included in order to save time. When
the design is finalized, the necessary refiguring will be calculated.

The Swarzchild design procedure yields a differential equation
for each mirror surface. The solutions of the equations in exact
form involve inconvenient variables and transcendental functions.
It is traditional and useful to express the mirror surfaces by power
series expansions of their meridical sections (the mirrors are
surfaces of revolution). If R represents the perpendicular
distance of a surface point from the axis and z the distance of
the point from a plane which is tangent to the surface at the

vertex we write:

$$z = a\,R^2 + b\,R^4 + c\,R^6 + d\,R^8 \qquad (8)$$

Both mirrors are concave and taking the positive z directions
so that a > 0 in equation (8) we list in Table VI the
coefficients for the two mirrors.

Table VI

Shape Coefficients for Mirror Surfaces[a]

	a	b	c	d
Large Mirror	$.845023 \times 10^{-3}$	$-.75425 \times 10^{-8}$	$-.215433 \times 10^{-12}$	$-.8028 \times 10^{-17}$
Small Mirror	$.253507 \times 10^{-2}$	$.48272 \times 10^{-7}$	$-.4481 \times 10^{-11}$	———

(a) Units of z, R are cm.

Figure 5 shows the deviations of the surfaces from the
(osculating) spheres. As can be seen, they are "mild" aspherics.
Although they are not paraboloids there is a good possibility[9]
that they are conical surfaces of revolution to an acceptable
degree of accuracy. This point, which offers greater economy
and ease of polishing and testing will be investigated in the
near future.

The magnitude of the residual geometrical aberrations were
calculated with an exact ray tracing program. These are
illustrated by the "spot diagrams" of figure 6, 7, and 8, which
treat the extremes (and most severely aberrated) of the Cerenkov and
azimuthal angular ranges over which the counter is designed. The

DEVIATION FROM SPHERICAL SHAPE

FIG. 5
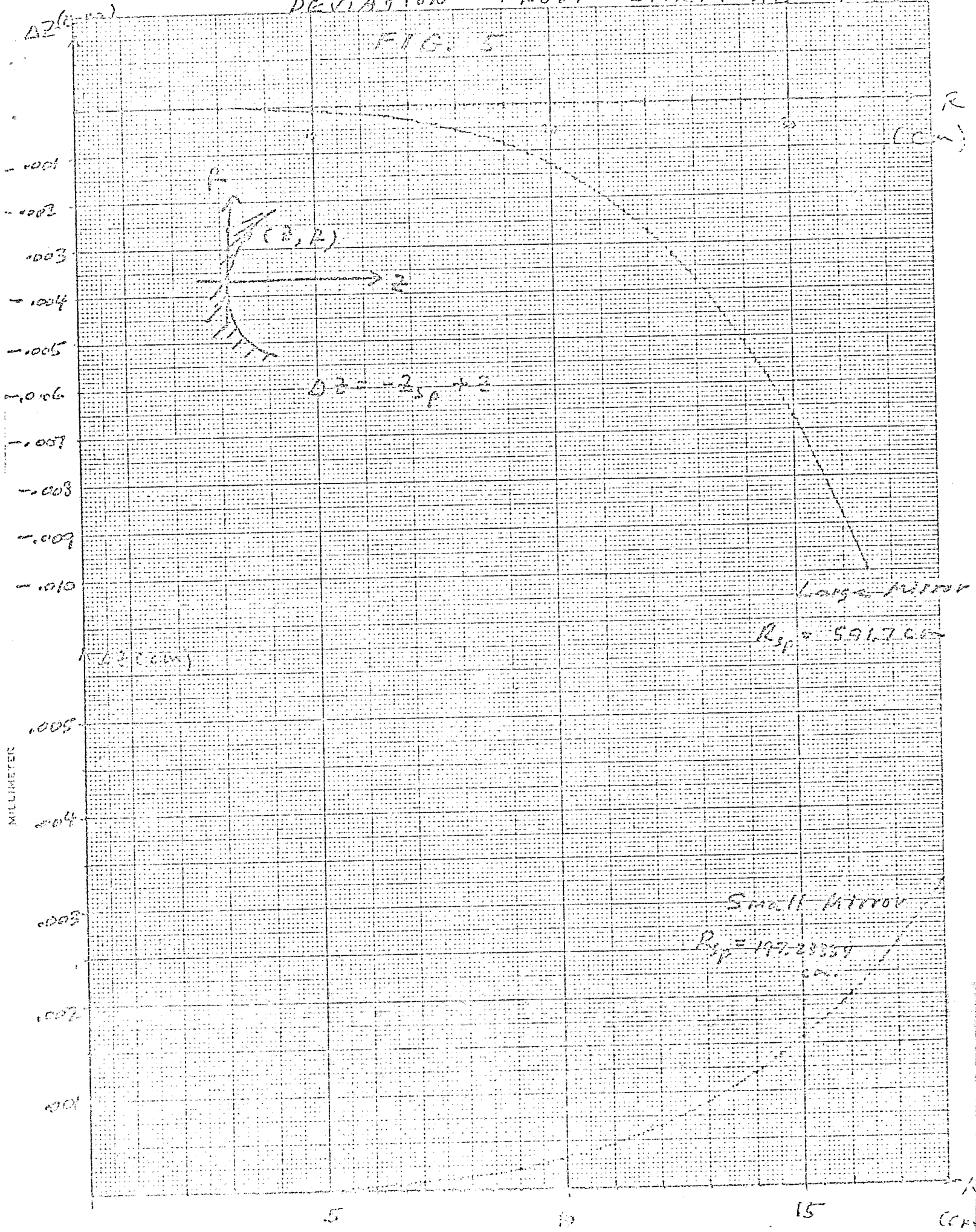
Large Mirror

$R_{sp} = 591.7$ cm

Small Mirror

$R_{sp} = 177.2935$ cm

$D^2 = \tilde{z}^2 - 2\rho\tilde{z} + \tilde{z}^2$

$F = 118.37\ cm$

$F_{m} = 795.85\ cm$

$e = 148.9237$

$\theta_c = 8.5\ m$, $\phi = 180°$

7.4

7.5

7.505

$\theta = 8.5\ m$, $\phi = 135°$

8.090

$\theta_c = 23.5\ mr$

Two Mirror System $F = 118.34$ $F_n = 295.85\,cm$

$e = 1.47.\,925$

$\theta_c = 8.5\ mr$

$\phi = 112.5°$

DIAM = .0662 MR

.001

7.93.6

12.747

.001

New Mirror System $r = 118.71$

$r_{cm} = 275.85$

$r = 147.925$

$\delta = 13.5$ mr

$\delta = 12.5°$
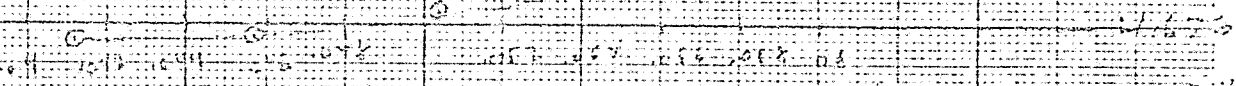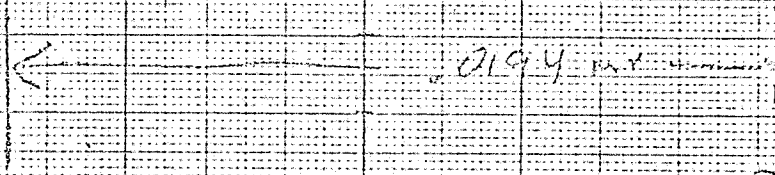
←   →   .19.4 mr →

"spots" correspond to the focal plane positions of rays emitted at different points (the two extremes and the center) along the radiator length. As can be seen, at the small Cerenkov angle extreme the maximum aberration is ±.0024 mr and at the largest Cerenkov angle and the extreme φ value it is ±.01 mr. These values are small enough to be completely negligible. The diffraction limit is typically ±.002 mr so that the surface quality need not be quite as good as for diffraction limited optics. Our consultant[9] estimates that quarter wave polishing would be conservative. For completeness Table VII summarizes the optical system parameters which are also illustrated in Figure 4.

Table VII

Optical System Parameters

Displacement of optical axis from beam axis (at downstream end)	33.0 cm
Angle of optic axis with respect to beam axis	16.0 mr
Paraxial focal length of large mirror	295.85 cm
Paraxial focal length of small mirror	98.617 cm
Distance of focal plane from vertex of small mirror	59.17 cm
Overall system focal length	118.34 cm
Mirror shape parameters --- see Table VI	

The foregoing aberration patterns were calculated at the paraxial image plane. A study was carried out, using the ray trace program to see if a slight displacement of the system focal plane would give improved performance and conversely to determine the precision to which the focal plane must be located. Figures 9, 10, 11, 12 show the results as ray projections on the x, z or y, z plane. As can be seen, the paraxial focal plane (z = 0) is as good an overall choice as can be made. Taking ±.01 mr as a very conservative limit on the change of apparent θ_c we find that the focal plane must be accurately located to within ±.6 mm which should be achievable.
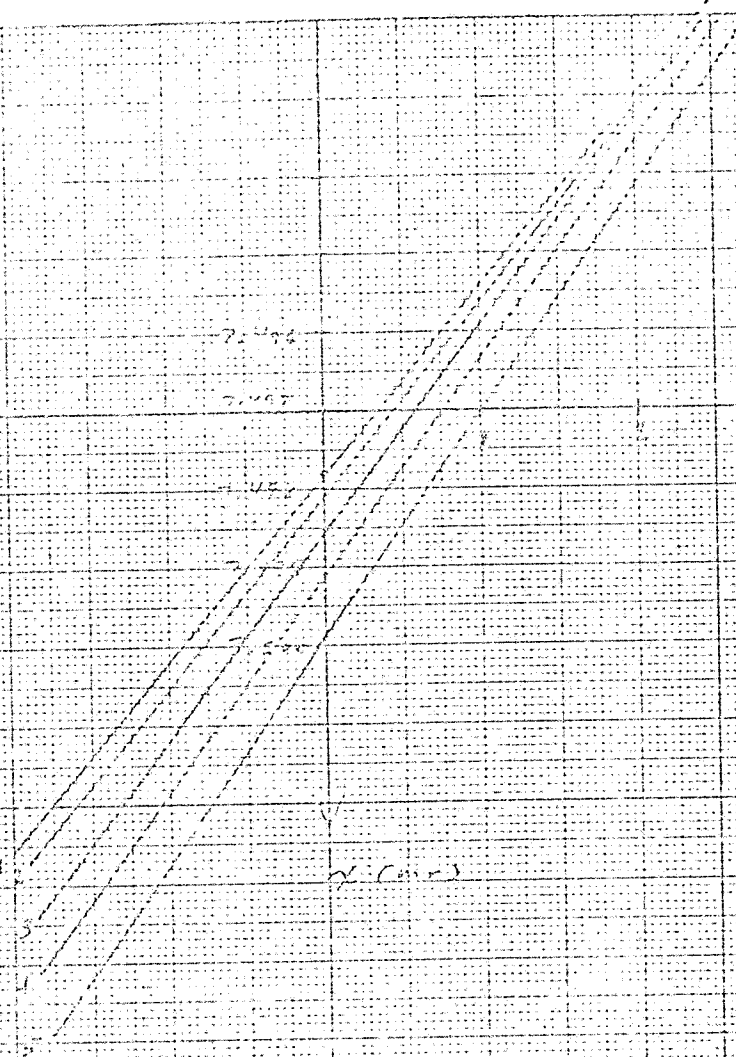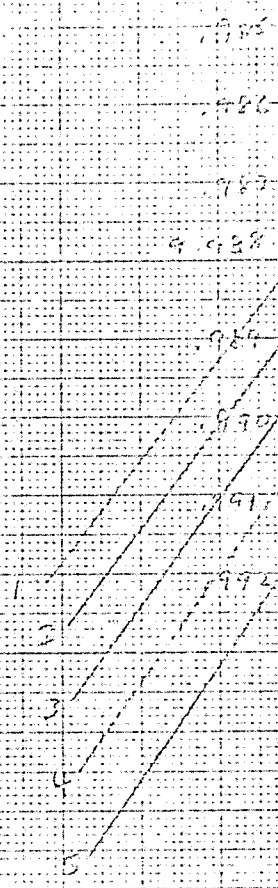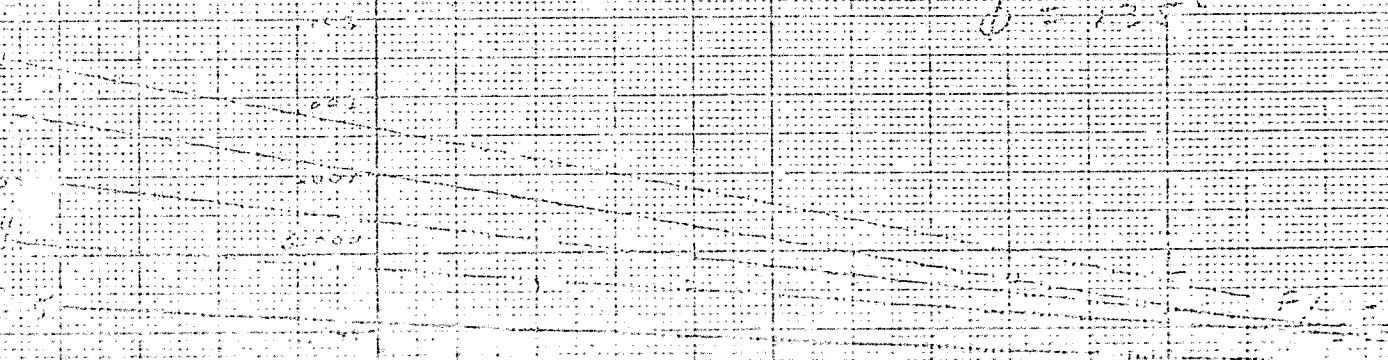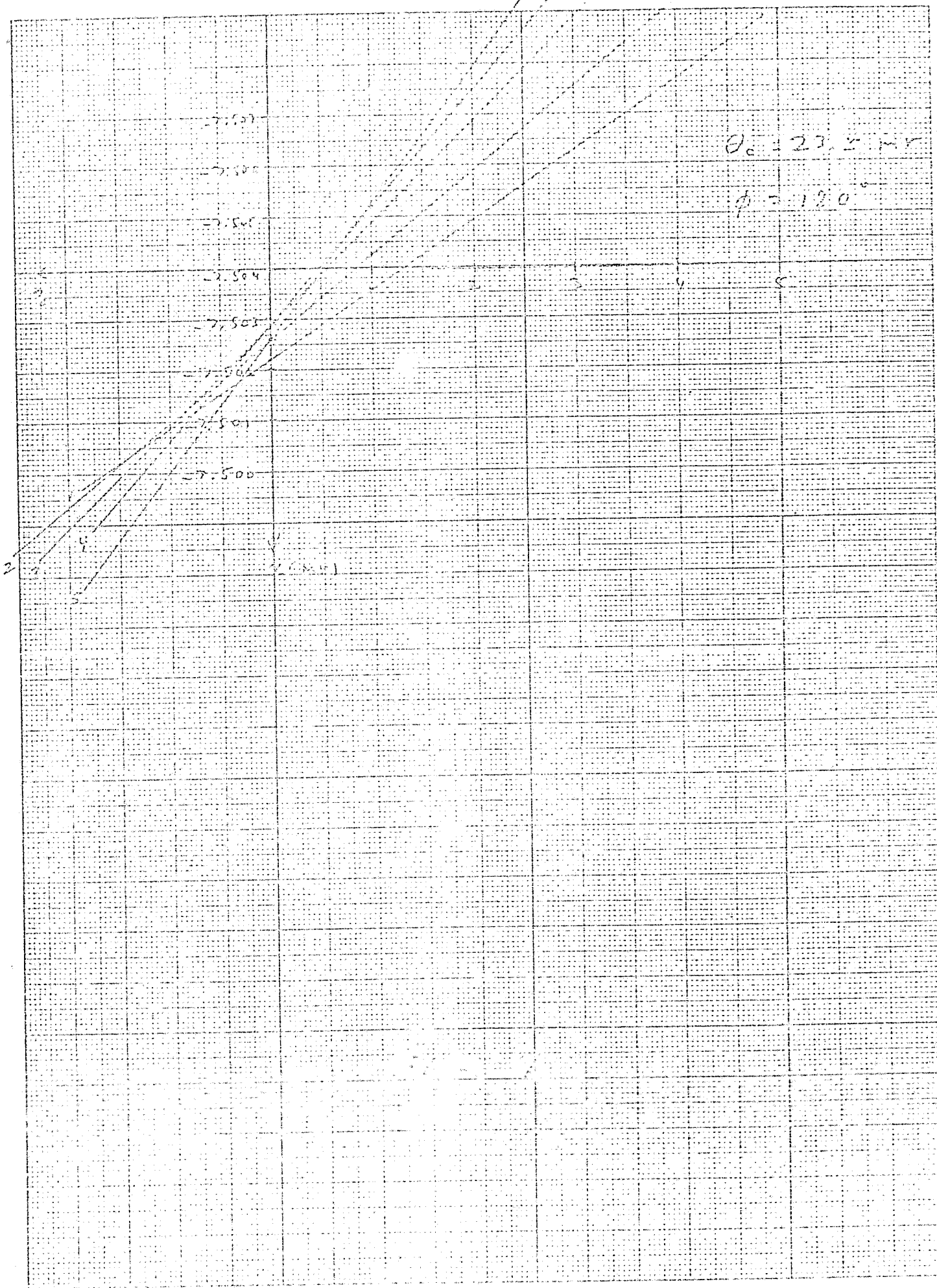
IV. The Use of CEMA Counter Optics with Standard Photomultipliers

Although we believe that the CEMA counter described in the preceding sections represents the most desireable approach for the Mini hyperon Cerenkov counter we recognize that the uncertainties in cost, funding, production schedules and reliability of the relatively new CEMA tubes makes a "fall back" position highly desireable.

The invention of the achromatic beam design[3] is the key to such a "fall back" position in that it makes it possible to use either a DISC or a differential counter with narrow slits with useful acceptance. As we shall discuss, the performance of the optical system of section III with slits and normal phototubes, and very likely, with the addition of mirrors and phototubes to detect 'wrong' particle light in anti-coincidence is comparable to that of the E-69 DISC and offers the advantage of flexibility in the choice of radiator length and Cerenkov angle.

We have already shown that the only significant "aberration" is the inherent chromatism in the radiator gas. Tables I thru IV show the choice of Cerenkov angles needed to achieve $\gtrsim 2$ dispersion width separation of Σ and Ξ from 100 GeV/c to 250 GeV/c. These are clearly within the accepted range of the optical system. We note that since the beam must be made sufficiently parallel to allow the separation in angle of Σ the full ϕ range of $\pm 70^\circ$ could be used. Moreover we could select phototubes with $A = 150$ cm⁻¹ so that the yield of photoelectrons, relative to that calculated in section II, would be substantially greater. For example, at

180 GeV/c we could have

$$M = \frac{270}{180} \times \frac{150}{100} \times 5.88 = 13.23$$

In the final design we may want to trade off some of this ϕ range for "anticoincidence ϕ range." In any case, even though the Cerenkov angle is only 14.000 mr instead of 25 mr as in the DISC, there is ample light. The only questions remaining are the choice of slit width and allowable beam spread (which need not, and indeed, should not be the same).

Because of time limitations we forego a complete momentum dependent analysis and consider the typical case of 180 GeV/c. The situation is illustrated in figure 13. We have chosen:

$$\Delta\theta_{slit} = .23 \text{ mr}$$

$$\Delta\theta_{beam} = \pm.04 \text{ mr}$$

These give the same absolute angular separations as for the DISC. Since our geometric aberrations are much smaller than the chromatism our images should have a correspondingly sharper edges than the DISC. Slit edge scattering should be the same as for the DISC. Finally, we have "anti" capability as well as two fold coincidence capability so these choices should be a valid comparison.

The DISC beam angular acceptance in $\Delta\theta_{beam} = .07 \times$ factor for momentum angle correlation in the beam. This factor has not

14 mr Diff Counter

DISC

Microwave
Signal

i

ii

iii

iii

7.65

iii

180

FIG. 13

been calculated explicitly for the counter proposed here but
clearly will have much smaller affect since the slit is ~ 3 times
as wide as the beam spread. We would estimate that at reasonable
discriminator settings (1 photoelectron) the full beam spread
would be counted at essentially the full efficiency. We thus
conclude that the counter proposed would have ~ 2 x acceptance
of the DISC.

We conclude this section with a brief estimate of the cost
of the optics and mechanical parts. Three firms have made cost
estimates on the optics with prices ranging from $27,000
(perkin Elmer) to $9,000 (XYZ Technical Center). The median
price, quoted by Frank Cooke, Inc. (incidentially, the same
firm which supplied the optics for the 15' bubble chamber) was
$19,000. Irv Winters and Andy Disco have estimated $20,000
for mechanical parts and gas system. We summarize our cost estimate

Optics	$19,000
Mechanical parts and gas system	20,000
Phototubes	3,000
Contingency	3,000
Total	$42,000

This seems likely to be conservative estimate for construction
of a differential counter utilizing DISC counter optics.
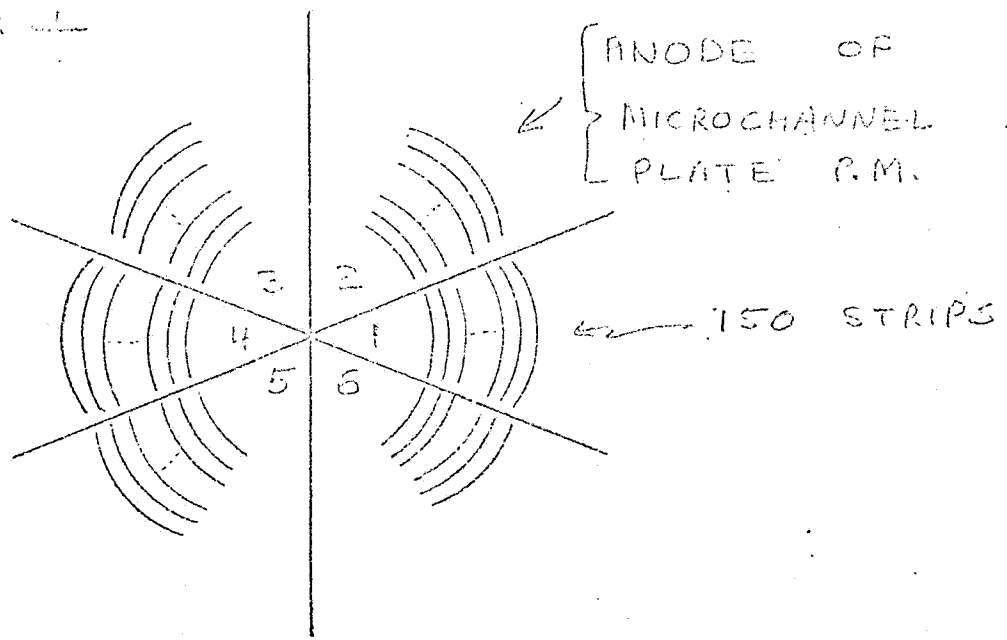
V. Proposal

The following seems a "modest"[10] but appropriate proposal

1. Proceed now with the achromatic beam and the CEMA optics used as a differential counter.

2. Build as much flexibility as possible into the designs e.g. equipment on rails, CEMA "optics head" readily convertible to either normal a CEMA photomultiplier tube. Especially, study how to retune the beam for partial achromatization and increased acceptance.

3. Proceed as vigorously as possible with development of CEMA tubes.

References

1. R.J. Stefanski, "Hyperon Beam with Quadrupole Focusing", EN-239, 2257, December 10, 1971. Clearly operation is possible and somewhat easier with the achromatic beam design of reference 3.

2. J. Litt and R. Meunier, "Cerenkov Counter Technique in High-Energy Physics," Annual Review of Nuclear Science Vol. 23 (1973), Annual Reviews Inc., Palo Alto, California.

3. C. Ankenbrandt, "A New Hyperon Beam Concept" Internal Fermilab Note, February 24, 1975; A. Roberts, "Preliminary Report on the Design of an Achromatic Beam for Experiments 97 and 353", Fermilab E97-1, May 1, 1975; A. Roberts, Private Communication.

4. D. Yovanovitch, et al., "A Threshold Gas Cerenkov Counter for a 200 GeV/c Beam," Nuclear Instruments and Methods $\underline{94}$, 477 (1971).

5. A. Schiz, Private Communication.

6. K. Schwarzschild, "Untersuchungen zur Geometrische Optik, II-Theorie der Spiegeltelescope," Royal Observatory at Gottingen 1905 (Abh. Königl. Ges. Wiss. Göttingen, Math. Phys. Klasse, $\underline{4}$ (1905-1906), No. 2).

7. A very useful analysis of the aplanatic mirror pair is given in Henri Chretien, "Calcul des Combinaisons Optique" Paris, 1949 pp. 377-383.

8. I. Winters, Private Communication.

9. Dr. Seymour Ronin, Private Communication.
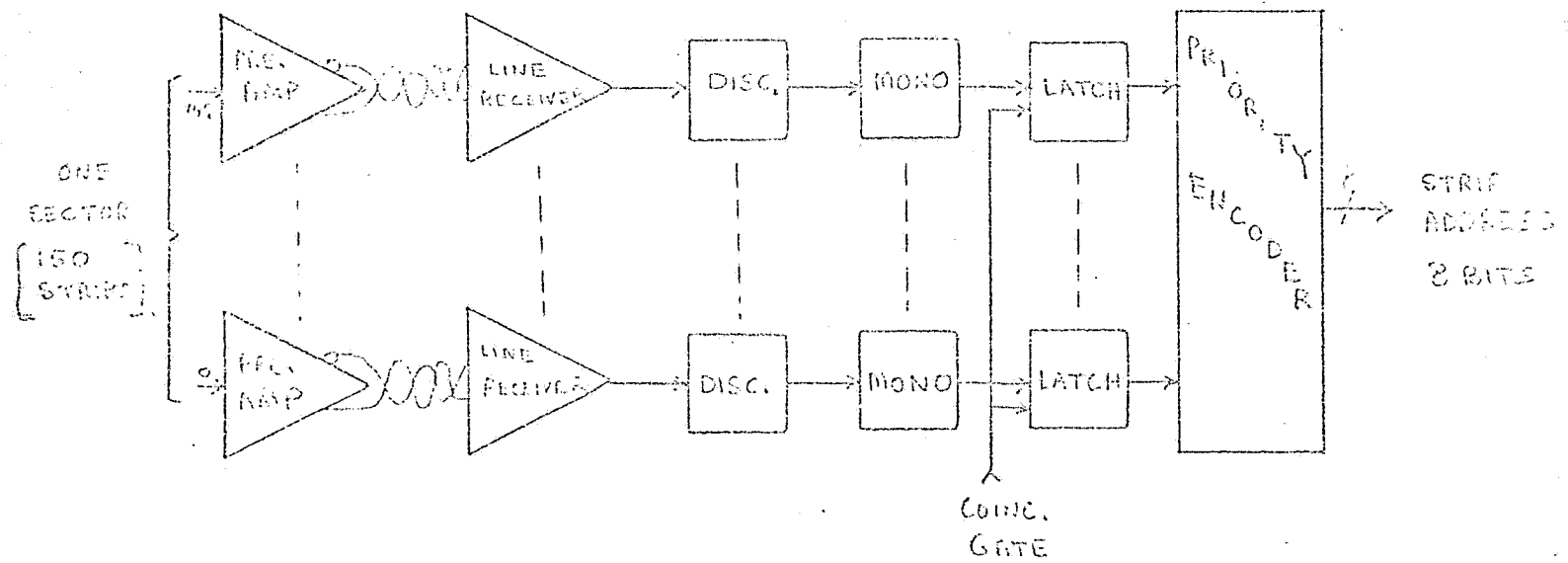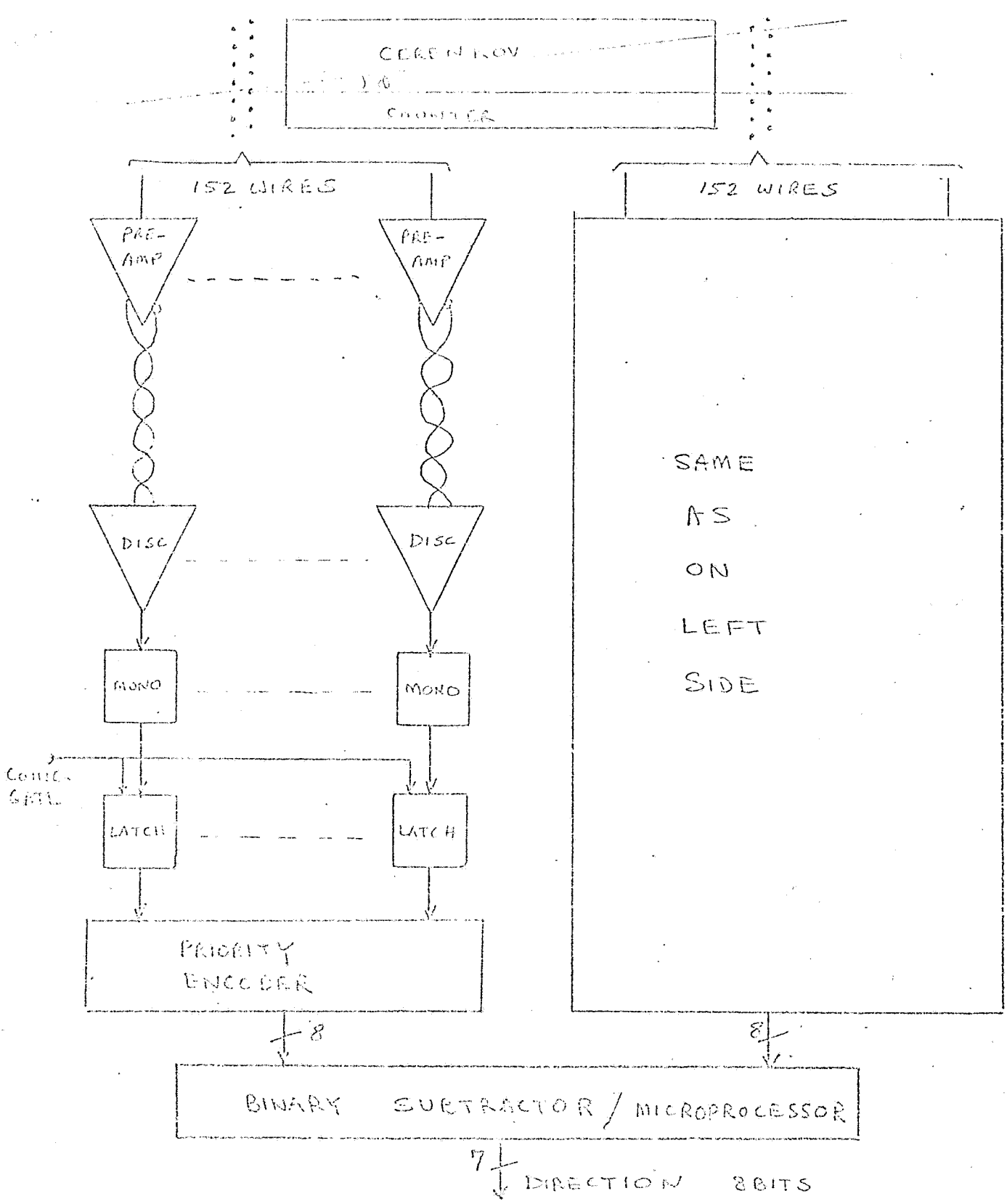
10. Apologies to the memory of J. Swift.

ANODE OF
MICROCHANNEL
PLATE P.M.

150 STRIPS

3 2
4 1
5 6

NO. OF STRIPS/SECTOR = 150
TOTAL NO. OF SECTORS = 6
TOTAL NO. OF STRIPS = 150 × 6 = 900

M.C.
MAP

LINE
RECEIVER

DISC.

MONO

LATCH

PRIORITY ENCODER

ONE
SECTOR
[150 STRIPS]

M.C.
MAP

LINE
RECEIVER

DISC.

MONO

LATCH

STRIP
ADDRESS
8 BITS

COINC.
GATE

BAND WIDTH = 1/200 nSec

DATE 6-11-75	YALE UNIVERSITY
	TITLE PSCLD
PREPARED S.E.	FRONT END ELECTRONICS
CHECKED	GROUP YPAS C.27	DRAWING NO.

CERENKOV

COUNTER

152 WIRES

152 WIRES

PRE-AMP

PRE-AMP

DISC

DISC

MONO

MONO

LATCH

LATCH

PRIORITY ENCODER

SAME

AS

ON

LEFT

SIDE

8

8

BINARY SUBTRACTOR / MICROPROCESSOR

7 DIRECTION 8 BITS

DATE 6-11-75	YALE UNIVERSITY	
	TITLE PSCLD	
PREPARED BY	DIRECTION FINDER	
CHECKED	GROUP YALE-E77	DRAWING NO.

A NEW HYPERON BEAM CONCEPT

Chuck Ankenbrandt

In previous hyperon beam designs, a large angular dispersion exists at
the exit of the magnet system. While this correlation between momentum
and horizontal angle somewhat simplifies hyperon momentum measurements,
it severely complicates any attempt to trigger on and/or to tag specific
hyperons via a Cerenkov detector.

This note outlines a new beam design which solves this problem with
surprisingly few attendant disadvantages and some accompanying advantages.
Concepts are emphasized because there has been no real attempt to optimize
the design which will be described; I am circulating it in preliminary
form in order to enlist the superior intuition of those of you who have
done hyperon experiments before.

The basic new idea is to remove the net angular dispersion by incorporat-
ing a reverse bend downstream of the main channel sweeping magnet. (It will
turn out that a quite short reverse bend will suffice.) The adverse effects
on background muon fluxes at the experiment which might seem at first sight
to result from this modification can be desi avoided by designing the second
bending magnet with a horizontally narrow pole tip and narrow coils, so that
most muons will in fact enter the return yoke of this magnet where they
will continue to be swept away from the hyperon beam as in Figure 1.
The second dipole magnet then will <u>add</u> to the background sweeping power of
the first; ideally it would be superconducting to minimize coil cross-section.

A logical place to incorporate this second bend is between the two
quadrupole magnets which are still included in the design; this provides
separation between the quads, thereby allowing their lengths to be reduced.
Relative to the original Fermilab beam design (Stefanski FN-239), the overall
beam length can then be reduced if we start from scratch with a new shorter
dipole as the first beam element; or the length will only slightly increase
if we stick with the presently existing magnet. The CERN design could be
modified to this configuration by merely reversing their second dipole.

Figure 2 illustrates a first attempt at an actual beam design with
realistic parameters fit by TRANSPORT. (See me for the complete TRANSPORT
output.) It is worth emphasizing that Figure 2 is to scale in z, that is,
a quite short reverse bend will make the emerging beam achromatic. The

reason is that the horizontally focusing quadrupole already cancels most of
the momentum dispersion of the beam, particularly when separation is provided
between the quads and when the second quad focuses horizontally. The following
result is most pertinent to the Cerenkov detector design: for an initial
beam phase space of $(\pm)0.5$ mm)X($\pm$ 0.5 mr) in both views and dp/p=$\pm$ 5%, the
output beam has angular spreads of $\pm$ 0.035 mrad and $\pm$ 0.14 mrad in the
horizontal and vertical directions respectively. The vertical angular
spread is larger because the effective focal length is shorter in the vertical.
Nonlinear chromatic effects in the quadrupoles, not included in the TRANSPORT
calculation, would tend to increase these angular divergences; they can
presumably be kept to tolerable levels by limiting the momentum spread of
the beam.

IMPLICATIONS FOR CERENKOV COUNTER

The simplifications which result for the Cerenkov counter are enormous.
Simple circular apertures in the focal plane of a DISC-type counter will
select definite velocities. (In practice some azimuthal segmenting of aper-
tures may be desirable as in standard DISC designs; but the essential
point is that all images will be concentric circles.) In a broad-band
beam, velocity selection will not suffice for particle identification in the
most stringent cases (if dp/p=$\pm$5%, then $m_{\Sigma}/p_{min} \cong m_{\Xi}/p_{max}$); however a
crude measurement of momentum (as might be provided by say a horizontal posi-
tion measurement at the quadrupole exit: position and momentum are fairly
well correlated there) would suffice for particle identification. One can
easily conceive then a two-dimensional matrix of Cerenkov ring radius
versus horizontal PWC position to select specific hyperons for the trigger.
I need hardly emphasize that DISC-type counters are well-designed, existing,
debugged, proven devices. The savings in design effort and probably in cost
are large. Detection efficiencies will also be most likely considerably
larger, not only because the whole Cerenkov ring is usable but because high-
grade commercially available photomultipliers can be used.

IMPLICATIONS FOR HYPERON MOMENTUM DETERMINATION

The beam momentum can no longer be determined directly from horizontal
angle; however, no essential complication should ensue. That is, a horizon-
tal position measurement at two places, say between B_L and Q_V and between
Q_V and B_R (i.e. on either side of the vertically focusing quad), will still
determine the momentum although the algorithm will be more complicated.

For example, for the specific beam design already described, the horizontal positions x_u and x_d upstream and downstream of the vertically focusing quad are given by

$$x_u = x_o + .5\ x_o{}' - .075\ \delta$$

and

$$x_d = 1.24\ x_o + .794\ x_o{}' - .145\ \delta$$

where $x_o, x_o{}'$, and δ are the position, slope, and momentum offset of the original ray at the target in units of cm, mrad, and % respectively. Eliminating $x_o{}'$ from these equations gives

$$.794\ x_u - .5\ x_d = .174\ x_o + .0128\ \delta$$

Using this linear combination to measure momentum and assuming standard deviations of 60 microns on x_u and x_d and a horizontal target size of 1 mm, we find an uncertainty of $\sigma_P = \pm\ 0.6\%$, with approximately equal contributions from chamber resolution and target size. This is only a little worse than the accuracy that can be achieved by measuring the horizontal angle in the Stefanski design.

OTHER CONSEQUENCES

There are other real advantages to a highly parallel beam. Beam halo can easily be eliminated by requiring that the beam be parallel, say by chambers on either side of the Cerenkov counter. Straight-thrus can similarly be rejected by looking at the beam angle downstream of the interaction or decay region. Beam veto counters can be made smaller. Further, if it becomes necessary to deaden the beam region of downstream detectors, these dead spots can also be made smaller. Finally the acceptance will be slightly larger for a given solid angle subtended by downstream detectors and/or apertures.
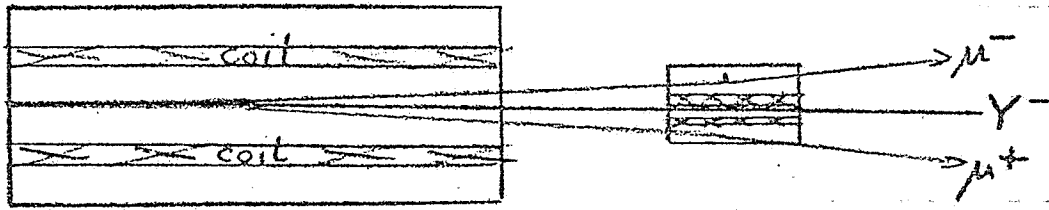
Fig.1. Effect of 2nd dipole on muons (artist's concept)

30 kg × 5 meters   12 kg/cm 28.5 kg 12 kg/cm
                    1.38 m.   1.25 m. 0.92 m.

B_L Q_V B_R Q_H

0   2 m   4 m   6 m   8 m   10 meters

HORIZ

10 mm
5 mm   c (0.5 mm) ×10
        s (0.5 mm)
                    p (5%)

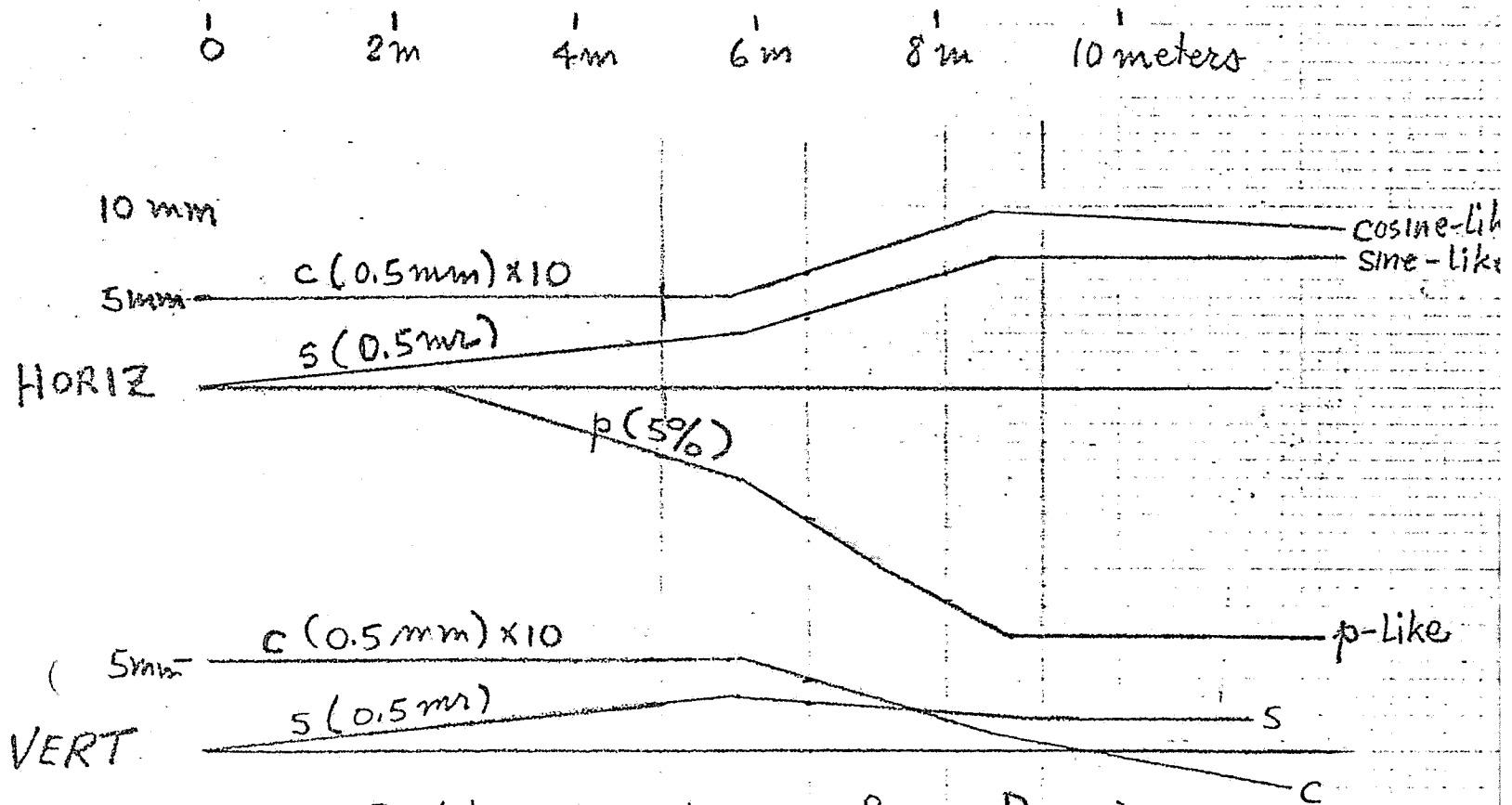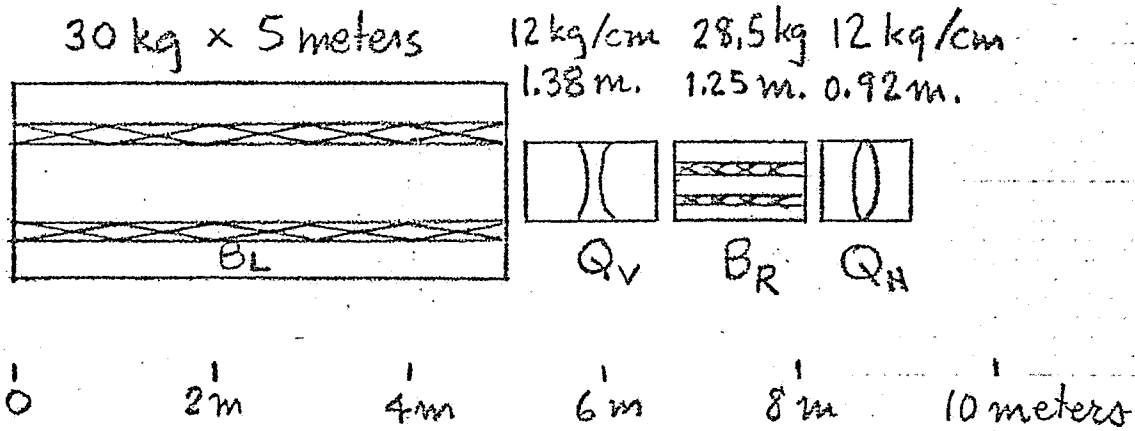cosine-like
sine-like
p-Like

VERT

5 mm   c (0.5 mm) ×10
        s (0.5 mm)

s
c

Fig. 2. Preliminary Hyperon Beam Design